LEVEL II

AEROELASTIC FLUTTER AND DIVERGENCE OF GRAPHITE/EPOXY CANTI-

LEVERED PLATES WITH BENDING-TORSION STIFFNESS COUPLING

by

STEVEN JAMES HOLLOWELL

B.S., United States Air Force Academy
(1977)

SUBMITTED IN PARTIAL FULFILLMENT
OF THE REQUIREMENTS FOR THE
DEGREE OF

MASTER OF SCIENCE

IN

AERONAUTICS AND ASTRONAUTICS

at the

MASSACHUSETTS INSTITUTE OF TECHNOLOGY

Jan   81

© Steven James Hollowell, 1980

Signature of Author _____
Department of Aeronautics and Astronautics
December 11, 1980

Certified by _____
John Dugundji
Thesis Supervisor

Accepted by _____
Harold Y. Wachman
Chairman, Departmental Graduate Committee

AD A101726

DTIC
ELECTE
JUL 22 1981
S D
D

DTIC FILE COPY

REPORT DOCUMENTATION PAGE		READ INSTRUCTIONS BEFORE COMPLETING FORM
1. REPORT NUMBER 80-67T	2. GOVT ACCESSION NO. AD-A101 726	3. RECIPIENT'S CATALOG NUMBER
4. TITLE (and Subtitle) Aeroelastic Flutter and Divergence of Graphite/Epoxy Cantilevered Plates with Bending-Torsion Stiffness Coupling		5. TYPE OF REPORT & PERIOD COVERED THESIS/DISSERTATION
		6. PERFORMING ORG. REPORT NUMBER
7. AUTHOR(s) 1Lt Steven James Hollowell		8. CONTRACT OR GRANT NUMBER(s)
9. PERFORMING ORGANIZATION NAME AND ADDRESS AFIT STUDENT AT: MIT		10. PROGRAM ELEMENT, PROJECT, TASK AREA & WORK UNIT NUMBERS
11. CONTROLLING OFFICE NAME AND ADDRESS AFIT/NR WPAFB OH 45433		12. REPORT DATE Jan 81
		13. NUMBER OF PAGES 136
14. MONITORING AGENCY NAME & ADDRESS(if different from Controlling Office)		15. SECURITY CLASS. (of this report) UNCLASS
		15a. DECLASSIFICATION/DOWNGRADING SCHEDULE

16. DISTRIBUTION STATEMENT (of this Report)

APPROVED FOR PUBLIC RELEASE; DISTRIBUTION UNLIMITED

17. DISTRIBUTION STATEMENT (of the abstract entered in Block 20, if different from Report)

18. SUPPLEMENTARY NOTES

APPROVED FOR PUBLIC RELEASE: IAW AFR 190-17

23 JUN 1981

FREDRIC C. LYNCH, Major, USAF
Director of Public Affairs
Air Force Institute of Technology (ATC)
Wright-Patterson AFB, OH 45433

19. KEY WORDS (Continue on reverse side if necessary and identify by block number)

20. ABSTRACT (Continue on reverse side if necessary and identify by block number)

ATTACHED

81 7 16 087

DD FORM 1473 EDITION OF 1 NOV 65 IS OBSOLETE
1 JAN 73

AEROELASTIC FLUTTER AND DIVERGENCE OF GRAPHITE/EPOXY CANTI-LEVERED PLATES WITH BENDING-TORSION STIFFNESS COUPLING

by

STEVEN JAMES HOLLOWELL

Submitted to the Department of Aeronautics and Astronautics on December 11, 1980, in partial fulfillment of the requirements for the degree of Master of Science in Aeronautics and Astronautics.

ABSTRACT

The aeroelastic flutter and divergence behavior of rectangular, graphite/epoxy, cantilevered plates with varying amounts of bending-torsion stiffness coupling is investigated for incompressible flow. A general Rayleigh-Ritz formulation is used to calculate flexibility influence coefficients, static deflections, divergence velocities, vibration frequencies, and flutter velocities. Flutter calculations are done using the U-g method. Test plates were constructed and subjected to static, vibration and wind tunnel tests. Wind tunnel tests indicated static deflections, divergence instabilities, bending-torsion flutter at low angles of attack, and stall flutter at high angles of attack. Bending stiffness and first bending frequencies showed good agreement between theory and experiment. Torsional stiffness and first torsion frequencies were not accurately predicted by the theory for highly coupled plates. Divergence velocities and reduced flutter velocities showed reasonable agreement between theory and experiment. Test plates with varying amounts of coupling exhibited markedly different stall flutter characteristics.

Thesis Supervisor: John Dugundji

Title: Professor of Aeronautics and Astronautics

ACKNOWLEDGEMENTS

I would like to express my sincere gratitude to Professor J. Dugundji for his guidance, interest, and encouragement in every aspect of this study. I am indebted to Professor J.W. Mar for initially exposing me to the merits of advanced composites, and encouraging me to do research in this area. I would like to thank Mr. M. Shirk at the Air Force Flight Dynamics Laboratory for helping me formulate this thesis topic.

Special thanks must be extended to Al Shaw for his invaluable advice and technical assistance in the experimental portion of this study, to Earle Wassmouth for his help in fabricating the test apparatus, and to Sherry Modestino who had the thankless job of transcribing my semi-legible handwriting into this manuscript.

Finally, I would like to thank the Air Force Institute of Technology for the opportunity to pursue an advanced degree at the Massachusetts Institute of Technology.

TABLE OF CONTENTS

5

LIST OF ILLUSTRATIONS

LIST OF TABLES

CHAPTER I

INTRODUCTION

1.1 Background

Aeroelastic tailoring is broadly defined as the tech-
nology to design a lifting surface which exhibits a desired
aeroelastic response. Desired aeroelastic responses most
often considered are maximization of flutter and divergence
speeds. Other aeroelastic responses can be important de-
pending on the application. They include control reversal
speed, camber changes as a function of load and speed, and
angle of attack changes as a function of load. The aniso-
tropy of advanced composite materials or, more specifically,
the designers' ability to control that anisotropy by selec-
tive lamination, makes it an attractive material for aero-
elastic tailoring.

Aeroelastic tailoring, which exploits the advantage
of advanced composites, has received considerable attention
in recent literature. N.J. Krone, Jr.[1] concluded that
forward swept wings without divergence or weight penalties
may be possible through the use of selectively laminated
advanced composites. T.A. Weisshaar[2,3] extended, analyti-
cally, Krone's conclusion to potentially practical wing
designs. Weisshaar concluded that the binding-torsion
stiffness coupling of anisotropic advanced composite

materials was the key to eliminating divergence in forward swept wings. V.C. Sherrer, T.J. Hertz, and M.H. Shirk[4] conducted a series of wind tunnel tests using simple plate-like models of a forward swept wing. These tests essentially verified Weisshaar's conclusion, and also showed that existing analytical techniques (computer programs) would adequately predict the divergence dynamic pressures for most test conditions.

Under contract to the Air Force Flight Dynamics Laboratory, General Dynamics Corporation developed a wing aeroelastic synthesis computer program (TSO)[5]. The computer program was intended to be a preliminary design tool for optimization of wings with advanced composite structural box skins. To this end, it used a direct Rayleigh-Ritz energy formulation to model the structural deflections. The program was capable of optimizing a wing skin design for several different constraints, simultaneously. Published aeroelastic tailoring studies[5,6,7] using TSO have not examined, in depth, the effect of structural bending-torsion coupling on flutter speed in the absence of changes in other variables. Additionally, only very limited wind tunnel data are available which examine the effect of structural bending torsion coupling on flutter speed, or even that verify the accuracy of flutter speeds generated by TSO. Finally, the phenomenon known as stall flutter has received only limited attention

as it relates to metal lifting surfaces[8,9], and virtually none as related to advanced composite lifting surfaces.

The references cited in this section by no means comprise a complete list of work done in this area. They should be viewed more as an indicator of where emphasis has been placed. One obstacle to conducting research in aeroelastic tailoring is that much of the work done by the larger aerospace corporations is proprietary and consequently is never reported in literature accessible to the public.

1.2 Objectives

This study will attempt to ascertain the effect of varying amounts of bending-torsion coupling on both the divergence and flutter speeds of an unswept lifting surface in incompressible flow. The lifting surface will be idealized by a cantilevered, rectangular, flat plate constructed of laminated graphite/epoxy, and having a half-span aspect ratio of 4 (8 by standard aerodynamic convention).

Specific objectives are to

(1) Develop an analytical formulation to predict static deflections, natural vibration frequencies, divergence speed, and flutter speed for idealized lifting surfaces. The formulation must be applicable to a plate having substantial bending-torsion coupling, but limited to a mid-plane symmetric lamination arrangement.

(2) Evaluate the effect of bending-torsion coupling on the idealized lifting surface by performing static deflection, vibration, and wind tunnel tests on selected cantilevered plates having varying amounts of bending-torsion coupling.

(3) Investigate the effects of bending-torsion coupling on stall flutter velocity. This will be limited to an experiment evaluation.

(4) Determine the accuracy of the analytical formulation by comparing theoretical and experimental results.

1.3 Organization

Chapter II develops a general Rayleigh-Ritz energy formulation to model lateral deflections of a laminated cantilever plate. Solutions for both two term and three term deflection equations are derived. The two term general solution is than applied to a static deflection problem to calculate a 2 x 2 matrix of flexibility influence coefficients, and to a divergence problem to calculate the divergence velocity of the idealized lifting surface. Both two and three term solutions are applied to a free vibration problem to determine the lower two or three vibration frequencies. Finally, the two term solution is applied to a

classical bending-torsion, potential flow, flutter problem using the U-g method.

Chapter III presents the experimental test apparatus and procedures for the static deflection tests, free vibration tests, and wind tunnel tests (flutter and divergence). The test results are then discussed, commenting on possible sources of error.

Chapter IV compares the analytical and theoretical results, identifies areas of good and poor agreement, and comments on sources of inaccuracies in the theoretical analysis, as well as ways to improve it.

Chapter V summarizes the conclusions reached in the previous chapters and makes recommendations for further study.

CHAPTER II

THEORY

2.1 Anisotropic Plate Flexural Stiffness

The flexural modulus (stiffness) components of a laminated advanced composite (graphite/epoxy in this study) plate are dependent on both the fiber orientation and stacking sequence of the individual laminae (plies). To simplify fabrication of test specimens, only laminated plates with a mid-plane symmetric stacking sequence are considered . The ply angles (θ) follow the sign convention in Fig. 1.
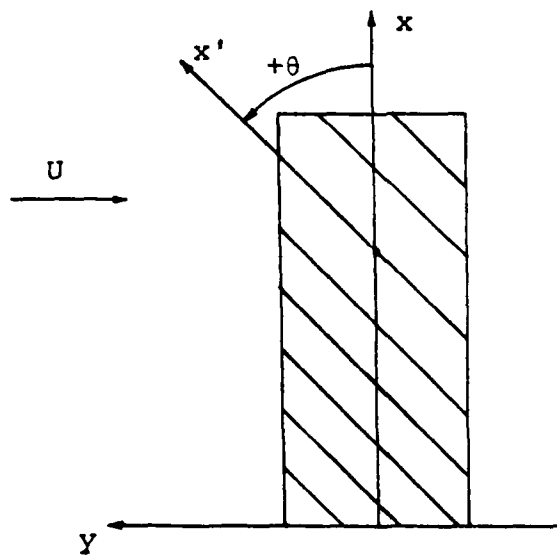
Figure 1. Ply Angle Sign Convention

The in-plane, on-axis lamina modulus components (Q_{ij}) were obtained from the orthotropic engineering constants for Hercules AS/3501-6 graphite/epoxy, from which the test specimens were to be fabricated. These engineering constants take on different values depending on whether they are obtained from bending or stretching tests. Engineering constants obtained from each type of test appear in Appendix A, and their validity for vibration problems is briefly discussed in Chapter IV (Reference 10 has an in-depth treatment of this subject.) The Q_{ij} terms are defined as[11]

$$Q_{11} = E_L/(1 - \nu_{LT}\nu_{TL}) \qquad (2\text{-}1a)$$

$$Q_{22} = E_T/(1 - \nu_{LT}\nu_{TL}) \qquad (2\text{-}1b)$$

$$Q_{12} = Q_{21} = \nu_{LT}E_T/(1 - \nu_{LT}\nu_{TL}) \qquad (2\text{-}1c)$$

$$Q_{66} = G_{LT} \qquad (2\text{-}1d)$$

where $\nu_{TL} = (E_T/E_L)\nu_{LT}$

The off-axis lamina modulus components $(Q_{ij}^{(\theta)})$ were obtained by first defining a set of invariants[11]

$$I_1 = [Q_{11} + Q_{22} + 2Q_{12}]/4 \qquad (2\text{-}2a)$$

$$I_2 = [Q_{11} + Q_{22} - 2Q_{12} + 4Q_{66}]/8 \qquad (2\text{-}2b)$$

$$R_1 = [Q_{11} - Q_{22}]/2 \qquad (2\text{-}2c)$$

$$R_2 = [Q_{11} + Q_{22} - 2Q_{12} - 4Q_{66}]/8 \qquad (2\text{-}2d)$$

and using the invariants in the following transformation relations[11]:

$$Q_{11}^{(\theta)} = I_1 + I_2 + R_1\cos2\theta + R_2\cos4\theta \qquad (2\text{-}3a)$$

$$Q_{22}^{(\theta)} = I_1 + I_2 - R_1\cos2\theta + R_2\cos4\theta \qquad (2\text{-}3b)$$

$$Q_{12}^{(\theta)} = I_1 - I_2 - R_2\cos4\theta \qquad (2\text{-}3c)$$

$$Q_{66}^{(\theta)} = I_2 - R_2\cos4\theta \qquad (2\text{-}3d)$$

$$Q_{16}^{(\theta)} = \frac{1}{2} R_1\sin2\theta + R_2\sin4\theta \qquad (2\text{-}3e)$$

$$Q_{26}^{(\theta)} = \frac{1}{2} R_1\sin2\theta - R_2\sin4\theta \qquad (2\text{-}3f)$$

where θ is the ply angle (Fig. 1).

The flexural modulus (D_{ij}) for an n-ply laminate with arbitrary ply angle orientation is obtained from

$$D_{ij} = \sum_{k=1}^{n} Q_{ij}^{(\theta_k)} [(z_k^3 - z_{k-1}^3)/3] \quad i,j = 1,2,6 \quad (2\text{-}4)$$

where

θ_k = ply angle of the $(k)^{th}$ ply

z_k = distance from the mid-plane to the upper surface of the $(k)^{th}$ ply (positive above mid-plane, negative below mid-plane)

z_{k-1} = distance from the midplane to the lower surface of the $(k)^{th}$ ply

Flexural modulus values (D_{11}, D_{66}, D_{16}) for $[0_2/90]_s$,

$[+30_2/0]_s$, $[+45_2/0]_s$, and $[\pm45/0]_s$ laminates appear in Appendix A. The reader should observe that, using the equations in this section, the flexural moduli of a $[+\theta_2/0]_s$ laminate will be the same as those for a $[-\theta_2/0]_s$ laminate, with the exception of a negative sign on D_{16} and D_{26} for the latter laminate.

2.2 General Rayleigh-Ritz Formulation

The direct Rayleigh-Ritz energy method is a relatively simple, straightforward approximation for the plate deflections, as required for the static deflection, free vibration, divergence, and flutter analyses in this study. The Rayleigh-Ritz method also has the advantage of showing the effect of the individual variables on the solution more clearly than other more accurate methods, such as finite element analysis. Whether or not the results of the Rayleigh-Ritz analysis developed in this chapter correlate sufficiently well with experimental results is discussed in Chapter IV. To simplify computation, the "wing" is idealized by a rectangular cantilevered flat plate with uniform thickness. Further, to allow the stiffness properties of the plate to be more accurately depicted, an aerodynamic fairing will not be used over the plate.

The Rayleigh-Ritz analysis begins by assuming a deflection shape for the structure. If only lateral deflections

(w) are allowed, the single deflection equation, written in generalized coordiates is:

$$w = \sum_{i=1}^{n} \gamma_i(x,y)q_i(t) \qquad (2\text{-}5)$$

where $\gamma_i(x,y)$ is the nondimensional deflection or mode shape of the (i)th mode (which must satisfy geometric boundary conditions for a cantilevered plate), and $q_i(t)$ is the generalized displacement of the (i)th mode. The generalized displacement is a function only of time and has units of length. For convenience and consistency, the coordinate system in Fig. 2 will be used for all problems.

The deflection equation is simplified by assuming

(1) the plate is chordwise rigid when undergoing torsional deflections,

(2) the plate does not exhibit chordwise bending for any of the problems to be developed,

(3) a single term in the deflection equation for each of the desired deflection modes (first bending and first torsion; or first bending, second bending, and first torsion) will adequately represent the actual deflections of the plate. A further requirement here, to insure rapid convergence, is that the mode shape for each term must accurately depict the deflection for that mode. The two term deflection equation can now be written as
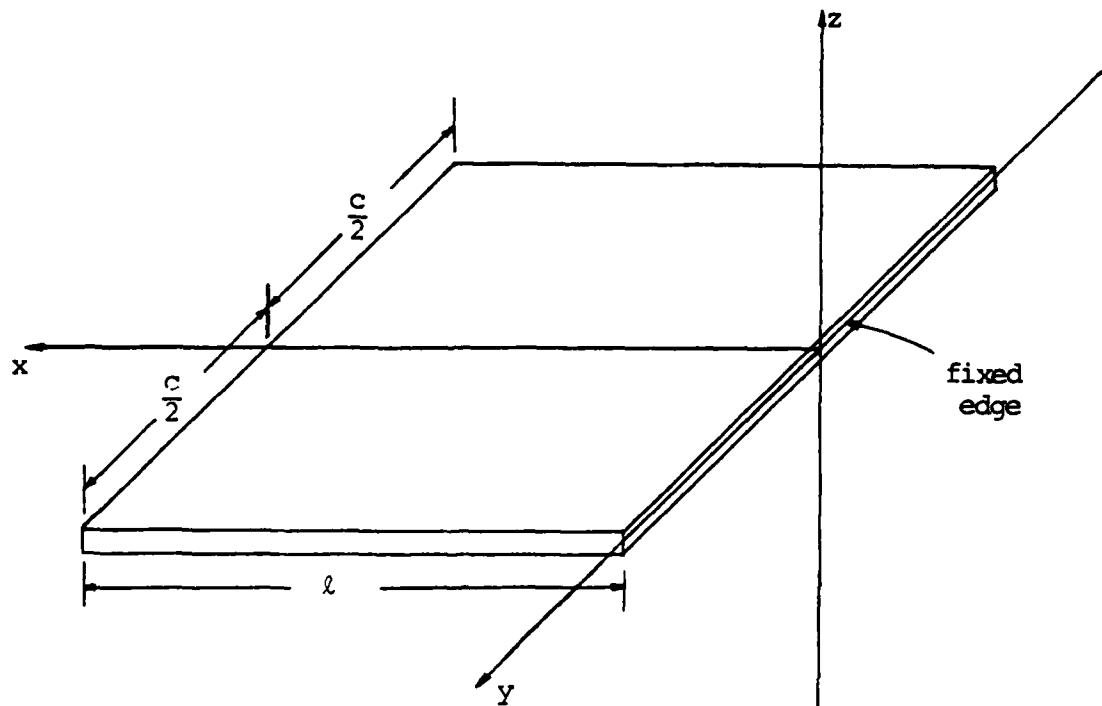
(a) Geometric Sign Convention
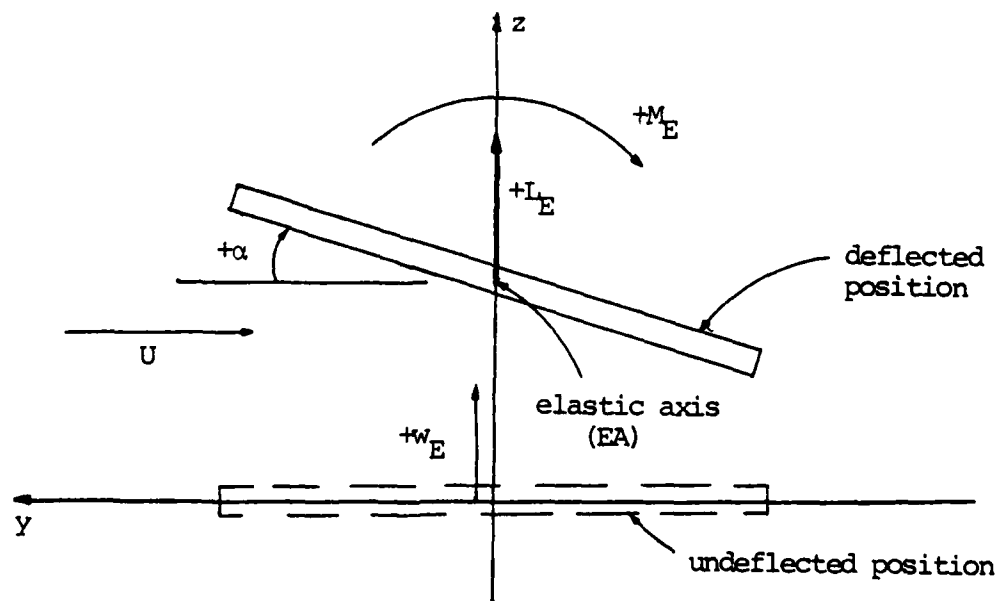
(b) Force-Moment-Deflection Sign Convention

Figure 2. Sign Conventions

$$w = \phi_1(x)\phi_1(y)q_1(t) + \phi_\alpha(x)\phi_\alpha(y)q_2(t) \qquad (2\text{-}6)$$

where $\phi_i(x)$ and $\phi_i(y)$ are one dimensional mode shapes for the $(i)^{th}$ mode. If the first term represents the first bending mode, then $\phi_1(y)$ is simply a rigid-body translation $(\phi_1(y) = 1)$. If the second term represents the first torsion mode, then, by the first assumption, $\phi_\alpha(y)$ is a rigid body rotation $(\phi_\alpha(y) = y/c)$. Incorporating these into Eq. 2-6 yields

$$w = \phi_1(x)q_1(t) + (y/c)\phi_\alpha(x)q_2(t) \qquad (2\text{-}7)$$

We can apply the same analogy to the three term deflection equation, which is written as

$$w = \phi_1(x)q_1(t) + \phi_2(x)q_2(t) + (y/c)\phi_\alpha(x)q_3(t) \quad (2\text{-}8)$$

. In Fig. 2b, the elastic axis (EA) is, by definition, located at the midchord of the plate $(y = 0)$. Lateral deflection of the elastic axis is designated w_E and rotation of the plate about its elastic axis is designated α. One observes that w_E and α are not generalized coordinates and, in fact, q_2 in Eq. 2-7 and α do not even have the same units. The units of α are radians, while q_2 has units of length. To write w_E and α in generalized coordinates (for Eq. 2-7), the following relations are used:

$$w_E = w_{y=0} = \phi_1(x)q_1(t) \tag{2-9}$$

$$\alpha = \frac{\partial w}{\partial y} = (\phi_\alpha(x)/c)q_2(t) \tag{2-10}$$

The importance of this transformation will become apparent when aerodynamic forces are applied. Finally, from Fig. 2b, F_E is a lateral force applied at the elastic axis and M_E is a moment about the elastic axis.

The strain energy (V) for a symmetric anisotropic laminate is[12]

$$V = \frac{1}{2} \int_0^\ell \int_{-\frac{c}{2}}^{\frac{c}{2}} [D_{11}(w,_{xx})^2 + 2D_{12}w,_{xx}w,_{yy}$$

$$+ D_{22}(w,_{yy})^2 + 4D_{16}w,_{xx}w,_{yy} + 4D_{26}w,_{yy}w,_{xy}$$

$$+ 4D_{66}(w,_{xy})^2] \, dydx \tag{2-11}$$

where a comma denotes partial differentiation.

2.2.1 Two Term Deflection Equation

$$w,_{xx} = \phi_1''q_1 + \frac{y}{c}\phi_\alpha''q_2 \qquad w,_{xy} = (1/c)\phi_\alpha'q_2$$

$$w,_{yy} = 0 \tag{2-12}$$

where: $(\ )' = d/dx$ and $(\ )'' = d^2/dx^2$. Substituting Eq. 2-12 into Eq. 2-11 and performing the chordwise integration yields

$$V = q_1^2 \left[\frac{D_{11}c}{2} \int_0^\ell (\phi_1'')^2 dx \right] + q_1 q_2 \left[2D_{16} \int_0^\ell \phi_1'' \phi_\alpha' dx \right]$$

$$+ q_2^2 \left[\frac{cD_{11}}{24} \int_0^\ell (\phi_\alpha'')^2 dx + \frac{2D_{66}}{c} \int_0^\ell (\phi_\alpha')^2 dx \right] \quad (2\text{-}13)$$

The kinetic energy expression for the plate is

$$T = \frac{1}{2} \int_0^\ell \int_{-\frac{c}{2}}^{\frac{c}{2}} m \dot{w}^2 \, dy dx \quad (2\text{-}14)$$

where $(\dot{\ }) = d/dt$ and m is the mass/area.

$$m = \rho_{GE} t_p \quad (2\text{-}15)$$

where ρ_{GE} is the specific gravity of graphite/epoxy and t_p is the plate thickness.

$$\dot{w} = \phi_1 \dot{q}_1 + (y/c) \phi_\alpha \dot{q}_2 \quad (2\text{-}16)$$

Performing the chordwise integration, Eq. 2-14 then becomes

$$T = \dot{q}_1^2 \left[\frac{mc}{2} \int_0^\ell \phi_1^2 dx \right] + \dot{q}_2^2 \left[\frac{mc}{24} \int_0^\ell \phi_\alpha^2 dx \right] \quad (2\text{-}17)$$

The change in external work (δW_e) can be expressed as

$$\delta W_e = \int_0^\ell \int_{-\frac{c}{2}}^{\frac{c}{2}} p_z \delta w \, dy dx \quad (2\text{-}18)$$

where p_z is a distributed lateral load and

$$\delta w = \phi_1 \delta q_1 + \frac{y}{c} \phi_\alpha \delta q_2 \quad (2\text{-}19)$$

Then, by substitution

$$\delta W_e = \delta q_1 Q_1 + \delta q_2 Q_2 \qquad (2\text{-}20)$$

where

$$Q_1 = \int_0^{\ell} \int_{-\frac{c}{2}}^{\frac{c}{2}} p_z \phi_1 dy dx$$

and

$$Q_2 = \int_0^{\ell} \int_{-\frac{c}{2}}^{\frac{c}{2}} p_z \frac{y}{c} \phi_\alpha dy dx$$

The relationship between the work and energy expressions is obtained through Lagrange's equation, which is a statement of Hamilton's energy principle; the basic premise of the Rayleigh-Ritz method. Lagrange's equation is[13]

$$\frac{d}{dt} \left(\frac{\partial T}{\partial \dot{q}_i} \right) + \frac{\partial V}{\partial q_i} - \frac{\partial T}{\partial q_i} = Q_i \qquad (2\text{-}21)$$

$$(i = 1, 2, \ldots N)$$

where:

$$\frac{\partial V}{\partial \dot{q}_i} = 0$$

$$\frac{\partial V}{\partial q_1} = 2q_1 \left[\frac{D_{11}c}{2} \int_0^{\ell} (\phi_1'')^2 dx \right] + q_2 \left[2D_{16} \int_0^{\ell} \phi_1' \phi_\alpha' dx \right]$$

$$\frac{\partial V}{\partial q_2} = q_1 \left[2D_{16} \int_0^{\ell} \phi_1'' \phi_\alpha' dx \right] + 2q_2 \left[\frac{cD_{11}}{24} \int_0^{\ell} (\phi_\alpha'')^2 dx + \frac{2D_{66}}{c} \int_0^{\ell} (\phi_\alpha')^2 dx \right]$$

$$\frac{\partial T}{\partial \dot{q}_1} = 2\dot{q}_1 \left[\frac{mc}{2} \int_0^{\ell} \phi_1^2 \ dx\right]$$

$$\frac{d}{dt}\left(\frac{\partial T}{\partial \dot{q}_1}\right) = \ddot{q}_1 \left[mc \int_0^{\ell} \phi_1^2 \ dx\right]$$

$$\frac{\partial T}{\partial \dot{q}_2} = 2\dot{q}_2 \left[\frac{mc}{24} \int_0^{\ell} \phi_\alpha^2 \ dx \right]$$

$$\frac{d}{dt}\left(\frac{\partial T}{\partial \dot{q}_2}\right) = \ddot{q}_2 \left[\frac{mc}{12} \int_0^{\ell} \phi_\alpha^2 \ dx\right]$$

From Eq. 2-21, the general equations of motion for the plate with a two term assumed displacement equation are

$$\ddot{q}_1\left[mc \int_0^{\ell} \phi_1^2 \ dx\right] + q_1 \left[D_{11}c \int_0^{\ell} (\phi_1'')^2 dx\right]$$

$$+ q_2\left[2D_{16} \int_0^{\ell} \phi_1'' \phi_\alpha' \ dx\right] = Q_1 \qquad (2\text{-}22a)$$

$$\ddot{q}_2\left[\frac{mc}{12} \int_0^{\ell} \phi_\alpha^2 \ dx\right] + q_1 \left[2D_{16} \int_0^{\ell} \phi_1'' \phi_\alpha' \ dx\right]$$

$$+ q_2 \left[\frac{cD_{11}}{12} \int_0^{\ell} (\phi_\alpha'')^2 dx \right.$$

$$\left. + \frac{4D_{66}}{c} \int_0^{\ell} (\phi_\alpha')^2 \ dx\right] = Q_2 \qquad (2\text{-}22b)$$

To make these equations more compact, nondimensional expressions for the integrals are defined below. These integral expressions may be evaluated exactly, or using any of several

numerical integration techniques, if the integrand is too complicated.

$$I_3 \equiv \frac{1}{\ell} \int_0^\ell \phi_1 \phi_\alpha \, dx \qquad\qquad (2\text{-}23a)$$

$$I_4 \equiv \frac{1}{\ell} \int_0^\ell \phi_1^2 \, dx \qquad\qquad (2\text{-}23b)$$

$$I_5 \equiv \frac{1}{\ell} \int_0^\ell \phi_\alpha^2 \, dx \qquad\qquad (2\text{-}23c)$$

$$I_6 \equiv \ell^2 \int_0^\ell \phi_1'' \phi_\alpha' \, dx \qquad\qquad (2\text{-}23d)$$

$$I_7 \equiv \ell^3 \int_0^\ell (\phi_1'')^2 \, dx \qquad\qquad (2\text{-}23e)$$

$$I_8 \equiv \ell \int_0^\ell (\phi_\alpha')^2 \, dx \qquad\qquad (2\text{-}23f)$$

$$I_{11} \equiv \ell^3 \int_0^\ell (\phi_\alpha'')^2 \, dx \qquad\qquad (2\text{-}24g)$$

Incorporating the expressions of Eq. 2-23 into Eqs. 2-22a and b yields the final form of the equations of motion.

$$\ddot{q}_1 \, [mc\ell I_4] + q_1 \, [\frac{D_{11}c}{\ell^3} I_7] + q_2 [\frac{2D_{16}}{\ell^2} I_6] \; = Q_1 \qquad (2.24a)$$

$$\ddot{q}_2 \, [\frac{mc\ell}{12} I_5] + q_1 \, [\frac{2D_{16}}{\ell^2} I_6]$$
$$+ q_2 \, [\frac{4D_{66}}{c\ell} (I_8 + \frac{D_{11}c^2}{48D_{66}\ell^2} I_{11})] \; = Q_2$$
$$(2.24b)$$

EQUATIONS OF MOTION

In Eq. 2-24b, the term

$$\frac{c^2 D_{11}}{48 \ell^2 D_{66}} I_{11}$$

represents the warping stiffness, which is inversely proportional to the square of the plate aspect ratio (ℓ/c). For the plates in this study (AR = 4), this term's contribution will be small.

2.2.2 Three Term Deflection Equation

The derivation of the equations of motion for the three term deflection equation is almost identical to the two-term deflection equation derivation. Therefore, only the final expressions for V, T, δW_e, and Lagrange's equation will be presented. As one would expect, there will be three equations of motion instead of two.

Deflection equation:

$$w = \phi_1(x) q_1(t) + \phi_2(x) q_2(t) + \frac{y}{c} \phi_\alpha(x) q_3(t) \qquad (2\text{-}25)$$

Strain energy:

$$V = [\frac{D_{11}c}{2} \int_0^\ell (\phi_1'')^2 \, dx] q_1 + [\frac{D_{11}c}{2} \int_0^\ell (\phi_2'')^2 dx] q_2^2$$

$$+ [\frac{D_{11}c}{24} \int_0^\ell (\phi_\alpha'')^2 dx + \frac{2D_{66}}{c} \int_0^\ell (\phi_\alpha')^2 dx] q_3^2$$

$$+ [D_{11}c \int_0^\ell \phi_1'' \phi_2'' dx] q_1 q_2 + [2D_{16} \int_0^\ell \phi_1'' \phi_\alpha' dx] q_1 q_3$$

$$+ [2D_{16} \int_0^\ell \phi_2'' \phi_\alpha' dx] q_2 q_3 \qquad (2\text{-}26)$$

Kinetic energy:

$$T = \dot{q}_1^2 \left[\frac{mc}{2} \int_0^{\ell} \phi_1^2 dx \right] + \dot{q}_2^2 \left[\frac{mc}{2} \int_0^{\ell} \phi_2^2 dx \right]$$

$$+ \dot{q}_3^2 \left[\frac{mc}{24} \int_0^{\ell} \phi_\alpha^2 dx \right] + \dot{q}_1 \dot{q}_2 \left[mc \int_0^{\ell} \phi_1 \phi_2 dx \right]$$

$$(2-27)$$

Change in external work:

$$\delta W_e = Q_1 \delta q_1 + Q_2 \delta q_2 + Q_3 \delta q_3 \qquad (2-28)$$

where:

$$Q_1 = \int_0^{\ell} \int_{-\frac{c}{2}}^{\frac{c}{2}} p_z \phi_1 \, dy dx$$

$$Q_2 = \int_0^{\ell} \int_{-\frac{c}{2}}^{\frac{c}{2}} p_z \phi_2 \, dy dx$$

$$Q_3 = \int_0^{\ell} \int_{-\frac{c}{2}}^{\frac{c}{2}} p_z \frac{Y}{c} \phi_\alpha \, dy dx$$

Before applying Lagrange's equation, we eliminate terms

with $\int_0^{\ell} \phi_1 \phi_2 dx$ and $\int_0^{\ell} \phi_1'' \phi_2'' \, dx$

by requiring that $\phi_1(x)$ and $\phi_2(x)$ be orthogonal functions.
Now, using the same nondimensional expressions for the inte-
grals as before, the equations of motion obtained from
Lagrange's equations are:

$$\ddot{q}_1 \left[mc\ell\ I_4 \right] + q_1 \left[\frac{D_{11}c}{\ell^3}\ I_7 \right] + q_3 \left[\frac{2D_{16}}{\ell^2}\ I_6 \right]$$

$$= Q_1 \qquad \text{(2-29a)}$$

$$\ddot{q}_2 \left[mc\ell\ I_{12} \right] + q_2 \left[\frac{D_{11}c}{\ell^3}\ I_{10} \right] + q_3 \left[\frac{2D_{16}}{\ell^2}\ I_9 \right]$$

$$= Q_2 \qquad \text{(2-29b)}$$

$$\ddot{q}_3 \left[\frac{mc\ell}{12}\ I_5 \right] + q_1 \left[\frac{2D_{16}}{\ell^2}\ I_6 \right] + q_2 \left[\frac{2D_{16}}{\ell^2}\ I_9 \right]$$

$$+ q_3 \left[\frac{4D_{66}}{c\ell} \left(I_8 + \frac{D_{11}c^2}{48D_{66}\ell^2}\ I_{11} \right) \right] = Q_3$$

$$\text{(2-29c)}$$

$$\boxed{\text{EQUATIONS OF MOTION}}$$

where

$$I_9 \equiv \ell^2 \int_0^\ell \phi_2'' \phi_\alpha'\ dx$$

$$I_{10} \equiv \ell^3 \int_0^\ell (\phi_2'')^2\ dx$$

$$I_{12} \equiv \frac{1}{\ell} \int_0^\ell \phi_2^2\ dx$$

The functions used in this study for the mode shapes $(\phi_1,\ \phi_2,\ \phi_\alpha)$ are combinations of sin, cos, sinh, and cosh. These functions are known as "beam" modes because they very closely model the deflections of an isotropic Euler beam. The first bending mode shape (ϕ_1) and the first

torsion mode shape (ϕ_α) were obtained from Ref. 14 and the second bending mode was obtained from Ref. 15. These mode shapes, along with numerical values for the nondimensional integral expressions, appear in Appendix B.

2.3 Static Deflection Problem

The static deflection problem is formulated as an analytical model of the experimental deflection tests described in Chapter III. For this problem, the cantilevered plate is subjected to a concentrated unit load and moment, individually applied at the 3/4 length point on the elastic axis. Since the result of the experimental tests was a 2 x 2 flexibility influence coefficient matrix, the same result is desired here, to allow direct comparison. The 2 x 2 matrix requirement dictates that we use the equations of motion derived from the two term deflection equation. Observing that acceleration ($\ddot{q}$) for static deflections is zero, Eqs. 2-25a and b are repeated here with $\ddot{q}$ terms eliminated.

$$q_1 \left[\frac{D_{11}c}{\ell^3} I_7 \right] + q_2 \left[\frac{2D_{16}}{\ell^2} I_6 \right] = Q_1 \qquad (2\text{-}30a)$$

$$q_1 \left[\frac{2D_{16}}{\ell^2} I_6 \right] + q_2 \left[\frac{cD_{11}}{12\ell^3} I_{11} + \frac{4D_{66}}{c\ell} I_8 \right] = Q_2$$
$$(2\text{-}30b)$$

The generalized forces (Q_i) obtained from Eq. 2-20 are

$$Q_1 = F_T \phi_1 (\tfrac{3}{4} \ell)$$ (2-31a)

$$Q_2 = M_T \phi_\alpha (\tfrac{3}{4} \ell) / c$$ (2-31b)

where F_t is a concentrated test load and M_t is a concentrated test moment such that

$$F_T = \int_0^\ell \int_{-\frac{c}{2}}^{\frac{c}{2}} p_z \, dy dx \quad \text{and} \quad M_T = \int_0^\ell \int_{-\frac{c}{2}}^{\frac{c}{2}} y \, p_z \, dy dx$$

The test forces and moments are applied at the same locations and with the same sign conventions as F_E and M_E in Fig. 2b. By the relations of Eqs. 2-9 and 2-10, the deflections w_E and α taken at $x = \tfrac{3}{4} \ell$ are

$$w_E = \phi_1 (\tfrac{3}{4} \ell) q_1$$ (2-32)

$$\alpha = [\phi_\alpha (\tfrac{3}{4} \ell) / c] q_2$$ (2-33)

Assuming unit forces and moments, instead of unit displacements, dictates that one will obtain flexibility inflence coefficients (c_{ij}) by solving the equations of motion. The matrix of influence coefficients must then be inverted to obtain the stiffness influence coefficients (k_{ij}). This is generally much easier to accomplish experimentally than to try and obtain the stiffness influence coefficients directly, by applying unit displacements to

the structure. To aid in conceptualizing the problem, the
equations of motion in terms of flexibility influences are
presented.

$$w_E = c_{11}F_T + c_{12}M_T \qquad \text{(2-34a)}$$

$$\alpha = c_{21}F_T + c_{22}M_T \qquad \text{(2-34b)}$$

The flexibility influence coefficients are defined as follows.

$$c_{11} \equiv w_E/F_T \Big|_{M_T = 0}$$

$$c_{12} \equiv w_E/M_T \Big|_{F_T = 0}$$

$$c_{21} \equiv \alpha/F_T \Big|_{M_T = 0} \qquad \text{(2-35)}$$

$$c_{22} \equiv \alpha/M_T \Big|_{F_T = 0}$$

To obtain the four flexibility influence coefficients,
Eqs. 2-30a and b must be solved simultaneously twice, each
time with a different combination of Q_1 and Q_2. The first
combination ($F_T = 1$ and $M_T = 0$) will be called "Test 1",
and the second combination ($F_T = 0$ and $M_T = 1$) will be called
"Test 2". The values for q_1 and q_2 obtained from Test 1,
when substituted into Eqs. 2-32 and 2-33, yield c_{11} and c_{21}
as defined by Eq. 2-35. Similarly, q_1 and q_2 from Test 2

yield c_{12} and c_{22}. The final step, if desired, is to arrange the flexibility influence coefficients in a 2 x 2 matrix and invert it to obtain the stiffness influence co-efficients.

2.4   Aeroelastic Divergence Problem

Aeroelastic divergence is a static deflection problem such that the aerodynamic forces and moments applied to the cantilevered plate are a function of the torsional deflection of the plate. Divergence is defined as the point at which the restoring forces generated by the structure can no longer counteract the aerodynamic forces. At that point, by the simple linear theory used in this study, the deflections increase without bound resulting in structural failure. Actually, as discussed in Chapter III, both structural and aerodyanmic nonlinearities come into play at large deflections and limit the maximum deflections to finite values. However, structural failure may still occur. These non-linearities, while important, will not be considered in this development.

The static forms ($\ddot{q} = 0$) of Eqs. 2-25a and b are repeated here.

$$q_1 \left[\frac{D_{11}c}{\ell^3} I_7 \right] + q_2 \left[\frac{2D_{16}}{\ell^2} I_6 \right] = Q_1 \qquad (2\text{-}36a)$$

$$q_1 \left[\frac{2D_{16}}{\ell^2} I_6 \right] + q_2 \left[\frac{4D_{66}}{c\ell} \left(I_8 + \frac{D_{11}c^2}{48D_{66}\ell^2} I_{11} \right) \right]$$

$$= Q_2 \qquad (2\text{-}36b)$$

The generalized forces (Q_i) obtained from Eq. 2-20 are

$$Q_1 = \int_0^\ell \phi_1 L_E \, dx \qquad (2\text{-}37a)$$

$$Q_2 = \int_0^\ell \frac{\phi_\alpha}{c} M_E \, dx \qquad (2\text{-}37b)$$

where

$$L_E = \int_{-\frac{c}{2}}^{\frac{c}{2}} p_z \, dy$$

$$M_E = \int_{-\frac{c}{2}}^{\frac{c}{2}} y \, p_z \, dy$$

L_E is the lift per unit length acting at the elastic axis of the plate, in the same direction as F_E (Fig. 2b). M_E is the aerodynamic moment per unit length, again acting at the elastic axis.

For this simple static analysis, two-dimensional aerodynamic strip theory was deemed to provide sufficient accuracy. The lift per unit length and moment per unit length are

$$L_E = qca_0(\alpha_0 + \alpha_e) \qquad (2\text{-}38a)$$

$$M_E = qcea_0(\alpha_0 + \alpha_e) \qquad (2\text{-}38b)$$

where q is the dynamic pressure, e is the distance between the elastic axis and the aerodynamic center (quarterchord) of the wing, a_0 is the two dimensional lift curve slope, α_0 is the rigid plate angle of attack and α_e is the flexible twist of the plate, such that $\alpha_0 + \alpha_e = \alpha$ (Fig. 2b).

The lift curve slope of a flat plate of infinite length (span) is the well known value 2π. This two dimensional lift curve slope can be empirically corrected to account for the affects of finite span by applying the correction suggested in Ref. 13.

$$\frac{\partial C_\ell}{\partial \alpha} \simeq a_0 \left[\frac{AR}{AR + 2} \right] \tag{2-39}$$

where $\partial C_\ell / \partial \alpha$ is the corrected lift curve slope and AR is the aspect ratio $(2\ell/c)$ of an equivalent wing, as defined for an aircraft wing composed of two cantilevered plates.

Equations 2-38a and b must be transformed to generalized coordinates before they are incorporated in the equations of motion. As before, Eq. 2-10 is used to transform α_e only. The generalized forces finally take the form:

$$Q_1 = qc\ell \frac{\partial C_\ell}{\partial \alpha} \left[\alpha_0 I_1 + \frac{q_2}{c} I_3 \right] \tag{2-40a}$$

$$Q_2 = qe\ell \frac{\partial C_\ell}{\partial \alpha} \left[\alpha_0 I_2 + \frac{q_2}{c} I_5 \right] \tag{2-40b}$$

where the nondimensional integral expressions are

$$I_1 \equiv \frac{1}{\ell} \int_0^\ell \phi_1 \, dx$$

$$I_2 \equiv \frac{1}{\ell} \int_0^\ell \phi_\alpha \, dx$$

$$I_3 \equiv \frac{1}{\ell} \int_0^\ell \phi_1 \phi_\alpha \, dx$$

$$I_5 \equiv \frac{1}{\ell} \int_0^\ell \phi_\alpha^2 \, dx$$

Substituting Eqs. 2-40a and b into Eqs. 2-36a and b yields the complete equations of motion. These equations are presented here in matrix form to make the solution technique more apparent.

$$\begin{bmatrix} \dfrac{D_{11}c}{\ell^3} I_7 & \dfrac{2D_{16}}{\ell^2} I_6 - q\ell \dfrac{\partial C_\ell}{\partial \alpha} I_3 \\[2em] \dfrac{2D_{16}}{\ell^2} I_6 & \left[\dfrac{4D_{66}}{c\ell} \left(I_8 + \dfrac{D_{11}c^2}{48D_{66}\ell^2} I_{11} \right) \right] - q \dfrac{e}{c}\ell \dfrac{\partial C_\ell}{\partial \alpha} I_5 \end{bmatrix} \begin{Bmatrix} q_1 \\[2em] q_2 \end{Bmatrix}$$

$$= \begin{Bmatrix} qc\ell \dfrac{\partial C_\ell}{\partial \alpha} I_1 \\[2em] qe\ell \dfrac{\partial C_\ell}{\partial \alpha} I_2 \end{Bmatrix} \alpha_0 \qquad\qquad (2\text{-}41)$$

Classical divergence is normally evaluated at zero initial angle of attack ($\alpha_0 = 0$), which is also assumed

here. Therefore, a unique solution to Eq. 2-41, with
$\alpha_0 = 0$, can be found by setting the determinant of the coefficient matrix equal to zero and solving for the dynamic pressure (q). The dynamic pressure which makes the determinant go to zero is the divergence dynamic pressure (q_D), which is related to the divergence velocity (U_D) by

$$q = \frac{1}{2} \rho_\infty U^2 \qquad (2-42)$$

After evaluating the determinant, we obtain the following expression for q_D.

$$q_D = \left(\frac{4D_{66}}{\ell^3} \right) \frac{\left[\frac{D_{11}c^2}{48D_{66}\ell^2} I_7 I_{11} + I_7 I_8 - \frac{D_{16}^2}{D_{11}D_{66}} I_6^2 \right]}{\left[\frac{e}{\ell} I_5 I_7 - \frac{2D_{16}}{D_{11}} I_3 I_6 \right] \frac{\partial C_\ell}{\partial \alpha}} \qquad (2-43)$$

When the integrals are evaluated using the beam mode shapes in Appendix B, the contribution of

$$\frac{D_{11}c^2}{48D_{66}\ell^2} I_7 I_{11}$$

will be small. The contribution of

$$\frac{D_{16}^2}{D_{11}D_{66}} I_6^2$$

to the value of q_D, while not negligibly small, is much less

than that of

$$\frac{2D_{16}}{D_{11}} \ I_3 I_6$$

The denominator of Eq. 2-44 will be zero when

$$\frac{D_{16}}{D_{11}} = \frac{eI_5 I_7}{2\ell I_3 I_6} \simeq 0.3 \ \frac{c}{\ell} \quad \text{(for examples in} \atop \text{this study)} \quad (2\text{-}44)$$

When D_{16}/D_{11} equals this critical value, q_D becomes infinite and the wing will not diverge. Above the critical value, q_D is negative and no real divergence occurs because U_D will be an imaginary number. Below the critical value, including all negative values for D_{16}/D_{11}, there will be a finite, real U_D.

The physical mechanisms which cause this to be so are readily apparent in Fig. 3a and b. Figure 3a is a plate with a substantial positive D_{16}. In this case, aerodynamic forces arising from plate displacements tend to return it to equilibrium, while just the opposite occurs with the plate having negative D_{16} (Fig. 3b).

For the case where there is a known, nonzero, initial angle of attack, and a known dynamic pressure, the static deflections of the structure (α and w_E) can be obtained by solving the equations of Eq. 2-41 simultaneously. For this study, only tip deflections are evaluated, because they were obtained experimentally.
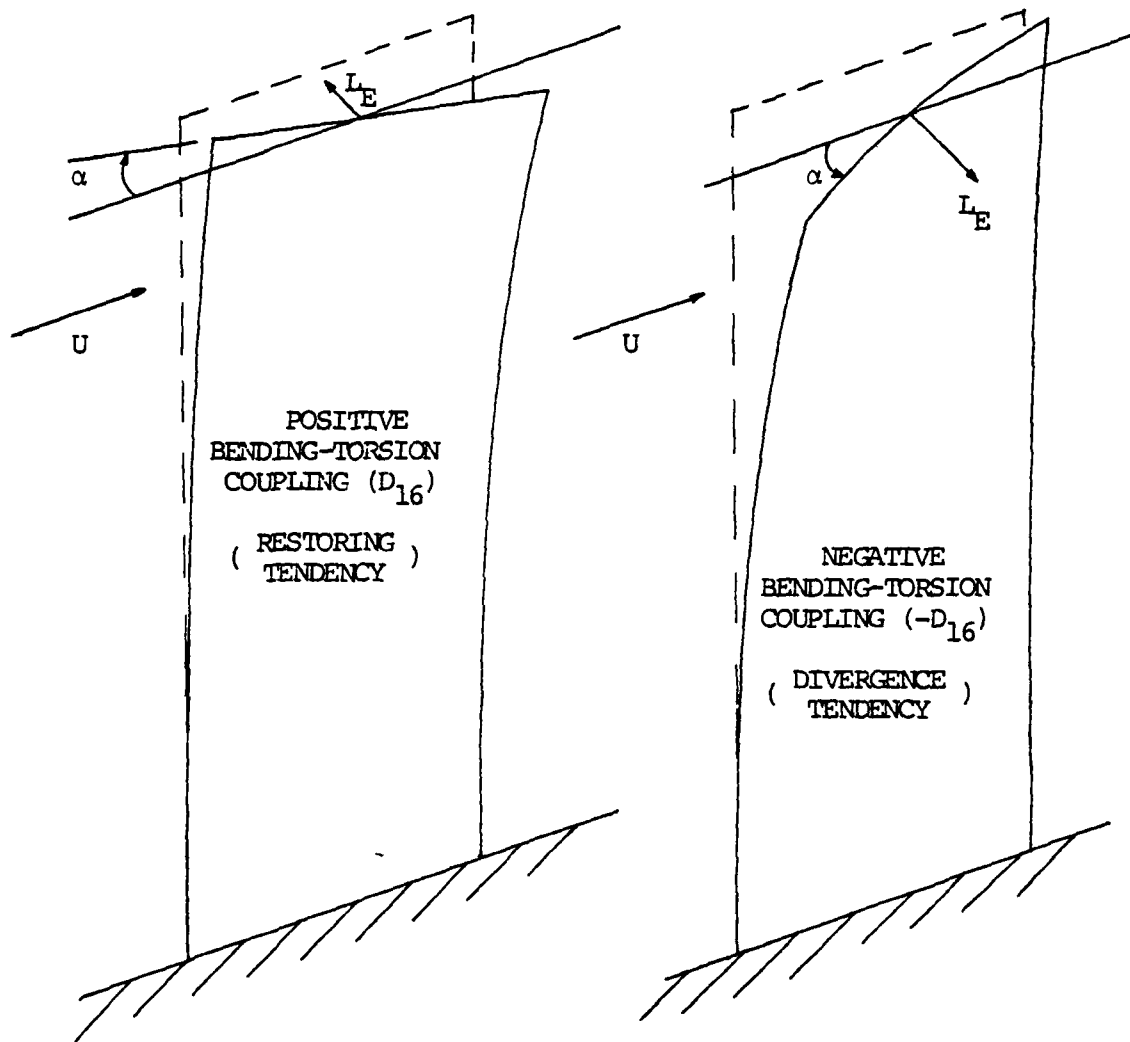
Figure 3. Static Deflection Behavior

Eq. 2-41 can be rewritten as

$$k_{11}q_1 + k_{12}q_2 = a_1\alpha_0 \qquad (2\text{-}45a)$$

$$k_{21}q_1 + k_{22}q_2 = a_2\alpha_0 \qquad (2\text{-}45b)$$

where

$$k_{11} = \frac{D_{11}c}{\ell^3} I_7$$

$$k_{12} = \frac{2D_{16}}{\ell^2} I_6 - q\ell \frac{\partial C_\ell}{\partial \alpha} I_3$$

$$k_{21} = \frac{2D_{16}}{\ell^2} I_6$$

$$k_{22} = [\frac{4D_{66}}{c\ell} (I_8 + \frac{D_{11}c^2}{48D_{66}\ell^2} I_{11} - \frac{qe\ell}{c} \frac{\partial C_\ell}{\partial \alpha} I_5]$$

$$a_1 = qc\ell \frac{\partial C_\ell}{\partial \alpha} I_1$$

$$a_2 = qe\ell \frac{\partial C_\ell}{\partial \alpha} I_2$$

By solving Eqs. 2-45a and b simultaneously, one obtains the following expressions for q_1 and q_2.

$$q_1 = \frac{a_2\alpha_0 - k_{22}q_2}{k_{21}} \qquad (2\text{-}46a)$$

$$q_2 = \frac{[a_1k_{21} - a_2k_{11}]}{[k_{12}k_{21} - k_{11}k_{22}]} \alpha_0 \qquad (2\text{-}46b)$$

The generalized deflections are then transformed to actual deflections (α_e and w_E) using Eqs. 2-9 and 2-10, where ϕ_1 and ϕ_α are evaluated at $x = \ell$. As before, α

(Fig. 2b) equals the sum of α_0 and α_e. The total angle of attack and bending deflection at the tip are

$$\alpha_{TIP} = [\ 1\ +\ \frac{\phi_\alpha(x=\ell)}{c}\ (\ \frac{a_1 k_{21} - a_2 k_{11}}{k_{12} k_{21} - k_{11} k_{22}}\ )]\alpha_0$$

(2-47a)

$$w_{E_{TIP}} = [\ \frac{a_2}{k_{21}} - \frac{k_{22}}{k_{21}}\ (\ \frac{a_1 k_{21} - a_2 k_{11}}{k_{12} k_{21} - k_{11} k_{22}}\ )]\phi_1(x=\ell)\ \alpha_0$$

(2-47b)

2.5 Free Vibration Problem

The free vibration problem is formulated by setting the generalized forces (Q_i) equal to zero in either Eqs. 2-25a and b, or Eqs. 2-29a, b and c. To make the equations of motion into algebraic equations instead of differential equations, one assumes that the motions of the plate will be harmonic. For harmonic (sinusoidal) motion, the generalized displacements can be expressed as

$$\dot{q} = qe^{i\omega t} \qquad \ddot{q} = -\omega^2 qe^{i\omega t} \qquad (2-48)$$

where ω is the frequency. These expressions are substituted into the differential equations of motion (Eqs. 2-25 and 2-29) to obtain the sinusoidal equations of motion. The sinusoidal equations of motion are presented here, in matrix

form, for both the two term and three term deflection equations.

Two term deflection equation:

$$\begin{bmatrix} (\dfrac{D_{11}c}{\ell^3}I_7) - \omega^2(mc\ell I_4) & (\dfrac{2D_{16}}{\ell^2}I_6) \\[3mm] (\dfrac{2D_{16}}{\ell^2}I_6) & [\dfrac{4D_{66}}{c\ell}(I_8 + \dfrac{D_{11}c^2}{48D_{66}\ell^2}I_{11})] - \omega^2(\dfrac{mc\ell}{12}I_5) \end{bmatrix} \begin{Bmatrix} q_1 \\[3mm] q_2 \end{Bmatrix} = 0$$

(2-49)

Three term deflection equation:

$$\begin{bmatrix} (\dfrac{D_{11}c}{\ell^3}I_7) - \omega^2(mc\ell I_4) & 0 & (\dfrac{2D_{16}}{\ell^2}I_6) \\[3mm] 0 & (\dfrac{D_{11}c}{\ell^3}I_{10}) - \omega^2(mc\ell I_{12}) & (\dfrac{2D_{16}}{\ell^2}I_9) \\[3mm] (\dfrac{2D_{16}}{\ell^2}I_6) & (\dfrac{2D_{16}}{\ell^2}I_9) & [\dfrac{4D_{66}}{c\ell}(I_8 + \dfrac{D_{11}c^2}{48D_{66}\ell^2}I_{11})] - \omega^2(\dfrac{mc\ell}{12}I_5) \end{bmatrix}$$

$$\times \quad \begin{Bmatrix} q_1 \\ q_2 \\ q_3 \end{Bmatrix} \quad = 0 \qquad (2-50)$$

One obtains a unique solution to either Eq. 2-49 or Eq. 2-50 by setting the determinant of the coefficient matrix equal to zero and solving for ω^2 (eigenvalue). The natural

vibration frequencies (ω_n) are obtained by taking the square
root of each eigenvalue. From Eq. 2-49, one obtains two
natural frequencies (first bending and first torsion), and
from Eq. 2-50, one obtains three natural frequencies (first
bending, second bending and first torsion).

To simplify calculations, the warping stiffness term

$$\frac{D_{11}c^2}{48D_{66}\ell^2}$$

has been eliminated because its contribution is small for
plates with moderate to high aspect ratios. The frequencies
obtained using the mode shapes in Appendix B are compared
in Chapter IV with experimentally obtained frequencies.

2.6 Aeroelastic Flutter Problem

The flutter problem is formulated using an indirect
method widely known as the U-g method. In this method,
the structural damping coefficient (g), introduced into
the equations of motion, is plotted versus velocity for
each vibration mode. Since solutions to the equations of
motion represent conditions for neutral stability, the
value of g obtained in this manner represents the amount
of damping that must be added to the structure to attain
neutral stability (flutter) at the given velocity. Therefore,

negative values of structural damping indicate that the structure is stable. Flutter will occur when the artificial structural damping equals the actual damping of the structure. To simplify calculations, the flutter problem will be formulated using only the equations of motion from the two term deflection equation.

The equations of motion (Eqs. 2-24a and b), as derived in Section 2.2, again assuming sinusoidal motion and neglecting the warping stiffness contribution, are

$$-\omega^2 \ [M_{ij}] \ \begin{Bmatrix} q_1 \\ q_2 \end{Bmatrix} + \ [K_{ij}] \ \begin{matrix} q_1 \\ q_2 \end{matrix} \ = \ \begin{Bmatrix} Q_1/e^{i\omega t} \\ Q_2/e^{i\omega t} \end{Bmatrix}$$

$$(2-51)$$

where

$$[M_{ij}] \ = \ \begin{bmatrix} mc\ell I_4 & 0 \\ 0 & \dfrac{mc\ell}{12} I_5 \end{bmatrix}$$

$$[K_{ij}] \ = \ \begin{bmatrix} \dfrac{D_{11}c}{\ell^3} I_7 & \dfrac{2D_{16}}{\ell^3} I_6 \\ \dfrac{2D_{16}}{\ell^2} I_6 & \dfrac{4D_{66}}{c\ell} I_8 \end{bmatrix}$$

and the generalized forces (Q_i) obtained from Eq. 2-20 are

$$Q_1 = \int_0^{\ell} \phi_1 L_E \, dx \qquad\qquad (2\text{-}52a)$$

$$\text{where } L_E = \int_{-\frac{c}{2}}^{-\frac{c}{2}} p_z \, dy$$

$$Q_2 = \int_0^{\ell} \frac{\phi_\alpha}{c} M_E \, dx \qquad\qquad (2\text{-}52b)$$

$$\text{where } M_E = \int_{-\frac{c}{2}}^{-\frac{c}{2}} y \, p_z \, dy$$

Since aerodynamic forces and moments obtained by assuming steady flow are generally inadequate for realistic flutter calculations, complete unsteady aerodynamic expressions will be used. Unsteady aerodynamic lift (L_E) and moment (M_E) expressions derived in Ref. 13 have been suitably transformed to the coordinate system in Fig. 2. The reader is cautioned that the coordinate system used throughout this study differs from the standard aeroelastic coordinate system used in Ref. 13. The difference being the $+w_E$ here is $-h$ in Ref. 13. The aerodyanmic expressions are

$$L_E = \pi\rho b^2 [-\ddot{w}_E + U\dot{\alpha} - ba\ddot{\alpha}] + 2\pi\rho UbC\,(k)\,[-\dot{w}_E$$

$$+ U\alpha + b(1/2 - a)\dot{\alpha}] \qquad\qquad (2\text{-}53a)$$

$$M_E = \pi\rho b^3 [-a\ddot{w}_E - U(1/2 - a)\dot{\alpha} - b(1/8 + a^2)\ddot{\alpha}] +$$

$$\pi\rho Ub^2 (1/2 + a)\,C(k)\,[-\dot{w}_E + U\alpha + b(1/2 - a)\dot{\alpha}]$$

$$(2\text{-}53b)$$

43

where   b = semichord

a = (distance EA is aft of midchord)/b   (zero in this study)

k = reduced frequency ($\omega b/U$)

$C(k)$ = Theodorsen function

Assuming sinusoidal motion

$$w_E = w_E e^{i\omega t} \qquad \alpha = e^{i\omega t}$$

$$\dot{w}_E = i\omega w_E e^{i\omega t} \qquad \dot{\alpha} = i\omega \alpha e^{i\omega t}$$

$$\ddot{w}_E = -\omega^2 w_E e^{i\omega t} \qquad \ddot{\alpha} = -\omega^2 \alpha e^{i\omega t}$$

the aerodynamic expressions, after some algebraic manipulation, become

$$L_E = \omega^2 \pi \rho b^3 \{ [L_1 + iL_2] \frac{w_E}{b} + [L_3 + iL_4]\alpha \} e^{i\omega t}$$

(2-54a)

where $[L_1 + iL_2] = 1 - \frac{2i}{k} C(k)$

$$[L_3 + iL_4] = a + \frac{2C(k)}{k^2} + \frac{i}{k} [1 + (1 - 2a) C(k)]$$

$$M_E = \omega^2 \pi \rho b^4 \{ [M_1 + iM_2] \frac{w_E}{b} + [M_3 + iM_4]\alpha \} e^{i\omega t}$$

(2-54b)

where $[M_1 + iM_2] = a - i \frac{(1 + 2a)}{k} C(k)$

$$[M_3 + iM_4] = (1/8 + a^2) + \frac{(1 + 2a)}{k^2} C(k)$$

$$+ \frac{i}{k} [(1/2 - 2a^2) C(k) - (1/2 - a)]$$

Equations 2-54a and b are substituted into Eqs. 2-52a and b.
One observes that, since the plate in this study has a con-
stant chord, variables b, $[L_1 + iL_2]$, $[L_3 + iL_4]$,
$[M_1 + iM_2]$, and $[M_3 + iM_4]$ are not functions of x and
can be brought outside the integral. Making use of the trans-
formation equations (2-9 and 2-10), and expressing the integ-
rals in nondimensional form, we arrive at the final expres-
sions for the generalized forces.

$$Q_1 = \omega^2 \pi \rho b^3 \{ \frac{[L_1 + iL_2] \ell I_4}{b} q_1 +$$

$$\frac{[L_3 + iL_4] \ell I_3}{c} q_2 \} e^{i\omega t} \qquad (2\text{-}55a)$$

$$Q_2 = \omega^2 \pi \rho b^4 \{ \frac{[M_1 + iM_2] \ell I_3}{bc} q_1 +$$

$$\frac{[M_3 + iM_4] \ell I_5}{c^2} q_2 \} e^{i\omega t} \qquad (2\text{-}55b)$$

where $\quad I_3 \equiv \frac{1}{\ell} \int_0^\ell \phi_1 \phi_\alpha \, dx$

$$I_4 \equiv \frac{1}{\ell} \int_0^\ell \phi_1^2 \, dx$$

$$I_5 \equiv \frac{1}{\ell} \int_0^\ell \phi_\alpha^2 \, dx$$

Substituting Eqs. 2-56a and b into Eq. 2-51 and can-
celing $e^{i\omega t}$ yields a new form of the equations of motion,
which are written here in contracted matrix form.

$$[\underline{\underline{K}} - \omega^2 \underline{\underline{A}}] \underline{q} = 0 \tag{2-56}$$

where the elements of the K_{ij} and A_{ij} matrices are given as

$$K_{11} = \frac{cD_{11}}{\ell^3} I_7$$

$$K_{12} = \frac{2D_{16}}{\ell^2} I_6$$

$$K_{21} = \frac{2D_{16}}{\ell^2} I_6$$

$$K_{22} = \frac{4D_{66}}{c\ell} I_8$$

$$A_{11} = mc\ell I_4 + \pi\rho b^2 I_4 [L_1 + iL_2]$$

$$A_{12} = \pi\rho \frac{\ell b^3}{c} I_3 [L_3 + iL_4]$$

$$A_{21} = \pi\rho \frac{\ell b^3}{c} I_3 [M_1 + iM_2]$$

$$A_{22} = \frac{mc\ell}{12} I_5 + \pi\rho \frac{\ell b^4}{c^2} I_5 [M_3 + iM_4]$$

Structural damping is proportional to, and opposes,
the deflection of the structure. The structural damping
coefficient (g) is introduced into Eq. 2-56 by multiplying
the B matrix by (1 + ig). The methodology behind this step

is treated in depth in Ref. 13. An assumption here is that the linear damping coefficient (g_h) is equal to the rotary damping coefficient (g_α). It is also convenient to divide Eq. 2-56 by $-\omega^2$ and combine it with the $(1 + ig)$ term to form a complex eigenvalue (Z), defined as

$$Z \equiv (\frac{1 + ig}{\omega^2}) \qquad (2\text{-}57)$$

Equation 2-53 now becomes

$$[\underline{A} - \underline{K}Z] \underline{q} = 0 \qquad (2\text{-}58)$$

where the elements of $\underline{K}$ are real and the elements of $\underline{A}$ are complex. The matrix $[\underline{A} - \underline{K}Z]$ is put into standard eigen-value form by premultiplying by $\underline{K}^{-1}$, resulting in

$$[\underline{K}^{-1}\underline{A} - \underline{I}Z] \underline{q} = 0 \qquad (2\text{-}59)$$

where $\underline{I}$ is an identity matrix. A unique solution to Eq. 2-59 is obtained by setting the determinant of the coefficient matrix equal to zero, and solving for Z. For a 2 x 2 matrix, the two Z-values correspond to the two plate vibration modes (first bending and first torsion).

The solution procedure is to pick a value for the reduced frequency (k) and solve Eq. 2-59 for Z_i. The frequency structural damping coefficient and velocity are obtained from Z by the following relations.

$$\omega = \frac{1}{\sqrt{Re\{Z\}}} \qquad g = \frac{Im\{Z\}}{Re\{Z\}} \qquad U = b\omega/k \qquad (2\text{-}60a,b,c)$$

A new k value is chosen and the procedure is repeated. Finally, a U-g diagram is created by plotting the structural damping for each root (Z) versus velocity, or a nondimensional flutter speed $(U/b\omega_\alpha)$, were ω_α is the torsional natural vibration frequency. One can get a reasonable approximation for ω_α by picking a very large value for k and solving Eqs. 2-59 and 2-60a for the torsion root. This is essentially the structural vibration frequency when U equals zero. U-g diagrams for all the laminated plates considered in this study appear in Appendix B. The flutter velocity (U_F) was conservatively chosen to be the point where the damping coefficient from either root first crosses the U-axis.

Solving the flutter problem is further complicated by the presence of the Theodorsen function (C(k)). The Theodorsen function is a nonrational functional which can be expressed exactly in terms of modified Bessel functions of the second kind. Since Eq. 2-59 was to be implemented on a digital computer and solved many times for different values of k, an approximation for C(k) was desired. By taking the Laplace Transform of R.T. Jones' exponential approximation, one obtains a rational expression for C(k). This expression is[16]

$$C(s) = \frac{0.5s^2 + 0.2808s + 0.01365}{s^2 + 0.3455s + 0.01365} \qquad (2\text{-}61)$$

where s is ik.

The flutter problem is now completely defined. For actual computation, taking the determinant of the 2 x 2 coefficient matrix is straightforward, the only complications being that (1) the K-matrix must first be inverted and (2) that the coefficients of the A-matrix are all complex. Because of the simplicity of the problem, the temptation is to solve it manually. However, be advised that a typical U-g plot requires on the order of 20 data points. Each data point requires that Eq. 2-59 be solved for a new k value.

49

CHAPTER III

EXPERIMENTS

3.1 Test Specimen Selection

Prior to making any test specimens, criteria which defined desirable, and sometimes essential, characteristics of the test specimens were established. These criteria included

(1) Test specimens must exhibit a wide range of bending-torsion coupling stiffness.

(2) Test specimens must be rectangular, constant thickness, flat plates with zero sweep. The requirement for a flat plate dictated using a symmetric laminate, since an unsymmetric laminate would warp during cure.

(3) Test specimens would be made from Hercules AS/3501-6 graphite/epoxy since it was available at M.I.T.

(4) Test specimens would have an aspect ratio of four, since this would be representative of an aircraft wing with an aspect ratio of eight.

(5) Test specimens should exhibit flutter and divergence within the 0 - 30 m/sec speed range of the acoustic wind tunnel at M.I.T.

(6) The test specimens should be small enought to be made using standard TELAC (Technology Laboratory for Advanced Composites) ply cutting templates and curing

plates. Additionally, a small size was desirable be-
cause the effect of slight material warping, often
encountered during curing, would be minimized.

(7) The laminate should be able to withstand repeated
large static and oscillatory loads.

Criteria five and six directly oppose one another when
trying to arrive at an optimum design. Trying to satisfy
both of them dictated a very thin plate. Also, to achieve
substantial bending-torsion coupling, an unbalanced lamina-
tion scheme was chosen. Unbalanced laminates have an unequal
number of $+\theta$ and $-\theta$ plies. However, a midplane symmetric
ply arrangement was still required. Carrying the unbalance
to the limit results in a unidrectional laminate with all
plies at $+\theta$ or all plies at $-\theta$. To improve the toughness
(criterion seven) of a unidirectional, off-axis laminate, the
center two plies would have a zero-degree ply angle. The
total thickness was chosen to be six plies. Five different
laminates were selected as representative of a wide range
of bending-torsion coupling stiffnesses, both positive and
negative. The first two laminates, $[+30_2/0]_s$ and $[-30_2/0]_s$,
were chosen because a unidirectional laminate with $\theta = 30°$
exhibits the highest bending-torsion coupling stiffness
(D_{16}) [11]. The next two laminates, $[+45_2/0]_s$ and $[-45_2/0]_s$,
were chosen because a unidirectional laminate with $\theta = 45°$
exhibits the highest torsion stiffness (D_{66}), but still has

a large D_{16}. The final laminate, $[0_2/90]_s$, was chosen because a unidirectional laminate with $\theta = 0°$ exhibits the highest bending stiffness (D_{11}) and zero D_{16}. During the test program, another laminate, $[\pm45/0]_s$, was added because it had the same theoretical D_{11} and D_{66} as $[+45_2/0]_s$, with less D_{16}. To minimize the number of test specimens which had to be constructed, the $[+\theta_2/0]_s$ and $[-\theta_2/0]_s$ test specimens were actually the same laminate, simply rotated 180 degrees about the x-axis (Fig. 1)

The test specimens would have to have an overall length of 330 mm (13 in) and a chord of 76 mm (3 in), because this was the largest size that could be constructed satisfying criteria four and six. The overall length included a 25 mm (1 in) loading tab, making the effective cantilever plate length 305 mm (12 in). Finally, in an effort to minimize plate stiffness, an airfoil shaped fairing would not be used on the plate for wind tunnel tests. This had the added advantage of making the plate stiffness easier to calculate.

3.2 Test Specimen Preparation

The test specimens were constructed from Hercules AS/3501-6 graphite/epoxy prepreg tape from Lot No. 1643. The tape was 305 mm (12 in) wide and had a nominal thickness of 0.134 mm (0.00528 in). Individual plies were cut

to the proper size and angular orientation using aluminum templates, and assembled into 305 mm (12 in) by 356 mm (14 in) laminates. The laminates and curing materials (Appendix C) were arranged on an aluminum curing plate especially designed by students in TELAC for use with graphite/ epoxy laminates having a length and width as stated above. The laminates were cured in a Baron model BAC-35 autoclave using the cure cycle listed in Appendix C. After curing, the laminates were post-cured in a forced air circulation oven at 350° F for eight hours. After post-curing, a rectangular test specimen 330 mm (13 in) long and 76 mm (3 in) wide was cut from each of the four laminates using a diamond coated cutting wheel mounted on an automatic feed, milling machine.

The thickness of a graphite/epoxy plate tended to vary over its surface. Therefore, the plate thickness was measured at several different locations and averaged. The same procedure was followed in measuring the length and width, although the variation was much less. The averaged measurements for each test specimen appear in Appendix D, along with the nominal values. The thickness variation between laminates (all were six ply) was 0.033 mm (0.0013 in) with the average being 0.807 mm (0.0318 in). This compared favorably to the nominal thickness of 0.804 mm (0.0317 in) for a six ply laminate. The laminates were also weighed on a triple beam balance, from which the material density

(ρ) for each test specimen was calculated. The average density was 1.53×10^3 kg/m^3 (0.0554 lb/in^3) with a maximum variation of 0.06×10^3 kg/m^3 (0.0022 lb/in^3). This again compared favorably with a nominal density of 1.52×10^3 kg/m^3 (0.055 lb/in^3) for graphite epoxy.

Loading tabs 83 mm (3.25 in) x 25.5 mm (1 in) were machined from 2.4 mm (0.094 in) aluminum plate and bonded to the base of each test specimen with epoxy, cured at room temperature. The loading tabs were intended to aid in aligning the test specimen in the clamping fixture and to prevent damage to the plate surface fibers.

To get an indication of the lateral deflections the plate would experience during the wind tunnel tests, strain gauges were attached to the base of each test specimen at the midchord, as shown in Fig. 4. Two Micro Measurements EA-03-187BB-120 strain gauges, from Lot. No. R-A21ABO2 with a gauge factor of 2.085, were attached to each test specimen (one on each side) to measure bending strain. Two BLH-SR4; FAED-25B-12-59; Serial No. 5-AE-SC strain gauge rosettes from Lot No. A-315 with a gauge factor of 2.01 were attached to each test specimen (one on each side) to measure torsion strain. The two bending gauges were wired together as a two-arm bridge circuit with three external lead wires approximately 305 mm (12 in) long. The two torsion gauges were wired together as a four-arm bridge circuit with four external lead wires. Wiring the strain gauges on either side of the
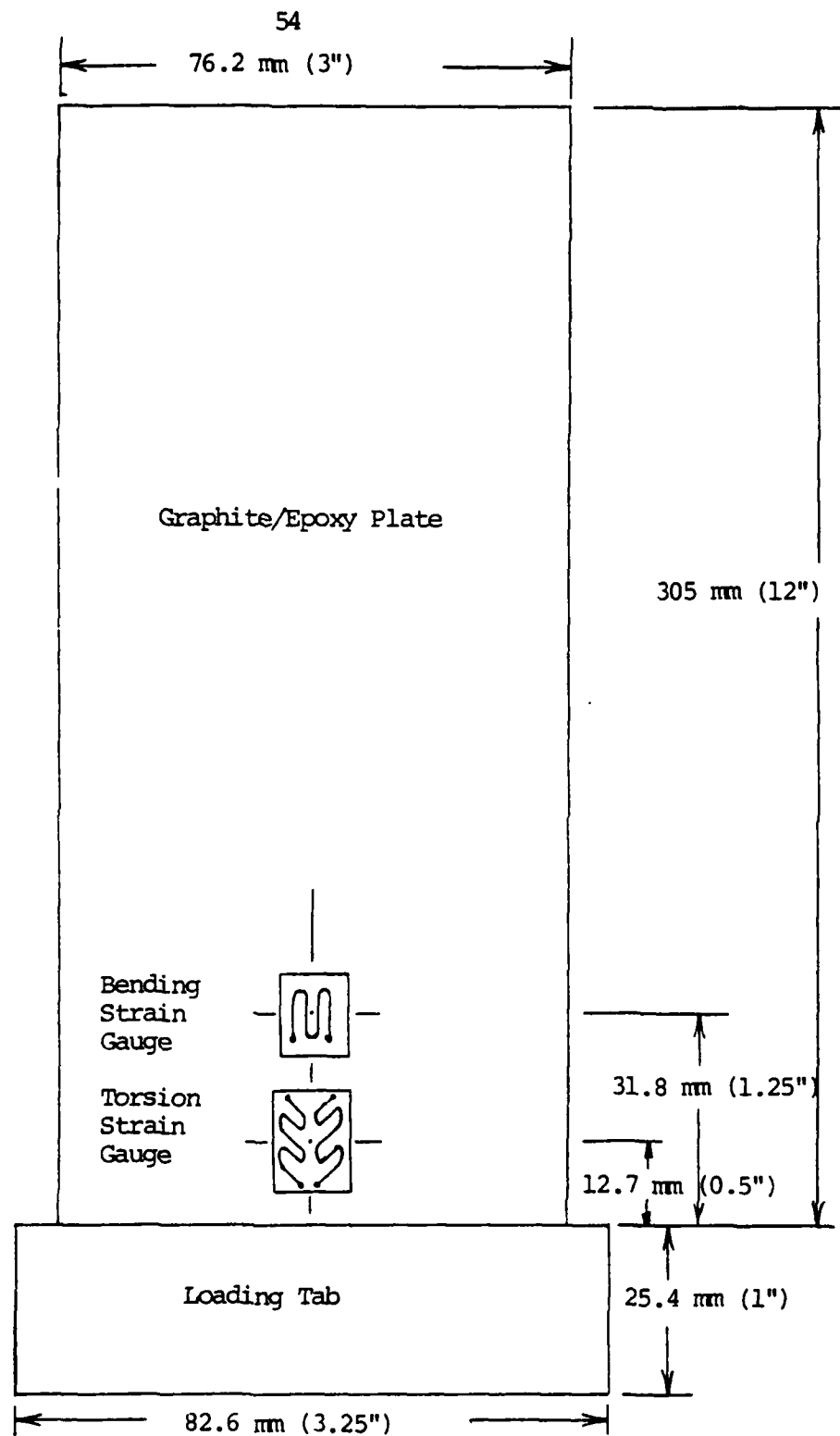
Figure 4. Sample Test Specimen

plate together, in this manner, doubled the signal output
for each channel (bending and torsion) and provided auto-
matic temperature compensation. This temperature compen-
sation was very important during the wind tunnel tests, where
air flowing over an uncompensated gauge would cause a zero
shift as the tunnel velocity was varied. The final step,
after all solder connections had been made, was to coat the
gauges with Micro Measurements M-Coat A, an air-drying poly-
urethane, for protection.

3.3 Test Apparatus and Procedure

(a) Static Deflection Tests

The static deflection test setup is shown in Fig. 5.
It consisted of a 330 mm (13 in) x 508 mm (20 in) plywood
base with six vertical steel rods approximately 760 mm
(30 in) long. The test specimen was clamped in a vise
machined from a 25.4 mm (1 in) x 152 mm (6 in) x 229 mm
(9 in) aluminum block, which was bolted to the base of the
test fixture. Two removable, low friction, pulleys were
attached to the vertical rods such that a force or moment
could be applied to the test specimen at any location along
its length. Rulers, graduated in 32nd's of an inch, were
also attached to the vertical rods to facilitate measuring
the test specimen's edge deflections. A deflection indicator
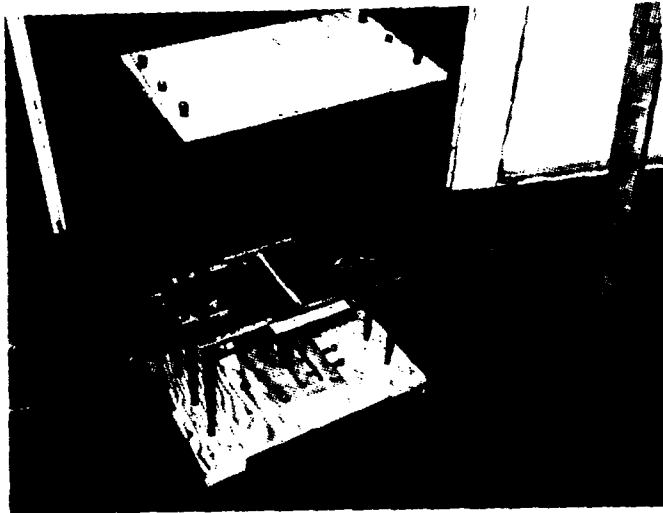
(a)   Force Test

(b)   Moment Test

Figure 5.   Influence Coefficient Test Apparatus

was constructed out of balsa wood. It had needle pointers on the ends and cotton threads attached to its midpoint and ends. The threads, when routed over the pulleys and attached to weights, transferred a force or moment to the test specimen (Fig. 5).

The deflection indicator was aligned with the lines scribed on the test specimen at the 3/4 length point, and the test specimen was clamped in the vise. The pulleys were clamped to the middle two vertical rods (Fig. 5a) at the proper height, and threads from the center of the deflection indicator were routed over the pulleys. The rulers were adjusted to the proper height and zeroed with respect to the deflection indicator pointers. Weights of 10, 20, 30, and 40 grams were successively attached to the threads, first to give positive deflections, then to give negative deflections. As each weight was attached, the readings from both pointers were recorded, along with the weight.

Next, the pulleys were moved to the corner rods (Fig. 5b) and the end threads were routed over them, so as to provide a positive moment when the weights were attached. Weights of 10, 20, 33.9, and 43.9 grams were successively attached to each thread of the couple, and readings from both pointers were again recorded along with the weights. The pulleys were then switched to the corner rods on the opposite diagonal, and the procedure was repeated for a negative moment.

For each data point, the lateral deflection of the elastic axis (w_E) and the rotation of the test specimen about the elastic axis (α) were calculated using the data reduction formulas in Appendix E. The lateral deflections obtained from the load test (Test 1) were plotted versus load, with the slope being the bending flexibility influence coefficient (c_{11}). The angular deflections (α) from Test 1 were plotted versus load, yielding the bending-torsion coupling flexibility influence coefficient (c_{21}). The angular deflections obtained from the moment test (Test 2) were plotted versus moment, yielding the torsion flexibility influence coefficient (c_{22}). The lateral deflections obtained from Test 2 were plotted versus moment to obtain the other bending-torsion coupling flexibility influence coefficient (c_{12}). The flexibility influence coefficient plots for the four test specimens appear in Appendix E. The flexibility influence coefficients for a $[+\theta_2/0]_s$ and a $[-\theta_2/0]_s$ laminate will be the same, except for the sign on c_{12} and c_{21}, since they were physically the same test specimen. Finally, the flexibility influence coefficients for each test specimen were arranged in a 2 x 2 matrix ($\underline{C}$) and inverted to obtain the stiffness influence coefficient matrix ($\underline{K}$). The results of the static deflection tests are discussed in Section 3.4.

(b)   Free Vibration Tests

The free vibration test setup, shown in Fig. 6, used the same vise as the static deflection tests. The vice was suspended by four spring steel strips, which allowed it to translate along the z-axis (Fig. 2), but restricted motion in all other directions. The vise was rigidly attached to a horizontally mounted Ling model 420 shaker using a cylindrical aluminum adapter. The shaker had a peak force of 445 N (100 lbs) and a frequency range of approximately 5 to 3000 Hz. Since the shaker was driven by an audio amplifier, there was a certain amount of distortion to the sine wave output signal below 20 Hz. For some vibration tests, an Endevco model 7701-50 "Isoshear" accelerometer was mounted to the vise by a threaded mounting stud, and an Endevco model 222B "Micro-miniature" accelerometer was mounted to the test specimen, within 25 mm of the base, using Eastman 910 adhesive. The outputs of these accelerometers, after passing through special amplifiers, were connected to a Tektronix type 502 dual beam oscilloscope so that both outputs could be displayed simultaneously. Finally, a digital signal counter was attached directly to the signal generator to provide an accurate frequency readout.

The test specimen was aligned and clamped in the vise. A white paper screen was suspended behind the test specimen
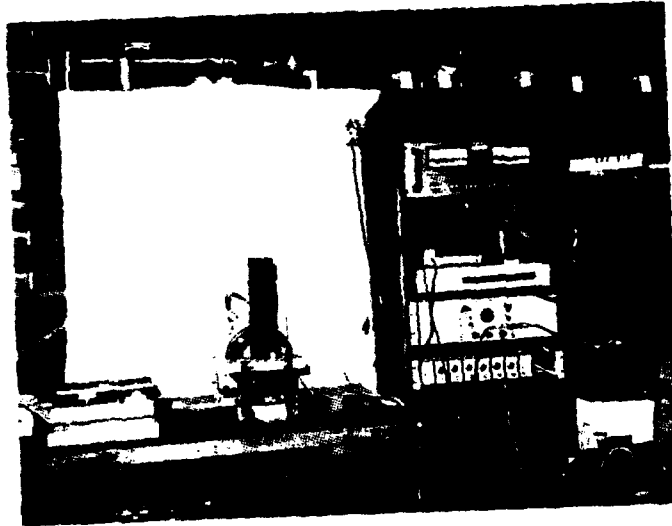
(a)   Front View
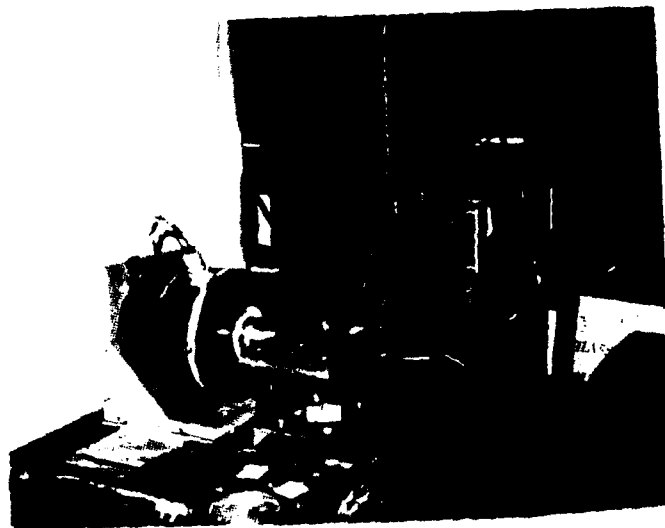
(b)   Side View

Figure 6.   Free Vibration Test Apparatus

to aid in observing the vibration modes. The test began with the signal generator set at, or below, 3 Hz. The frequency was slowly increased until the first bending mode was excited. The frequency was very finely adjusted until the vibration amplitude peaked, as observed visually, and the frequency was recorded. This procedure was repeated for the second bending and first torsion vibration modes. Since flutter is normally associated with the lower (bending and torsion) vibration modes, only the first bending, second bending and first torsion frequencies were obtained for each specimen.

In an effort to improve the accuracy and repeatability of the frequencies, the dual beam oscilloscope was used to observe the accelerations of the vise and the test specimen. The resonance frequency was defined as the frequency where a 90° phase shift occurred between the two accelerometer traces. If a complete 90° phase shift did not occur, then the resonance frequency was taken to be the frequency where the maximum phase shift occurred. In an attempt to obtain a clear phase shift at the first torsion natural mode, the specimen-mounted accelerometer was moved to different chord-wise locations, all the way to the edge of the test specimen. The results of the free vibration tests are discussed in Section 3.4.

(c)   Wind Tunnel Tests

All wind tunnel tests were performed in the M.I.T.,
Department of Aeronautics and Astronautics, acoustic wind
tunnel. The acoustic wind tunnel is a continuous flow tun-
nel with a 1.5 m (5 ft) x 2.3 m (7.5 ft) free jet test sec-
tion 2.3 m (7.5 ft) long, located inside a large anechoic
chamber. The tunnel was powered by a 100 HP motor giving
it a continuously variable velocity range of 0 to 32 m/sec
(0 to 105 ft/sec). The tunnel control panel was located
outside the anechoic chamber. The velocity was controlled
by two levers (coarse and fine speed control). The coarse
lever controlled the motor field current and was variable
in fixed step increments only. The fine lever controlled
the motor shunt current and was continuously variable.
The total current being drawn by the motor, along with
voltage, were displayed at the control panel on analog
gauges. There was a 400 amp current limitation on the motor,
which was protected by circuit breakers. The tunnel velo-
city was read from an alcohol manometer, calibrated in
inches of alcohol, and located at the control panel. The
manometer was connected to a pitot tube located slightly
forward of the test section. A hydraulic motor, recessed
into the floor of the test section, provided a means of
mounting the test apparatus.

The test setup, shown in Fig. 7, consisted of a turntable machined from aluminum mounted on a 635 mm (25 in) tall pedestal made of 152 mm (6 in) steel pipe. The pedestal was, in turn, mounted to the floor of the wind tunnel test section. The vise from the static deflection tests was fastened to the free rotating portion of the turntable. A wooden cover disk 508 mm (20 in) in diameter, shown removed in Fig. 7a and attached in Fig. 7b, was used to provide smooth airflow past the test specimen. The disk, which had the angle of attack marked on its edge in 2° increments up to 18°, rotated with the test specimen. A pointer attached to the fixed base provided a consistent means of reading the angle of attack. An aluminum rod, attached to to the disk and extending outside the test section, allowed the angle of attack to be varied while the test was in progress.

A terminal strip attached to the underside of the disk provided a convenient means of connecting the test specimen strain gauge lead wires to the instrumentation wiring harness. The instrumentation system was a Gould 2400 series four channel strip chart recorder. The recorder had a four arm D.C. bridge preamplifier installed in channel 1 and a two arm D.C. bridge preamplifier installed in channel 2. The recorder also had an internal time base generator which marked the strip chart at one second intervals. The preamplifier had
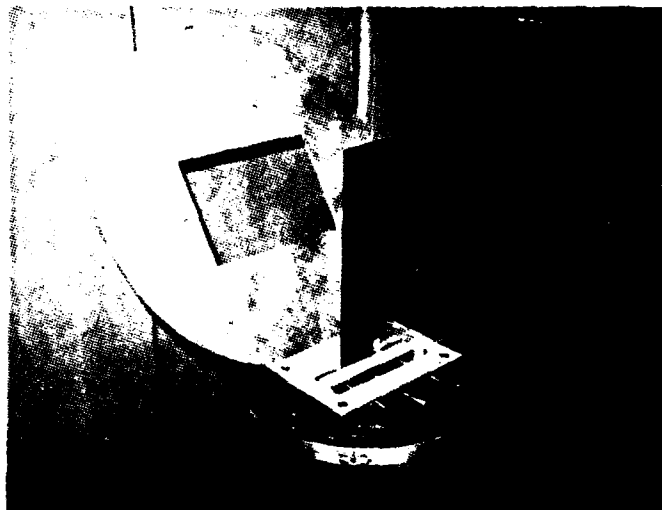
(a)   Cover Disk Removed
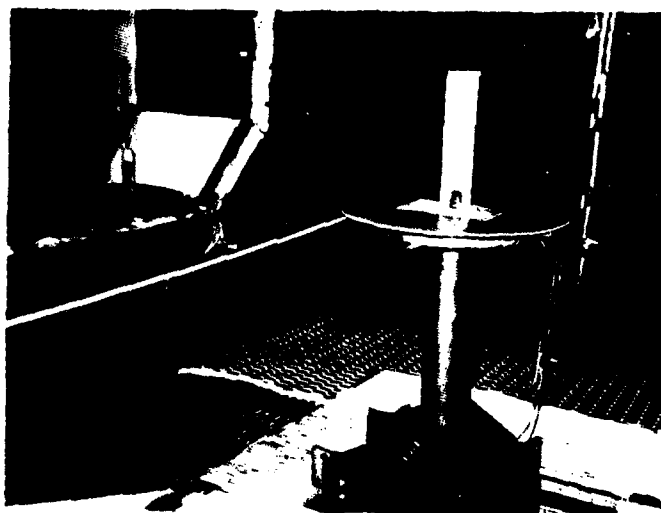
(b)   Cover Disk Attached

Figure 7. Wind Tunnel Test Apparatus

the capability of both attenuating and amplifying the input signal. The strip chart speed could be set at 5, 10, 25, 50, 100, and 200 mm/sec plus each speed could be divided by 100. The chart speed was accurate to $\pm$ 0.5%. To provide a record of the test specimen deflections, the torsion strain gauge was attached to channel 1 and the bending strain gauge was attached to channel 2.

The test specimen was aligned and clamped in the vise. The cover disk was installed, and all gaps were covered with tape. The strain gauge lead wires were attached to the terminal strip, and the strip chart recorder was adjusted according to the manufacturer's instructions. The test number and test specimen, along with test section temperatures and atmospheric pressure, were recorded on a data sheet. The first three natural vibration frequencies were recorded on the strip chart by giving the test specimen a bending deflection and letting it oscillate, then giving it a torsion deflection and letting it oscillate. Static calibrations were performed by giving the test specimen a series of known pure bending and torsion tip deflections and appropriately annotating the strip chart deflections.

The angle of attack was adjusted to zero, and the wind tunnel was started and set at a low velocity (< 8 m/sec; 25 ft/sec). After the velocity stabilized, a reading was taken from the alcohol manometer andannotated on the strip

chart, in inches of alchol. The angle of attach was then swept from 0° to 12° (sometimes to 18° if deemed appropriate) in 2° increments, while the velocity was held constant. Each angle of attack was annotated on the strip chart. The angle of attack was returned to zero and the tunnel speed increased slightly. The new manometer reading was annotated on the strip chart, and the angle of attack sweep was repeated. The strip chart recorder was run at 1 mm/sec for most of the test. When oscillation was detected, a two second expanded record (100 or 200 mm/sec) was made. For some test specimens, at higher angles of attack, the oscillations would begin very abruptly. To get better data on the angle of attack, where flutter actually started, the angle of attack was increased in 1° increments in this region. This test procedure was repeated until either the the maximum tunnel speed was reached, or the test specimen deflections became excessive. At higher tunnel speeds, the maximum angle of attack tested was reduced to prevent damage to the test specimen. For the specimens which exhibited flutter at zero angle of attack, the normal procedure was to obtain two or three more data runs at velocities slightly higher than the velocity where the test specimen fluttered at zero angle of attack.

Divergence testing often results in the destruction of a test specimen. Since this was not a desirable result,

wind tunnel speeds were increased in very small increments as the divergence velocity was approached. The deflections of the test specimen were closely monitored, and when it would no longer return to a zero deflection state, the tunnel velocity was not increased further. The extreme flexibility of the test specimens also increased the allowable margin for error.

Finally, after all the desired data was taken, the tunnel was shut down and the temperature of the test section was recorded on the data sheet. Since the wind tunnel was a continuous flow variety, temperature increases of up to 10° F were encountered during test runs. The test specimen was removed from the vise and another test specimen installed. When going from a $[+\theta_2/0]_s$ specimen to a $[-\theta_2/0]_s$ specimen, the turntable was simply rotated 180 degrees, while the specimen remained undisturbed. The test procedure was then repeated for the new test specimen.

After the wind tunnel tests were complete, the manometer readings were converted to indicated velocity, and then to true velocity using the conversions in Appendix E. The temperature used for the true velocity correction was the average of the start and finish temperature for each run. The oscillation frequencies were obtained manually and annotated on the strip chart, along with the indicated velocity. The static calibrations were used to obtain an

approximate relationship between test specimen deflection and strain gauge output using the procedure outlined in Appendix E. This relationship was used, on selected tests, to calculate the test static deflections (not oscillation deflections). The peak to peak oscillation amplitude of the bending and torsion strain gauges, on selected tests, was also annotated on the strip chart. Finally, the flutter boundary velocities, along with the dimensionless reduced flutter speeds $(U/b\omega_\alpha)$ were plotted versus angle of attack for each test specimen. On selected tests, the test specimen deflection, for a given angle of attack, was plotted versus velocity. Also, flutter amplitude, for a given angle of attack, was plotted versus velocity for selected tests. These test results are discussed in Section 3.4.

3.4 Test Results

(a) Static Deflection Tests

The flexibility influence coefficients (c_{ij}) which are a measure of the structure's deflection for a given load, were obtained by determining the slope of the lines plotted in Appendix E. All the plots were linear, with the exception of c_{22} for the $[0_2/90]_s$ test specimen. For this plot, a linear approximation was used to determine the slope. The data scatter on all the plots was less than 10%. The flexibility influence coefficients could have been arranged in

a 2 x 2 matrix and inverted to obtain the stiffness influence
coefficients (k_{ij}), which are a measure of the force a struc-
ture exerts for a given displacement. However, for this
section, the flexibility influence coefficients will be exa-
mined directly. Table 1 lists the experimentally obtained
inflence coefficients for each test specimen.

TABLE 1

EXPERIMENTAL FLEXIBILITY INFLUENCE COEFFICIENTS

Test Specimen	c_{11} (ft/lb)	c_{12} (ft/ft·lb)	c_{21} (rad/lb)	c_{22} (rad/ft·lb)	Coupling Factor (κ)
$[0_2/90]_s$	0.18	−0.03	−0.02	2.3	0.0014
$[\pm45/0]_s$	0.60	−0.16	−0.13	1.06	0.033
$[+45_2/0]_s$	0.98	−0.76	−0.75	2.7	0.22
$[-45_2/0]_s$	0.98	+0.76	+0.75	2.7	0.22
$[+30_2/0]_s$	0.64	−0.80	−0.82	3.0	0.34
$[-30_2/0]_s$	0.64	+0.80	+0.82	3.0	0.34

A measure of the accuracy of these static deflection
tests was that, according to Maxwell's Law of Reciprocal
Deflections, c_{12} must equal c_{21}. All of the test specimens
showed excellent agreement in this area.

The coupling factor (κ), included in Table 1, was de-
fined as

$$\kappa \equiv \frac{c_{12}c_{21}}{c_{11}c_{22}}$$

and was a dimensionless measure of the amount of bending-torsion coupling a test specimen possessed. One observes that going from a balanced to an unbalanced laminate significantly increased the coupling. Also, the $[+30_2/0]_s$ and $[-30_2/0]_s$ test specimens had the highest coupling of those tested.

In going from the balanced $[\pm45/0]_s$ test specimen to the unbalanced $[+45_2/0]_s$ test specimen, the torsional flexibility (c_{22}) increased by a factor of 2.5, and the bending flexibility (c_{11}) increased by a factor of 1.6. The reader should also note that the $[+30_2/0]_s$ test specimen was more flexible in torsion than the $[0_2/90]_s$ test specimen.

(b) Free Vibration Tests

Excitation of the torsion vibration mode was extremely difficult on the $[0_2/90]_s$ and the $[\pm45/0]_s$ test specimens, which had very little bending-torsion coupling. Additionally, the torsion mode was only lightly excited on the other test specimens. The accelerometer bonded to the test specimen was also largely unsuccessful for the torsion mode, because the phase shift was very slight. Since the shaker was driven by an audio amplifier, the output signal was distorted below 20 Hz. This made using an oscilloscope to detect phase shift in the first bending mode difficult. The phase shift technique did, however, work well for the

second bending mode.

Frequencies of the lowest three natural vibration modes, obtained from both the shaker and wind tunnel tests, are tabulated in Appendix E. The averaged frequencies for each test specimen appear in Table 2. Frequencies from both sources were all within 3% of the average. The $[+\theta_2/0]_s$ and $[-\theta_2/0]_s$ test specimens, being the same physical plate, had the same natural frequencies.

TABLE 2

EXPERIMENTAL NATURAL FREQUENCIES   (AVERAGE VALUES)

Test Specimen	1st bending freq (Hz)	2nd bending freq (Hz)	1st torsion freq (Hz)
$[0_2/90]_s$	11.1	69.0	42.2
$[\pm45/0]_s$	6.07	38.5	77.4
$[+45_2/0]_s$ $[-45_2/0]_s$	4.83	30.1	51.1
$[+30_2/0]_s$ $[-30_2/0]_s$	5.97	36.1	58.4

In going from the balanced $[\pm45/0]_s$ test specimen to the unbalanced $[+45_2/0]_s$ test specimen, the torsion frequency, which is largely dependent on the torsional flexibility of the specimen, decreased by 34%. Also, the first bending mode frequency decreased by 20%. These results

were consistent, at least in direction, with those of the static deflection tests.

The situation becomes slightly more confusing when the frequencies of the other test specimens are compared with their flexibility influence coefficients. The first and second bending mode frequency trends correlate well with the trends of the bending flexibility influence coefficients. However, the trends for the torsion frequencies and the torsion flexibility influence coefficients had poor correlation. This indicated that the bending torsion coupling must be primarily affecting the torsion frequency. As an aside, when stiffness influence coefficients were compared to natural frequencies in this manner, one was led to conclude that the coupling primarily affected the bending frequencies.

All the test specimens, except the $[0_2/90]_s$ specimen, exhibited first bending as the lowest frequency, followed by second bending, and finally first torsion. The $[0_2/90]_s$ test specimen started with first bending, followed by first torsion and finally second bending.

(c) Wind Tunnel Tests

The primary objective of the wind tunnel tests was to determine the zero initial angle of attack ($\alpha_0 = 0$) divergence and flutter velocities for each test specimen. Since the test velocities were low and the test specimens quite

flexible, the onset of flutter at zero α_0 tended to be gradual. For consistency, the flutter threshold was defined to be the velocity where the oscillation amplitude stabilized and the waveform became periodic. Determining the threshold for stall flutter was somewhat easier, because oscillation tended to begin abruptly when the stall angle of attack was reached.

The type of flutter (bending, torsion or bending-torsion) could not be determined completely from the amplitude of the bending and torsion strip chart channels. This was because, for a plate with bending - torsion coupling, the elastic axis was not located at the midchord, where the strain gauges were located. So a pure bending deflection excited both the bending and torsion strain gauges. The problem was overcome by defining bending flutter as oscillations with a frequency very close to one of the bending natural frequencies. Torsion flutter was said to occur when the frequency was close to the torsion natural frequency, and bending-torsion flutter occured at a frequency between the other two.

On test 9, with the $[-45_2/0]_s$ test specimen, a torsion strain gauge failed due to excessive deflection about half way through the test. The test was completed using the bending channel only. The malfunction was in a wire soldered to the terminal, which was repaired and caused no further problems. A bending strain ga e on the $[-30_2/0]_s$

test specimen failed at the end of Test 3, also due to excessive deflections. This gauge was not repairable, so Tests 14 and 15 were run with only one bending strain gauge. Temperature fluctuations during these two tests caused a zero drift on the bending channel. This zero drift made the data worthless for determining static deflections. However, the data were satisfactory for determining oscillation frequencies and amplitudes.

The flutter threshold velocity was plotted versus initial angle of attack in Fig. 8. The test specimens exhibited markedly different behavior. The $[0_2/90]$ test specimen, with no bending-torsion coupling, exhibited bending-torsion flutter with a frequency of approximately 30 Hz for angles of attack below two degrees and torsion flutter with a frequency of approximately 42 Hz for higher angles of attack. The test specimens with large positive bending-torsion coupling, $[+30_2/0]_3$ and $[+45_2/0]_s$, exhibited primarily bending-torsion flutter at 28 Hz and 24 Hz, respectively. The flutter threshold velocity did not drop significantly with increasing angle of attack, probably because the coupling caused a decrease in the tip angle of attack, preventing it from stalling. At an angle of attack of 18 degrees, the flutter threshold for the $[+30_2/0]_s$ test specimen dropped significantly and the flutter changed to torsion flutter at 55 Hz. The $[\pm45_2/0]_s$ test specimen, which was stiff in torsion and had
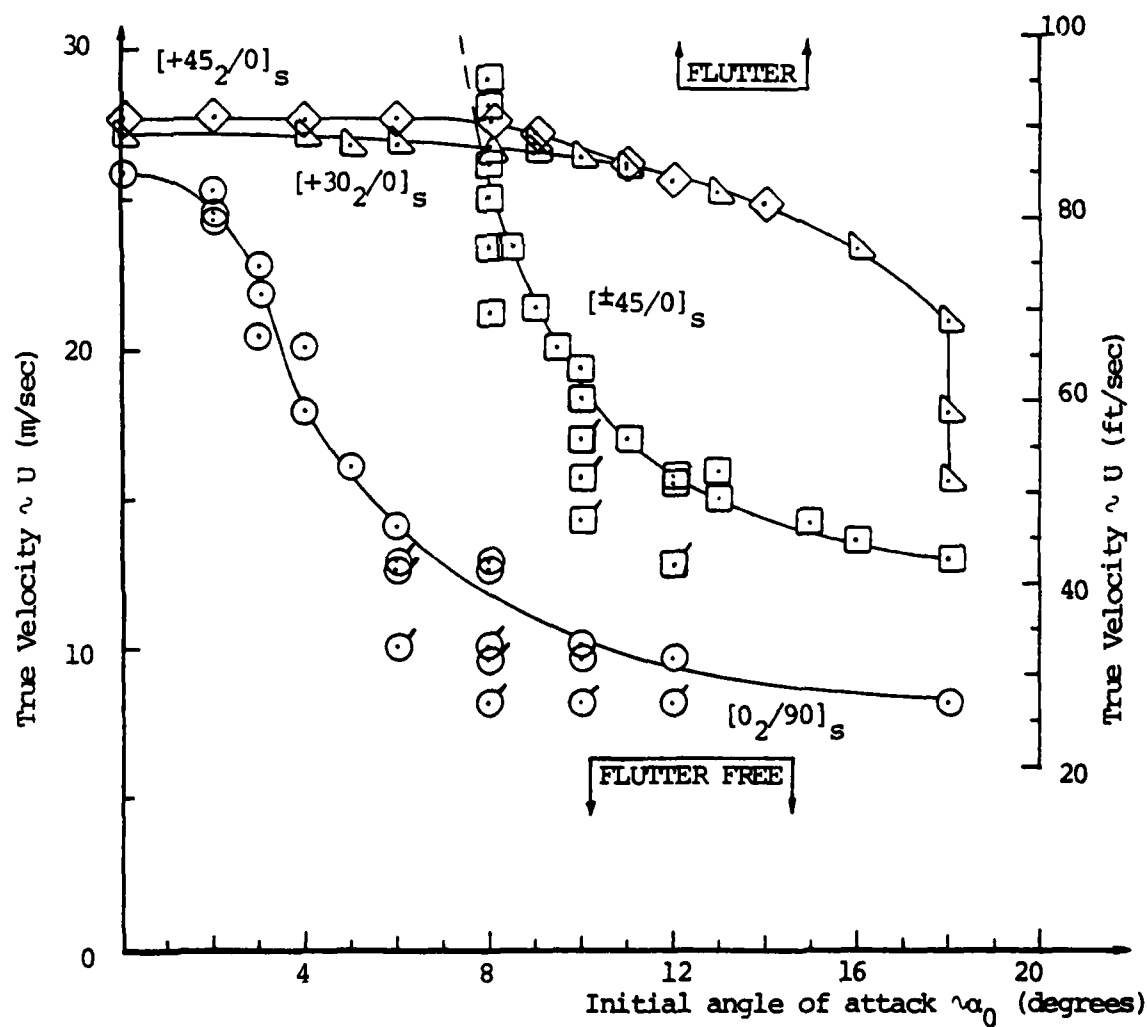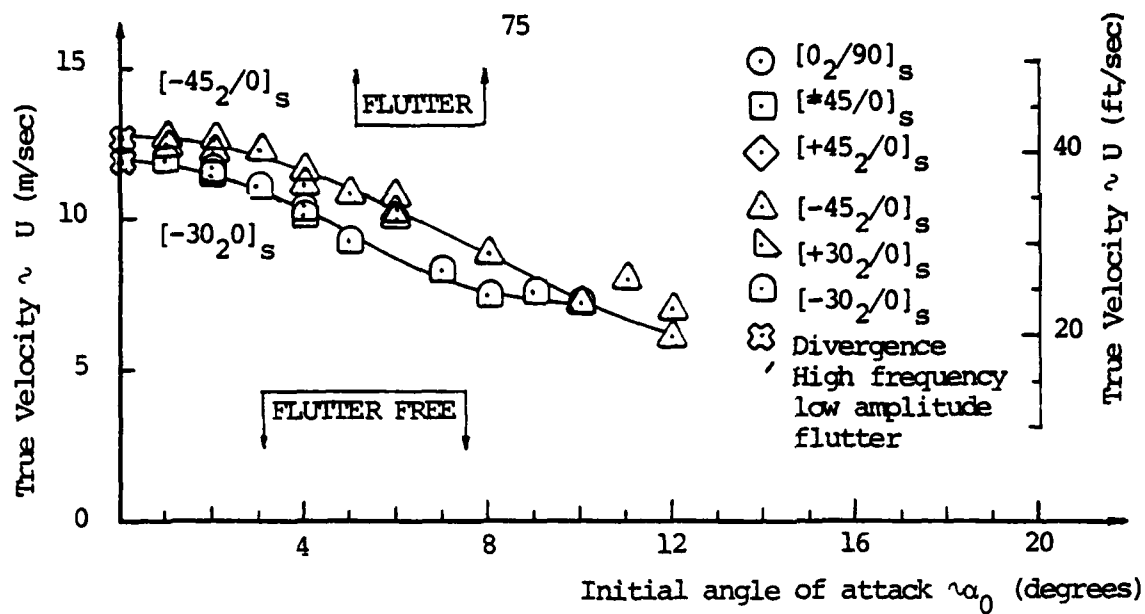
Figure 8. Flutter Boundary Velocities

only a small amount of positive bending-torsion coupling,
would not flutter at zero angle of attack within the 32 m/sec
maximum speed for the wind tunnel. However, at angles of
attack above eight degrees, it behaved similarly to the
$[0_2/90]_s$ test specimen. The flutter was primarily torsion
at 60 Hz. The test specimens with large negative bending-
torsion coupling, $[-30_2/0]_s$ and $[-45_2/0]_s$, exhibited divergence
at zero angle of attack. These two test specimens exhibited
primarily bending flutter with frequencies of 4.5 Hz and
4.0 Hz, respectively, at angles of attack greater than one
degree. This flutter was more of a Von Karman vortex shed-
ding buffet then a true stall flutter.

Several data points in Fig. 8 have been marked with a
(') to indicate a high frequency, low amplitude oscillation.
The $[0_2/90]_s$ test specimen exhibited bending oscillations
at 69 Hz and torsion oscillations at 145 Hz. The $[\pm45_2/0]_s$
test specimen exhibited torsion oscillations at 108 Hz.
These oscillations indicated that the second bending and
second torsion modes had been excited, which happened because
the plates were quite flexible. They do not represent the
phenomenon with which this study is concerned.

The effect of bending-torsion coupling on the zero
angle of attack flutter velocity could not be determined
directly from Fig. 8. This was because the test specimens
had varying amounts of torsional stiffness, which strongly

affect the flutter velocities. To cancel out the effect of torsional stiffness, the dimensionless reduced flutter velocity $(U_F/b\omega_\alpha)$ was plotted versus angle of attack in Fig. 9. In this parameter, b is the semichord and ω_α is the first torsion natural frequency, which was obtained experimentally.

The trends for each test specimen are similar to Fig. 8, as one would expect. However, in Fig. 9, the $[0_2/90]_s$ test specimen had the highest zero angle of attack reduced flutter velocity, followed by the $[+45_2/0]_s$ test specimen, and finally the $[+30_2/0]_s$ test specimen. Since the $[+30_2/0]_s$ test specimen had the largest positive bending-torsion coupling, the $[+45_2/0]_s$ test specimen had somewhat less, and the $[0_2/90]_s$ test specimen had none, one may conclude from this very limited sample size that zero angle of attack flutter reduced velocity was inversely proportional to positive bending-torsion coupling.

The $[-45_2/0]_s$ test specimen had a higher reduced divergence velocity $(U_D/b\omega_\alpha)$ than the $[-30_2/0]_s$ test specimen. So, using the same logic as before, one may conclude that divergence velocity was inversely proportional to increasingly negative bending-torsion coupling. Visual observations indicated that divergence was impossible for test specimens with substantial positive bending-torsion coupling.
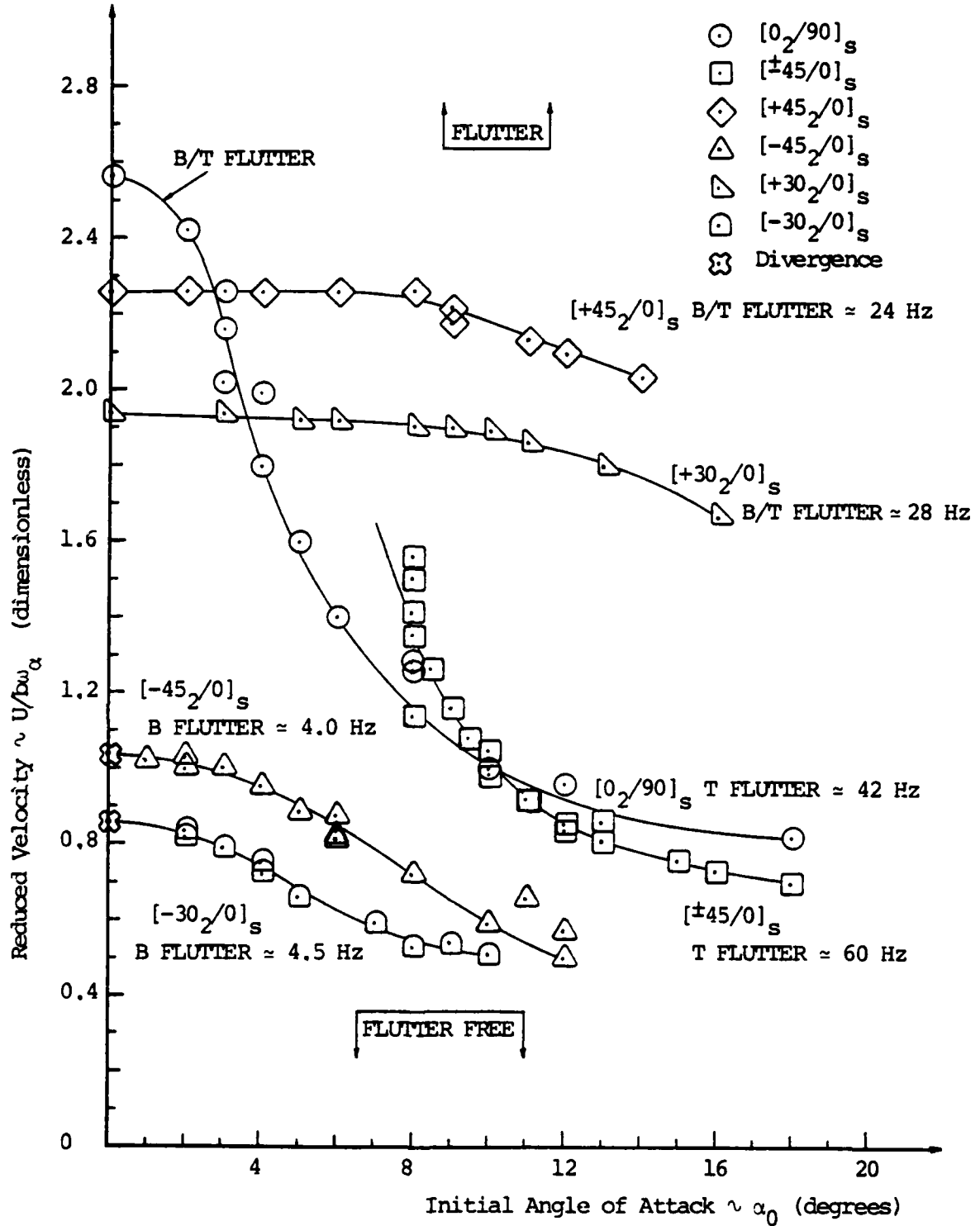
Figure 9.   Reduced Flutter Boundary Velocities

Static tip deflections, both α_{tip} and $w_{e_{tip}}$, for the $[+45_2/0]_s$, $[\pm45/0]_s$, and $[-45_2/0]_s$ were plotted versus velocity in Figs. 10, 11 and 12, respectively. The tip deflection data were obtained using the data reduction procedure in Appendix E. This data reduction procedure, which relates strain gauge readings to tip deflections through static calibrations, was only an approximation. Therefore, Figs. 10 - 12 must be examined for qualitative information only. The lines faired on the plots represent a "best fit" to the available data, which have been arbitrarily extrapolated to indicate some trends. The α_{tip} was the sum of the initial angle of attack (α_0) and the elastic twist (α_e).

Figure 10 indicates a linear relationship between lateral tip deflection and velocity. This seems odd, because the force on the wing is a function of the dynamic pressure (q), which is a function of the square of the velocity. One would expect this relationship to be parabolic. Two possible explanations are offered. First, the relationship was parabolic and the data were somewhat in error. Second, the bending-torsion coupling reduced the tip angle of attack to a low value as the test specimen was bent laterally. Unfortunately, the plot of the tip angles of attack doesn't support this second explanation. However, values for α_e obtained from the strip chart were extremely
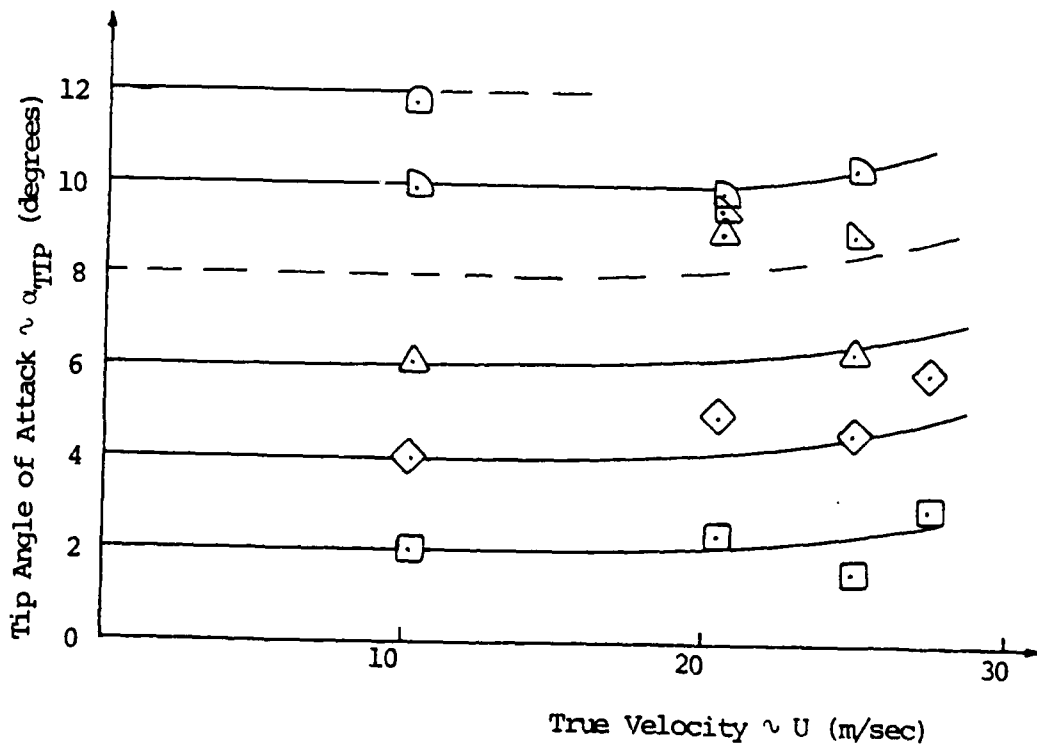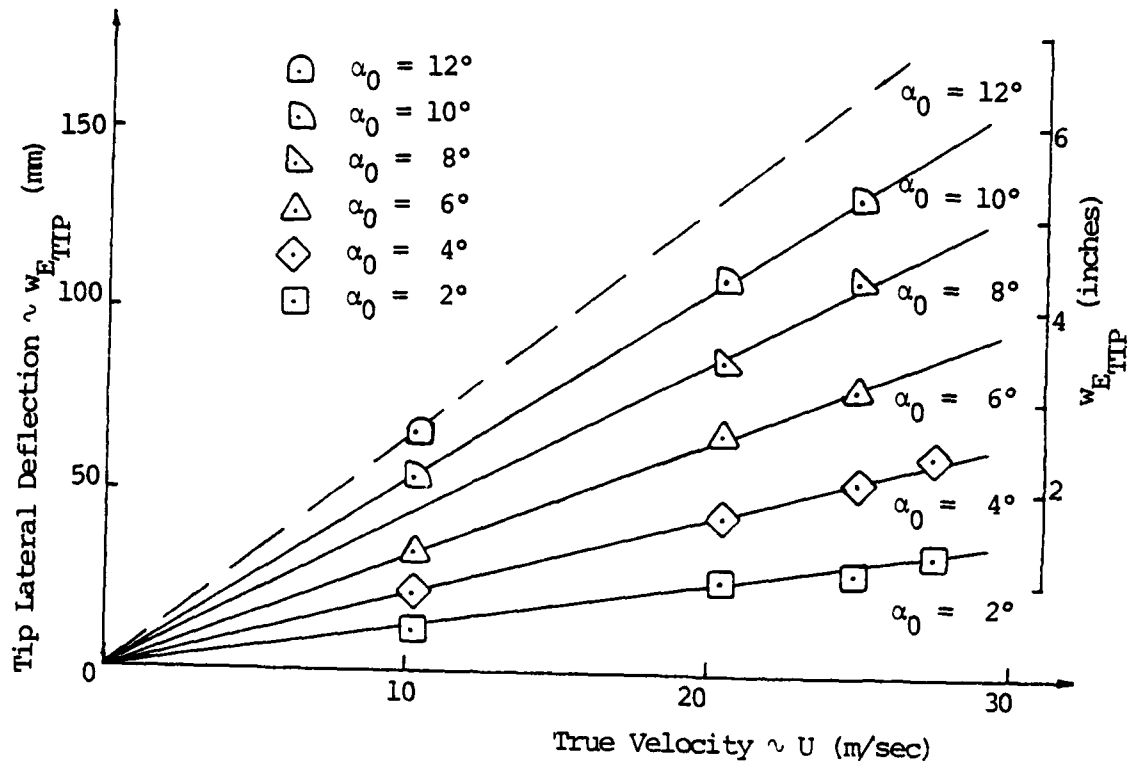
Figure 10. Experimental Static Aeroelastic Deflection, $[+45_2/0]_s$ Test Specimen
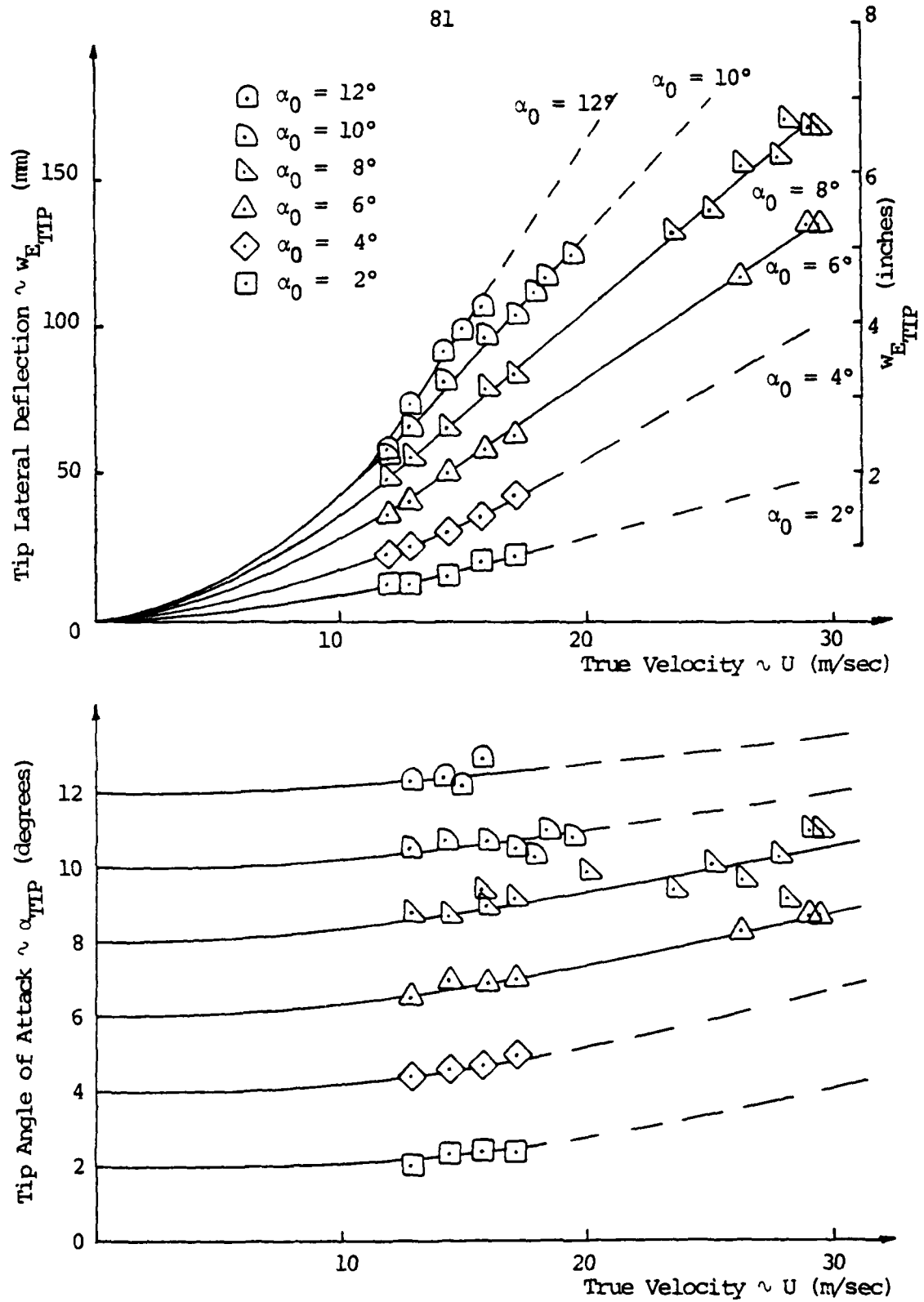
Figure 11. Experimental Static Aeroelastic Deflections, $[\pm 45/0]_s$ Test Specimen
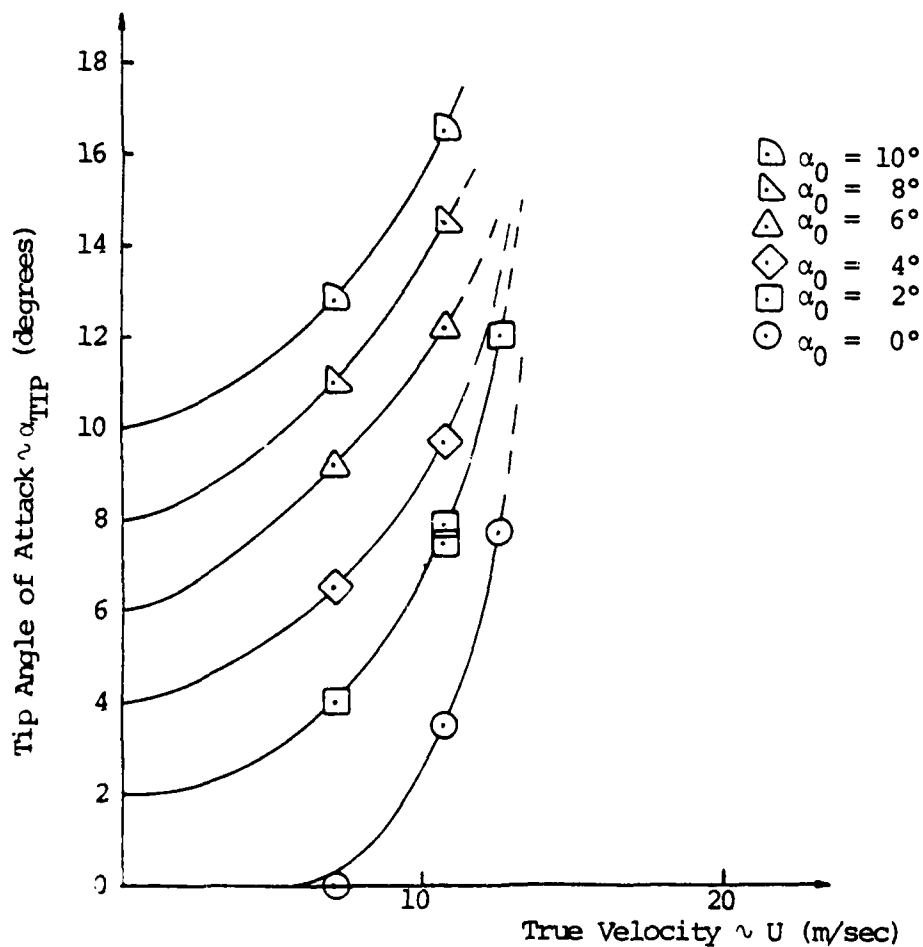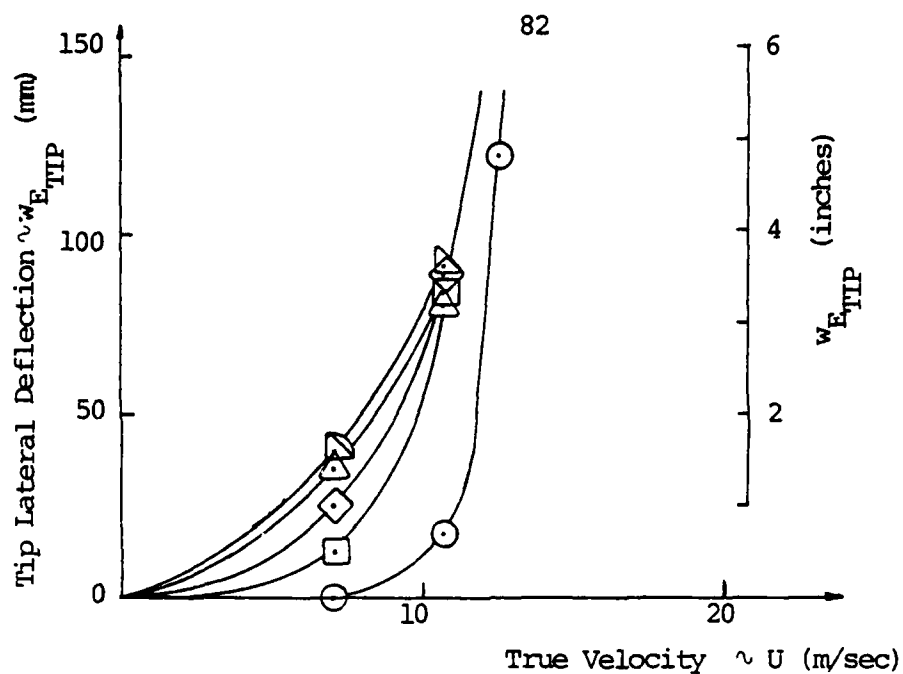
Figure 22. Experimental Static Aeroelastic Deflections, $[-45_2/0]_s$ Test Specimen

sensitive to slight errors in reading the strip chart. This was compounded by the fact that buffeting of the test specimens made it difficult to get an accurate strip chart reading.

Figure 11 indicates a more parabolic relationship between the lateral tip deflections and velocity. Also the tip angle of attack increases with increasing velocity as one would expect for a wing with low bending-torsion coupling. More data points were available for Fig. 11 and they have good continuity.

Figure 12 shows the expected divergent response tendencies of a wing with negative bending-torsion coupling.

The flutter amplitude was plotted versus velocity for the $[+45_2/0]_s$, $[\pm 45/0]_s$, and $[-45_2/0]_s$ test specimens in Figs. 13, 14, and 15, respectively. The flutter amplitude was unreduced, unamplified, peak to peak oscillation data directly from the strip chart. It has no significance other than to indicate where the flutter starts, for a given initial angle of attack, and to indicate how rapidly the magnitude increases. For both the $[+45_2/0]_s$ and $[-45_2/0]_s$ test specimens flutter beings quite close together for several angles of attack. While, for the $[\pm 45/0]_s$ test specimen the occurrence is more spread out.
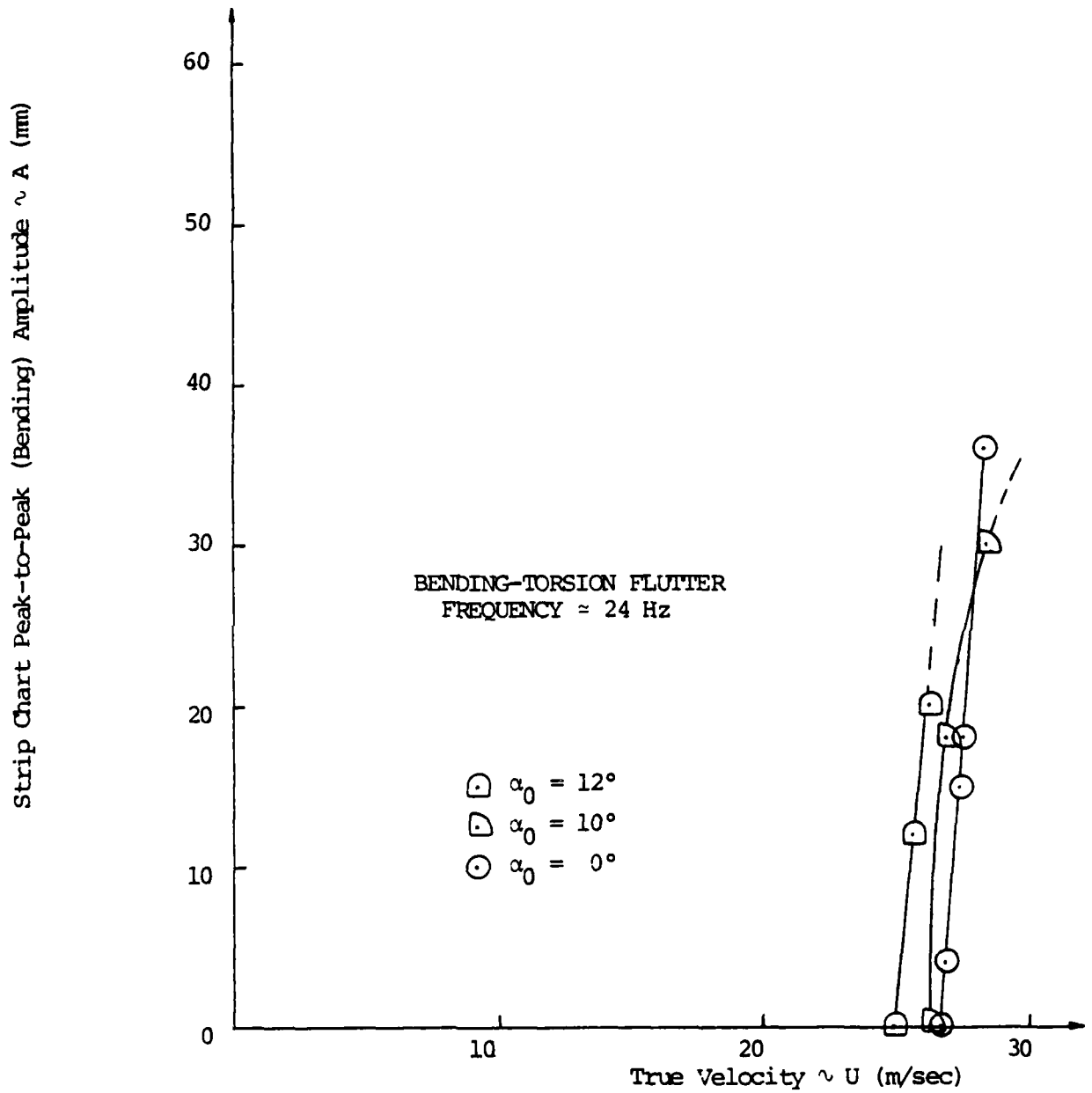
Figure 13. Flutter Amplitudes. $[+45_2/0]_s$ Test Specimen
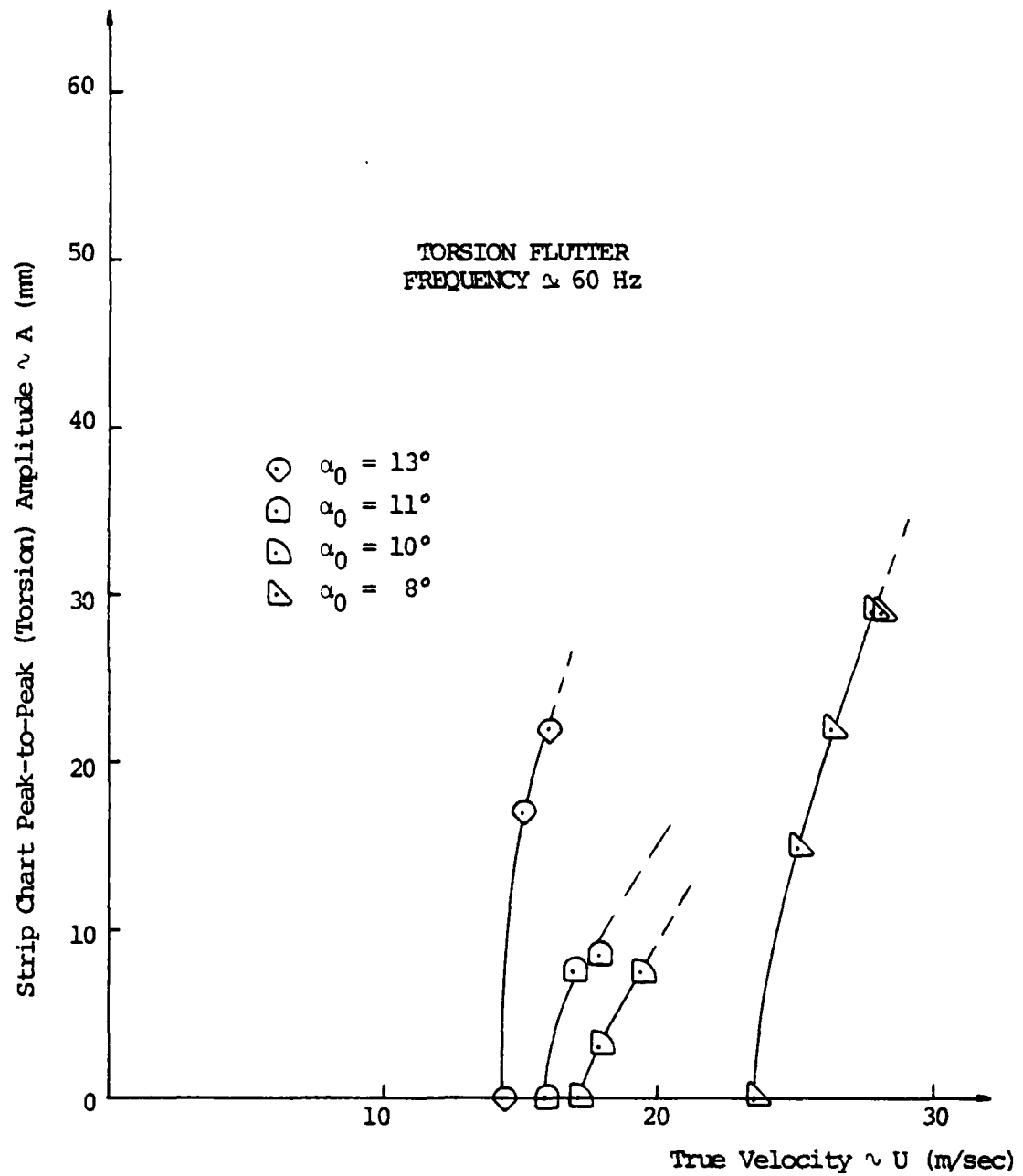
Figure 14. Flutter Amplitudes, $[\pm 45/0]_s$ Test Specimen
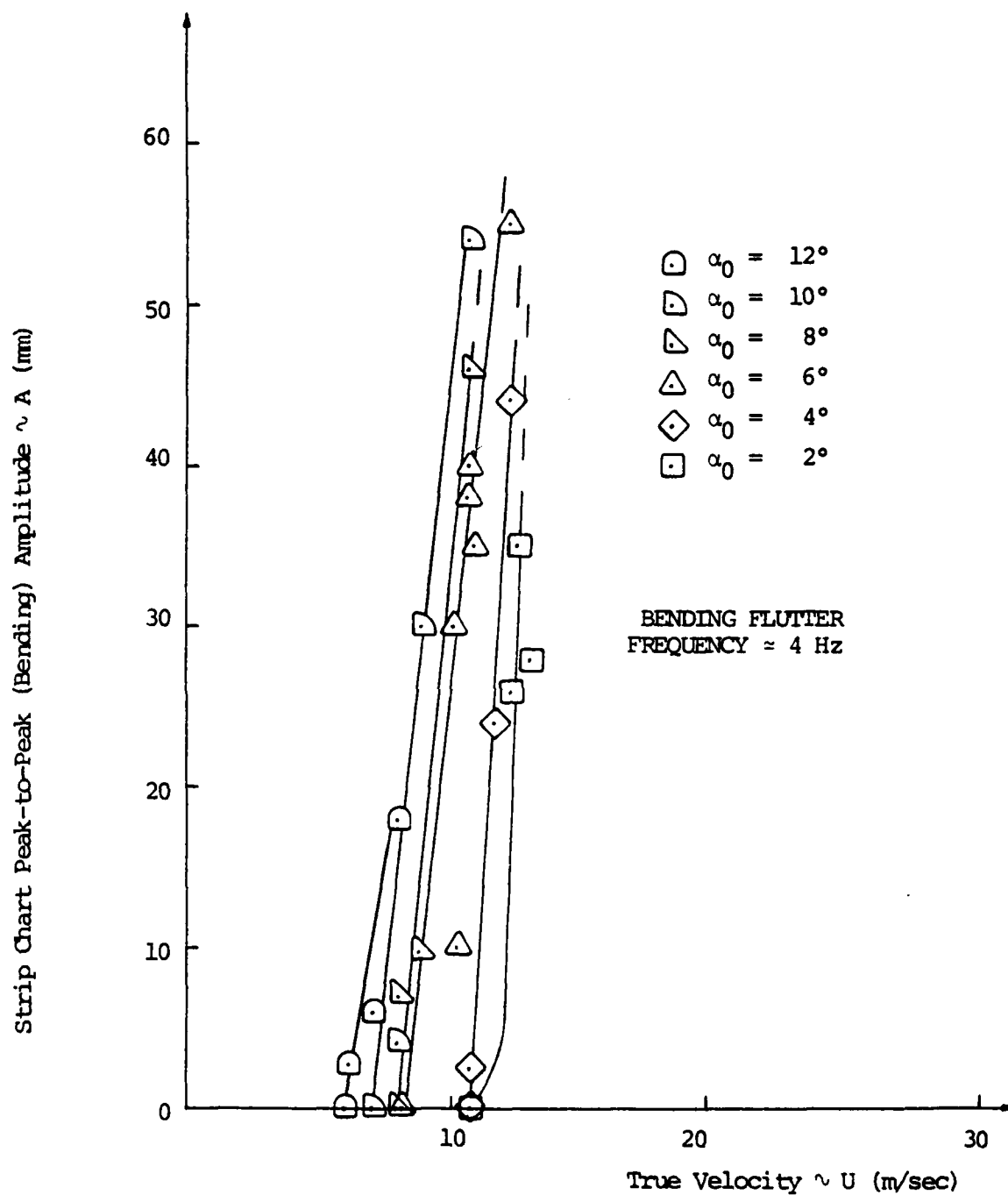
Figure 15. Flutter Amplitudes, $[-45_2/0]_s$ Test Specimen

CHAPTER IV

COMPARISON OF THEORETICAL AND EXPERIMENTAL RESULTS

Work done by Boyce[18], Crawley[19], and, in particular, Turner[10] showed that stiffness properties for graphite/epoxy laminates experimentally obtained from in-plane extensional loading were generally higher than material properties obtained from out-of-plane flexural loading. The standard TELAC values for E_L, E_T, G_{LT} and ν_{LT}, which appear in Appendix A, were obtained for Hercules AS/3501-6 G/E from in-plane loads. Turner, through a series of out-of-plane flexural static and dynamic tests, established an alternative set of material property values for AS/3501-6 G/E. These material property values also appear in Appendix A. Turner's values, while not statistically significant like the TELAC values, do constitute a basis for comparison. Therefore, in this chapter, experimental results will be compared to theoretical results using both TELAC and Turner material properties for graphite/epoxy. Additionally, discussion, in several instances, will be limited to qualitative "trends" due primarily to the approximate nature of the data being compared.

4.1 Static Deflection Tests

The theoretical and experimental flexibility influence

coefficients for each test specimen appear in Table 3. For
clarity, they have been arranged in 2 x 2 matrices. As
stated before, c_{11} is the bending flexibility, c_{22} is the
torsion flexibility, and c_{12}, c_{21} are the bending torsion
coupling flexibilities.

Values for c_{11} calculated from Turner material proper-
ties were within 10% of experimental values. The c_{11}'s
from TELAC material properties were lower than Turner
and experimental c_{11}'s, indicating that TELAC material pro-
perties resulted in a plate that was too stiff in pure
bending. The coupling flexibility influence coefficients
obtained from TELAC data were, however, in better agreement
with experimental data than those from Turner data.

The torsion influence coefficient for the $[\pm 45/0]_s$ test
specimen obtained from Turner data had reasonable agreement
with the experimental value. The torsion influence coef-
ficients obtained from both Turner and TELAC data had poor
agreement with experimental values for test specimens with
large bending-torsion coupling. With one notable exception,
all theoretical values for c_{22} were lower than experimental
values. The exception was the $[0_2/90]_s$ test specimen, where
theory predicted a substantially higher value for c_{22} than
was obtained from the experiments. For all test specimens,
except $[0_2/90]_s$, torsion influence coefficients obtained
using Turner data had better agreement with experimental

89

TABLE 3
FLEXIBILITY INFLUENCE COEFFICIENTS

Test Specimen	Theoretical		Experimental
	TELAC Material Properties	Turner Material Properties	
$[O_2/90]_s$	$\underline{\underline{C}} = \begin{bmatrix} 0.139 & 0 \\ 0 & 3.38 \end{bmatrix}$ $\kappa = 0$	$\underline{\underline{C}} = \begin{bmatrix} 0.184 & 0 \\ 0 & 3.69 \end{bmatrix}$ $\kappa = 0$	$\underline{\underline{C}} = \begin{bmatrix} 0.18 & -0.03 \\ -0.02 & 2.3 \end{bmatrix}$ $\kappa = 0.0014$
$[\mp45/0]_s$	$\underline{\underline{C}} = \begin{bmatrix} 0.427 & -0.185 \\ -0.185 & 0.737 \end{bmatrix}$ $\kappa = 0.109$	$\underline{\underline{C}} = \begin{bmatrix} 0.548 & -0.237 \\ -0.237 & 0.972 \end{bmatrix}$ $\kappa = 0.106$	$\underline{\underline{C}} = \begin{bmatrix} 0.60 & -0.16 \\ -0.13 & 1.06 \end{bmatrix}$ $\kappa = 0.033$
$[+45_2/0]_s$	$\underline{\underline{C}} = \begin{bmatrix} 0.788 & -0.731 \\ -0.732 & 1.34 \end{bmatrix}$ $\kappa = 0.505$	$\underline{\underline{C}} = \begin{bmatrix} 0.972 & -0.912 \\ -0.912 & 1.72 \end{bmatrix}$ $\kappa = 0.496$	$\underline{\underline{C}} = \begin{bmatrix} 0.98 & -0.76 \\ -0.75 & 2.7 \end{bmatrix}$ $\kappa = 0.215$
$[+30_2/0]_s$	$\underline{\underline{C}} = \begin{bmatrix} 0.508 & -0.755 \\ -0.755 & 1.944 \end{bmatrix}$ $\kappa = 0.578$	$\underline{\underline{C}} = \begin{bmatrix} 0.617 & -0.890 \\ -0.890 & 2.36 \end{bmatrix}$ $\kappa = 0.545$	$\underline{\underline{C}} = \begin{bmatrix} 0.64 & -0.80 \\ -0.82 & 3.0 \end{bmatrix}$ $\kappa = 0.342$

values than did torsion influence coefficients obtained using TELAC data.

There were several possible reasons for differences between theoretical and experimental torsion influence coefficients. First, the two term deflection equation may not adequately represent the actual deflection of the structure. Additional terms would allow more degrees of freedom. Second, the assumption that the plate was chordwise rigid when undergoing torsional deflections may not be true, especially for test specimens with large bending-torsion coupling. Third, the theory used to obtain the flexural moduli (D_{ij}) for the plates, as presented in Chapter II, assumed small deflections and, consequently, neglected transverse shear. If transverse shear was present, the plate would become more flexible in torsion. Further, if transverse shear increased with increasing bending-torsion coupling, then for test specimens with large bending-torsion coupling, one would expect the experimental torsion flexibility influence coefficients to be much larger than the theoretical influence coefficients. This was the case in this study.

The final significant trend was that the coupling factor (κ) for the theoretical flexibility influence coefficients was substantially higher than the experimental coupling factor for all test specimens except $[0_2/90]_s$.

Both the theoretical and experimental coupling factors were essentially zero for the $[0_2/90]_s$ test specimen.

4.2 Free Vibration Tests

A summary of the theoretical and experimental natural frequencies for the first three natural vibration modes of each test specimen appears in Table 4. Also included in Table 4 are the theoretical uncoupled natural frequencies calculated using the following equations.[19]

$$\text{(first bending)} \quad \omega_{1B} = 3.52\sqrt{\frac{D_{11}}{m\ell^4}} \qquad (4\text{-}1a)$$

$$\text{(second bending)} \quad \omega_{2B} = 22.0\sqrt{\frac{D_{11}}{m\ell^4}} \qquad (4\text{-}1b)$$

$$\text{(first torsion)} \quad \omega_{1T} = 1.57\sqrt{\frac{48D_{66}}{m\ell^2 c^2}} \qquad (4\text{-}1c)$$

where D_{11} is the bending flexural modulus, D_{66} is the torsion flexural modulus, m is the mass per area, ℓ is the length, c is the chord, and ω is the frequency in rad/sec.

The theoretical first bending natural frequencies, calculated using Turner material properties, were all within 5% of the experimental values, which was good agreement. The first bending frequencies calculated from TELAC material properties had poorer agreement with experimental values.

TABLE 4

NATURAL FREQUENCIES

Test Specimen	Vibration Mode	Uncoupled		Theoretical (Hz)				Experimental (Hz)
				2 Term Deflection Eq.		3 Term Deflection Eq.		
		TELAC	Turner	TELAC	Turner	TELAC	Turner	
[O$_2$/90]$_s$	1B	12.7	11.1	12.7	11.1	12.7	11.1	11.1
	2B	79.7	69.2			79.8	69.3	69
	1T	34.3	33.2	34.4	33.2	34.4	33.2	42
[∓45/0]$_s$	1B	7.69	6.78	7.25	6.40	7.25	6.40	6.1
	2B	48.1	42.3			47.9	42.2	38
	1T	80.3	69.8	80.4	69.8	80.6	70.0	77
[+45$_2$/0]$_s$	1B	7.69	6.78	5.35	4.79	5.23	4.69	4.8
	2B	48.1	42.3			46.8	41.3	30
	1T	80.3	69.8	80.5	70.0	81.4	70.7	51
[+30$_2$/0]$_s$	1B	10.2	8.95	6.57	5.97	6.35	5.80	6.0
	2B	64.1	56.0			59.7	52.4	36
	1T	71.6	62.7	72.1	63.1	75.9	66.2	58

In all cases, the TELAC first bending frequencies were higher than experimental frequencies. The theoretical uncoupled first bending frequencies, as one would expect, showed good correlation with experimental frequencies for test specimens with little bending-torsion coupling, and poor correlation for test specimens with large bending-torsion coupling.

The theoretical values for the second bending frequencies from Turner material properties showed reasonable agreement with the experimental values for test specimens with low coupling, and poor agreement for test specimens with large coupling. Second bending frequencies calculated from TELAC material properties were not as good as the frequencies from Turner data. The theoretical uncoupled values for the second bending frequency had generally poorer agreement with the experimental values than the coupled solutions did.

The theoretical first torsion natural frequencies had generally poor agreement with experimental values. Errors for first torsion natural frequencies calculated using Turner material properties were lowest for the $[\pm 45/0]_s$ test specimen and highest for the $[+45_2/0]_s$ test specimen. More importantly, one observes that the theoretical torsion frequency values for the $[\pm 45/0]_s$ and $[+45_2/0]_s$ test specimens were essentially the same, while the experimental torsion

frequency for the $[+45_2/0]_s$ test specimens was substantially
lower than the experimental torsion frequency for the $[\pm45/0]_s$
test specimen. The higher torsion frequency for the $[\pm45/0]_s$
test specimen indicated that it was much stiffer in torsion
than the $[+45_2/0]_s$ test specimen. As before, this was pos-
sibly due to neglecting transverse shear in the problem
derivation. Also, the fact that only the first three vib-
ration mode shapes were used to formulate the assumed deflec-
tion equation could affect the solutions somewhat. Finally,
as before, the assumption that the plate was chordwise rigid
during torsion vibrations could also affect the solution.

The theoretical natural frequencies should possibly be
checked by a more extensive Rayleigh-Ritz formulation and
a finite element analysis.

4.3 Divergence Velocities

Theoretical and experimental divergence velocities for
each test specimen appear in Table 5. Velocities were ob-
tained for plates using both TELAC and Turner material prop-
erties, and for both a two dimensional lift curve slope
$(2c_\ell/2\alpha)$ and one empirically corrected for finite span using
the correction expression in Chapter II. Of the six speci-
mens tested, only three would possibly exhibit any divergence
at zero initial angle of attack. These three test specimens
were $[0_2/90]_s$, $[-45_2/0]_s$, and $[-30_2/0]_s$. Of these three,

TABLE 5

DIVERGENCE VELOCITIES

| Test Specimen | Theoretical | | | | Experimental |
| | Infinite Span | | Finite Span | | |
	TELAC	Turner	TELAC	Turner	
$[O_2/90]_s$	20.1 m/sec (65.8 ft/sec)	19.3 m/sec (63.2 ft/sec)	22.4 m/sec (73.6 ft/sec)	21.5 m/sec (70.6 ft/sec)	>27 m/sec (>90 ft/sec)
$[\pm 45/0]_s$	Infinite - would not diverge				>32 (>105)
$[+45_2/0]_s$	Infinite - would not diverge				>28 (>92)
$[-45_2/0]_s$	10.5 (34.3)	9.33 (30.6)	11.7 (38.3)	10.4 (34.2)	12.5 (41.0)
$[+30_2/0]_s$	Infinite - would not diverge				>28 (>92)
$[-30_2/0]_s$	10.1 (33.0)	9.24 (30.3)	11.2 (36.9)	10.3 (33.9)	11.7 (38.5)

Finite span $\partial C_\ell / \partial \alpha = 2\pi \, [AR/(AR + 2)]$

the $[0_2/90]_s$ test specimen exhibited flutter prior to divergence, so no experimental divergence characteristics were obtained. However, a theoretical divergence velocity was still calculated for that specimen.

Theoretical divergence velocities were lower than experimental velocities in all cases. The finite span divergence for the $[-45_2/0]_s$ and $[-30_2/0]_s$ test specimens, calculated using Turner material properties, were lower than the divergence velocities calculated using TELAC material properties. An experimental divergence velocity was not obtained for the $[0_2/90]_s$ test specimen. However, the wind tunnel was taken up to 27 m/sec (90 ft/sec) with this test specimen and divergence did not occur. This contrasts to a theoretical finite span divergence velocity, calculated with Turner material properties, of 22 m/sec (71 ft/sec). This indicated that the theory would not adequately model the $[0_2/90]_s$ test specimen.

The fact that the theory predicted a lower divergence velocity than found from experiments would suggest that the actual plates were stiffer than the theoretical plates. This observation is in sharp contrast to the observations in Sections 4.1 and 4.2, where the theoretical plates appeared stiffer. The observation would tend to rebut the explanations given in those sections. Since divergence is a function of aerodynamic force on the plate, as well as plate

stiffness, the aerodynamic strip theory needed to calculate the loads on the plate may have been a source of error. Further, the finite span correction may have resulted in the theoretical air loads being greater than the actual air loads. Reference 13 suggests that an alternate empirical correction for finite span effects may provide better correlation between theoretical and experimental results for divergence problems. That empirical correction is

$$\frac{\partial C_\ell}{\partial \alpha} = a_0 [\frac{AR}{AR + 4}] \qquad (4-2)$$

Using this finite span correction, theoretical divergence velocities were raised slightly. A final source of error may have been the criteria used during the wind tunnel tests to determine the divergence velocity. This, however, is an improbable source of error.

4.4 Static Aeroelastic Tip Deflections

The theoretical tip lateral deflections ($w_{E_{TIP}}$) and tip angles of attack (α_{TIP}) were calculated using Turner material properties, the empirical finite span correction, and the solution technique in Chapter II. The tip deflections were plotted versus velocity for the $[+45_2/0]_s$, $[\pm45/0]_s$, and $[-45_2/0]_s$ test specimens in Figs. 16, 17, and 18, respectively. To allow a comparison with experimental
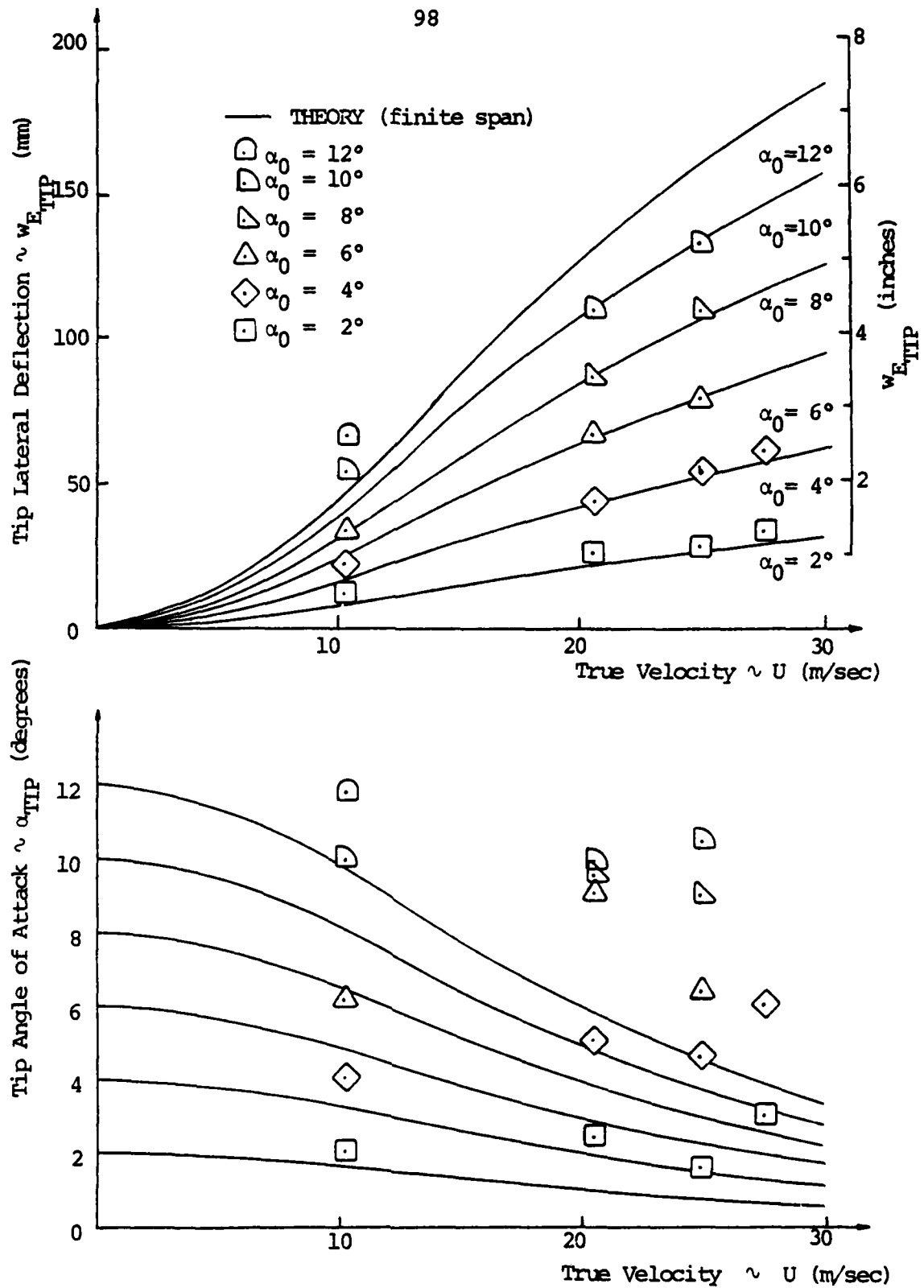
Figure 16. Static Aeroelastic Deflections, $[+45_2/0]_s$ Test Specimen
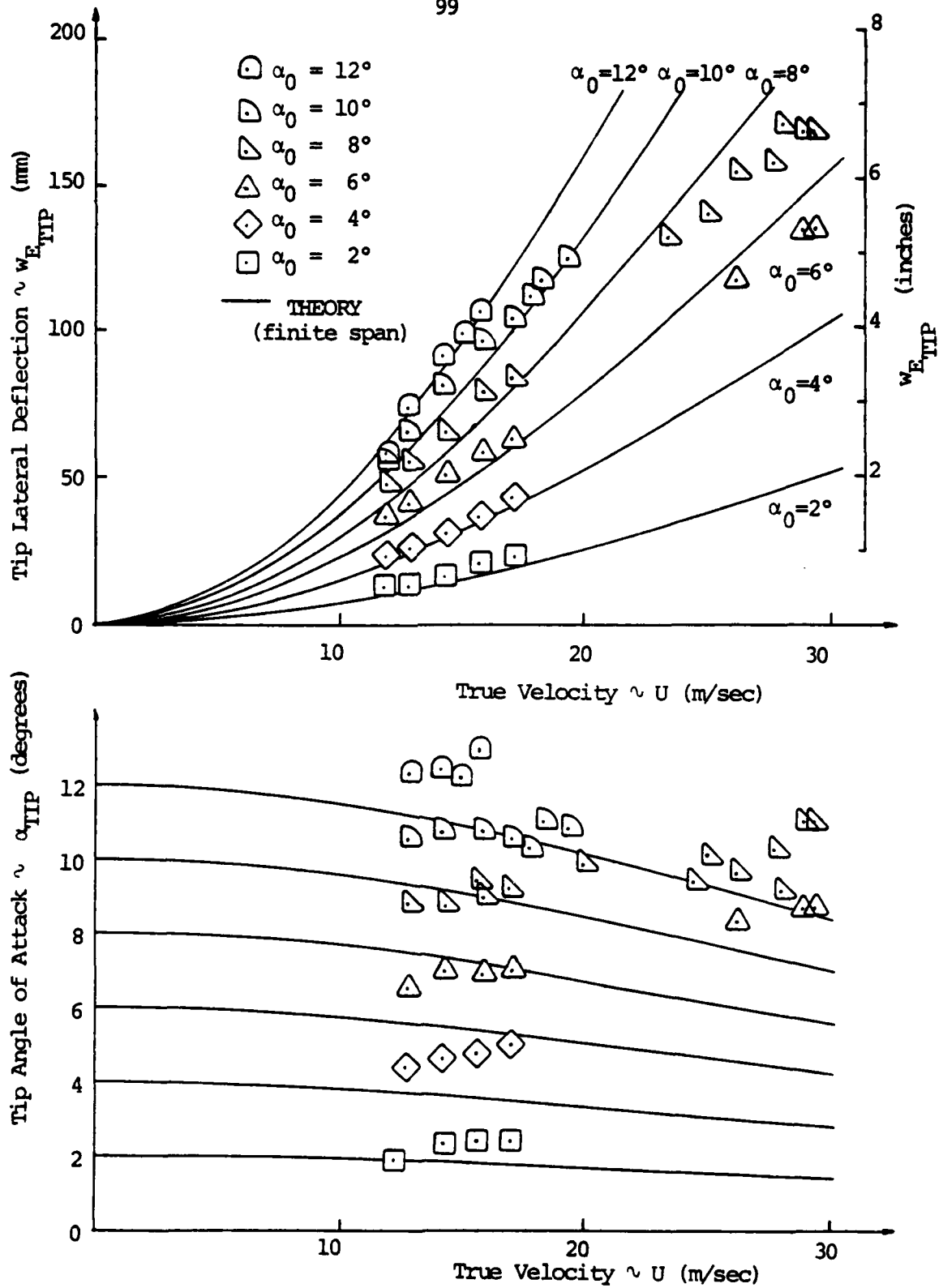
Figure 17. Static Aeroelastic Deflections, $[\pm 45/0]_s$ Test Specimen
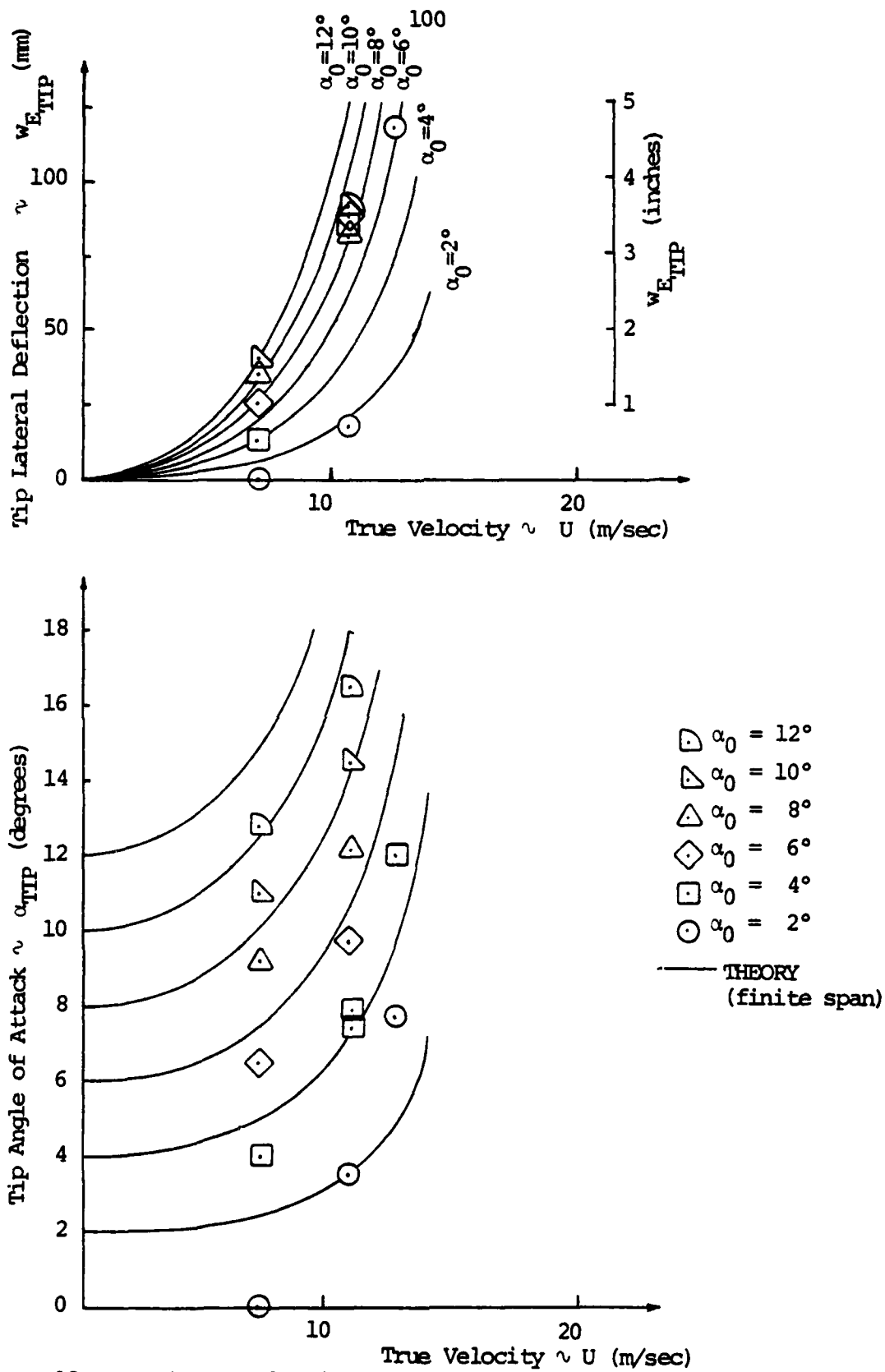
Figure 18. Static Aeroelastic Deflections, $[-45_2/0]_s$ Test Specimen

results, the approximate experimental tip deflections, discussed in Chapter III, were included in these figures. The lines represent the theory and the plotting symbols are the experimental values. Since data from both theory and experiment were approximate, a valid comparison must be limited to trends only.

In Fig. 16, the lateral deflection trends for the $[+45_2/0]_s$ test specimen show reasonable agreement between theory and experiment, especially at higher velocities. The trends for the theoretical and experimental tip angle of attack, however, did not agree. The experimental values indicated a very slight increase in tip angle of attack as velocity was increased. Theory, on the other hand, showed a substantial decrease in tip angle of attack as velocity was increased. The implications of the theoretical results were that the torsional moment resulting from bending-torsion coupling more than overcame the aerodynamic moment. A possible reason was that the theoretical coupling factor (κ), discussed in Section 4.1, was much larger than the experimental κ. Of course, there was also the problem with reading the strip chart, as discussed in Chapter III.

The agreement between theoretical and experimental lateral tip deflections for the $[\pm45/0]_s$ test specimen in Fig. 17 was not quite as good as for the $[+45_2/0]_s$ test specimen, but was still reasonable. Again, the trends for

the tip angles of attack did not correlate between theory
and experiment. The theoretical tip angles of attack did
not decrease as much for the $[\pm45/0]_s$ test specimen as they
did for the $[+45_2/0]_s$ test specimen, but the experimental
tip angle of attack values increased more for the $[\pm45/0]_s$
test specimen. In view of the fact that the $[\pm45/0]_s$ test
specimen possessed slight positive bending-torsion coupling,
one would anticipate this type of behavior. The reasons
for the lack of correlation between experiment and theory
then would be the same as for the $[+45_2/0]_s$ test specimen.

Divergent tendencies of both the tip lateral deflec-
tions and angles of attack for the $[-45_2/0]_s$ test specimen
are apparent in Fig. 18. The trends were similar for both
the theoretical and experimental results, although the ex-
perimental data did not correlate well with theory for indi-
vidual angles of attack. Finally, the experimental tip angle
of attack data appeared to diverge faster than the theore-
tical data.

4.5 Flutter Velocities

The theoretical and experimental flutter velocities at
zero angle of attack for each test specimen appear in Table
6. Additionally, the nondimensional reduced flutter velo-
cities for each test specimen are presented. Since the

TABLE 6

a. FLUTTER VELOCITIES

Test Specimen	Theoretical (U-g Analysis) TELAC	Turner	Experimental
$[0_2/90]_s$	18.0 m/sec (59.0 ft/sec]	17.4 m/sec (57.0 ft/sec)	25.9 m/sec (85.0 ft/sec)
$[\pm 45/0]_s$	42.1 (138)	36.6 (120)	32.0 (>105)
$[+45_2/0]_s$	40.2 (132)	35.1 (115)	27.7 (91.0)
$[-45_2/0]_s$	50.3 (165)	43.6 (143)	diverged first
$[+30_2/0]_s$	34.7 (114)	30.5 (100)	27.1 (89.0)
$[-30_3/0]_s$	50.0 (164)	42.3 (142)	diverged first

b. REDUCED FLUTTER VELOCITIES

Test Specimen	Theoretical TELAC	Turner	Experimental
$[0_2/90]_s$	2.21	2.21	2.56
$[\pm 45/0]_s$	2.21	2.21	>1.6
$[+45_2/0]_s$	2.11	2.11	2.24
$[-45_2/0]_s$	2.64	2.63	diverged first (1.01)
$[+30_2/0]_s$	2.04	2.04	1.94
$[-30_2/0]_s$	2.93	2.90	diverged first (.839)

$[-45_2/0]_s$ and $[-30_2/0]_s$ test specimens diverged prior to fluttering, no experimental flutter velocities were obtained for them. However, theoretical flutter velocities were calculated for these two test specimens. Also, the $[\pm45/0]_s$ test specimen did not flutter within the speed range of the wind tunnel.

The correlation between theoretical and experimental flutter velocities was generally poor. The flutter velocity for the $[0_2/90]_s$ test specimen, calculated using Turner material properties, was much lower than the experimental flutter velocity. On the other hand, the theoretical flutter velocities for the $[+45_2/0]_s$ and $[+30_2/0]_s$ test specimens, calculated using Turner material properties, were much higher than the experimental flutter velocities. The flutter velocities calculated using TELAC material properties had generally worse correlation.

The errors in the flutter calculations appeared to be directly related to the inability of the theory to accurately determine the torsion vibration frequencies. Therefore, one would expect a somewhat better correlation between theoretical and experimental reduced flutter velocities $(U_F/b\omega_\alpha)$, since the contribution of the torsion vibration frequency had been eliminated. In fact, that was exactly what happened. The $[0_2/90]_s$ test specimen's error was reduced significantly, and the errors associated with the $[+45_2/0]_s$

and $[+30_2/0]_s$ test specimens were less than 10%. The reader should note that the ω_α used for the theoretical calculations was obtained from the U-g analsyis for a very large reduced frequency (k) value.

Since the trends were reasonably well predicted by the theory, some conclusions on how bending-torsion coupling affects flutter velocity were drawn, based on theoretical results. The first conclusion was that increasingly positive bending-torsion coupling reduced the flutter velocity. The second conclusion was that increasingly negative bending-torsion coupling raised the flutter velocity. This was an unrealistic situation, however, because the test specimens with negative coupling diverged long before they reached the flutter velocity.

CHAPTER V

CONCLUSIONS AND RECOMMENDATIONS

5.1 Conclusions

The present study has sought to investigate the flutter and divergence behavior of graphite/epoxy plates with various amounts of bending-torsion stiffness coupling. As a consequence, the static deflection and vibration behavior has also been examined.

There was reasonable agreement between theory and experiments for the bending stiffness and first bending mode natural frequencies. Also, for test specimens with low bending-torsion coupling, there was reasonable agreement for the torsional stiffness and first torsion mode natural frequencies. There was, however, poor agreement between theory and experiments for torsion stiffness and frequencies of test specimens with large bending-torsion coupling. The poor agreement was probably due to an inadequate number of modes in the assumed deflection equation. Other possible sources of error were the assumption that the plate was chordwise rigid and the neglecting of the transverse shear effect.

In this study, only the plates with negative bending-torsion coupling $(-D_{16})$ exhibited divergence within the speed range of the wind tunnel. For these test specimens,

the theory had reasonable agreement with the experiments.
The errors in the theory were possibly due to the approximate aerodynamic strip theory. For test specimens with
positive bending-torsion coupling, the theory predicted that
divergence would not occur. Experimentally, they did not
exhibit a divergence tendency within the speed range of the
wind tunnel. Based on the theory and the limited set of
experiments, the following observations can be made. The
zero angle of attack divergence velocity, for the plates in
this study, became infinite for positive bending-torsion
coupling above a certain critical value. This divergence
velocity decreased as the bending-torsion coupling decreased
from the critical value to zero, and continued to decrease
as the bending-torsion coupling became increasingly negative.

The theory and experiments had poor agreement for zero
angle of attack flutter velocities. However, the agreement
between theory and experiments for reduced flutter velocities $(U/b\omega_{\alpha})$ was good. This indicated that the inaccuracies in the theory were in the prediction of the torsion
vibration frequency. The test specimens with negative
bending-torsion coupling diverged prior to reaching their
flutter velocities, but a theoretical flutter velocity was
still calculated for them. As before, based on the theory
and the limited set of experiments, the following observations can be made.

The zero angle of attack flutter velocity for the plate in this study was low for positive bending-torsion coupling. The flutter velocity increased as the positive bending-torsion coupling decreased to zero, and continued to increase as the bending-torsion coupling became increasingly negative. This latter situation, for negative bending-torsion coupling, becomes academic if divergence occurs prior to flutter.

The test specimens exhibited markedly different flutter behavior as angle of attack was increased. The test specimens with low bending-torsion coupling exhibited classical bending-torsion flutter at zero angle of attack, but it changed to pure torsion flutter as the angle of attack was increased. Also, the flutter boundary velocity decreased rapidly with increasing angle of attack, stabilizing around $\alpha = 12°$. This trend is similar to the results Rainey[8] obtained for metal plates and is classical stall flutter. The test specimens with large positive bending-torsion coupling exhibited bending-torsion flutter throughout most of the angle of attack range. Additionally, the flutter boundary velocities did not decrease with increasing angle of attack below $\alpha = 12°$. This behavior was probably due to the fact that the tip of the plate tended to have a lower angle of attack than the root, so it did not stall. The test specimens

with large negative bending-torsion coupling diverged at
zero angle of attack and exhibited a low frequency bending
flutter for angles of attack greater than zero. The flutter
boundary velocities here were significantly below the velo-
cities for the other test specimens for angles of attack
less than 12°. These bending flutter velocities decreased
moderately with increasing angle of attack.

5.2 Recommendations

The theory should be further developed to give better
results for the torsion vibration frequencies and flutter
velocities. Improvement could probably be most easily faci-
litated by going to a finite element analysis which allows
more degrees of freedom and accounts for transverse shear.
If a Rayleigh-Ritz formulation is used, more terms should
be included in the deflection equation. For divergence
velocity calculations, a better aerodynamic theory, such
as lifting line theory, should be used. Also, the stall
characteristics of the plate should be explored further.

The effect of bending-torsion coupling as a passive
gust alleviation technique might hold some promise. Further,
bending-torsion coupling might be useful for increasing the
aileron reversal speed for a swept wing. Finally, the effect
of bending-torsion coupling on an oblique wing, particularly
with the roll degree of freedom, might prove interesting.

APPENDIX A

MATERIAL PROPERTIES

TABLE A-1

ORTHOTROPIC ENGINEERING CONSTANTS

Hercules AS/3501-6 Graphite/Epoxy

Property	TELAC Values (in-plane loads)	Turner Values (out-of-plane loads)
E_L	130×10^9 Pa	98×10^9 Pa
E_T	10.5×10^9	7.9×10^9
ν_{LT}	0.28	0.28
G_{LT}	6.00×10^9	5.6×10^9
Ply thickness	1.34×10^{-6} m	
Density	1.52 kg/m^3	

TABLE A-2

LAMINATE FLEXURAL MODULI

Laminate	Modulus	TELAC Material Properties		Turner Material Properties	
	D_{11}	5.474 Nm	4.038 lb·ft	4.126 Nm	3.043 lb·ft
$[0_2/90]_s$	D_{16}	0	0	0	0
	D_{66}	0.2600	0.1918	0.2425	0.1789
	D_{11}	1.996	1.472	1.550	1.143
$[\pm45/0]_s$	D_{16}	0.5789	0.427	0.4364	0.3219
	D_{66}	1.422	1.049	1.074	0.7920
	D_{11}	1.996	1.472	1.550	1.143
$[+45_2/0]_s$	D_{16}	1.254	0.925	0.9456	0.6975
	D_{66}	1.422	1.049	1.074	0.7920
	D_{11}	3.541	2.612	2.703	1.994
$[+30_2/0]_s$	D_{16}	1.589	1.172	1.179	0.8695
	D_{66}	1.132	0.8350	0.8662	0.6389

APPENDIX B

THEORETICAL ANALYSIS

B.1 Mode Shapes[14,15]

$$\phi_1(x) = \cosh\epsilon_1(\tfrac{x}{\ell}) - \cos\epsilon_1(\tfrac{x}{\ell}) - \alpha_1[\sinh\epsilon_1(\tfrac{x}{\ell}) - \sin\epsilon_1(\tfrac{x}{\ell})]$$

(B-1)

where $\epsilon_1 = 1.8751$

$\alpha_1 = 0.7341$

$$\phi_2(x) = \cosh\epsilon_2(\tfrac{x}{\ell}) - \cos\epsilon_2(\tfrac{x}{\ell}) - \alpha_2[\sinh\epsilon_2(\tfrac{x}{\ell}) - \sin\epsilon_2(\tfrac{x}{\ell})]$$

(B-2)

where $\epsilon_2 = 4.6941$

$\alpha_2 = 1.0185$

$$\phi_\alpha(x) = \sin(\tfrac{\pi x}{2\ell})$$

(B-3)

$\phi_1(\ell) = 2.00$ $\qquad\qquad$ $\phi_1(0.75\ell) = 1.32$

$\phi_2(\ell) = -2.00$ $\qquad\qquad$ $\phi_2(0.75\ell) = 0.269$

$\phi_\alpha(\ell) = 1.00$ $\qquad\qquad$ $\phi_\alpha(0.75\ell) = 0.924$

The following integrals were evaluated numerically using ten point trapezoidal integration.

$$I_1 \equiv \frac{1}{\ell} \int_0^\ell \phi_1 dx = 0.783$$

$$I_2 \equiv \frac{1}{\ell} \int_0^\ell \phi_\alpha dx = 0.637$$

$$I_3 \equiv \frac{1}{\ell} \int_0^\ell \phi_1 \phi_\alpha \, dx = 0.678$$

$$I_4 \equiv \frac{1}{\ell} \int_0^\ell \phi_1^2 \, dx = 1.00$$

$$I_5 \equiv \frac{1}{\ell} \int_0^\ell \phi_\alpha^2 \, dx = 0.500$$

$$I_6 \equiv \ell^2 \int_0^\ell \phi_1'' \phi_\alpha' \, dx = 3.76$$

$$I_7 \equiv \ell^3 \int_0^\ell (\phi_1'')^2 \, dx = 12.4$$

$$I_8 \equiv \ell \int_0^\ell (\phi_\alpha')^2 \, dx = 1.23$$

$$I_9 \equiv \ell^2 \int_0^\ell \phi_2'' \phi_\alpha' \, dx = -6.43$$

$$I_{10} \equiv \ell^3 \int_0^\ell (\phi_2'')^2 \, dx = 485$$

$$I_{11} \equiv \ell^3 \int_0^\ell (\phi_\alpha'') \, dx = 3.04$$

$$I_{12} \equiv \frac{1}{\ell} \int_0^\ell \phi_2^2 \, dx = 1.00$$

B.2 U-g Diagrams
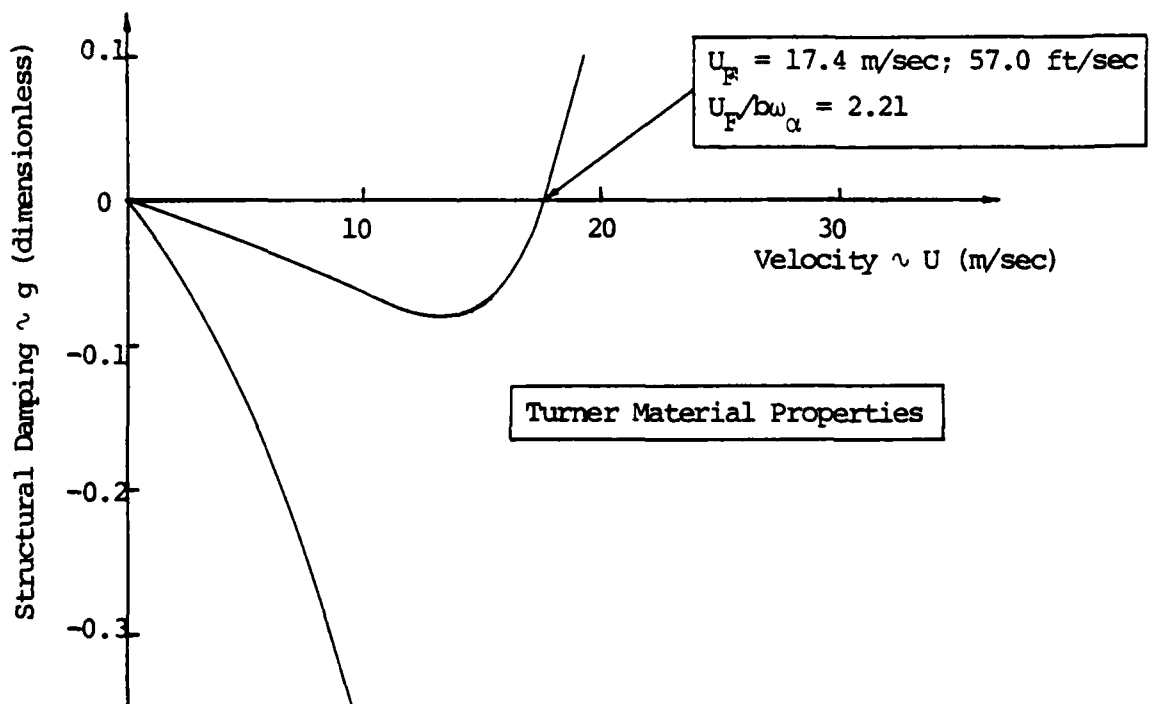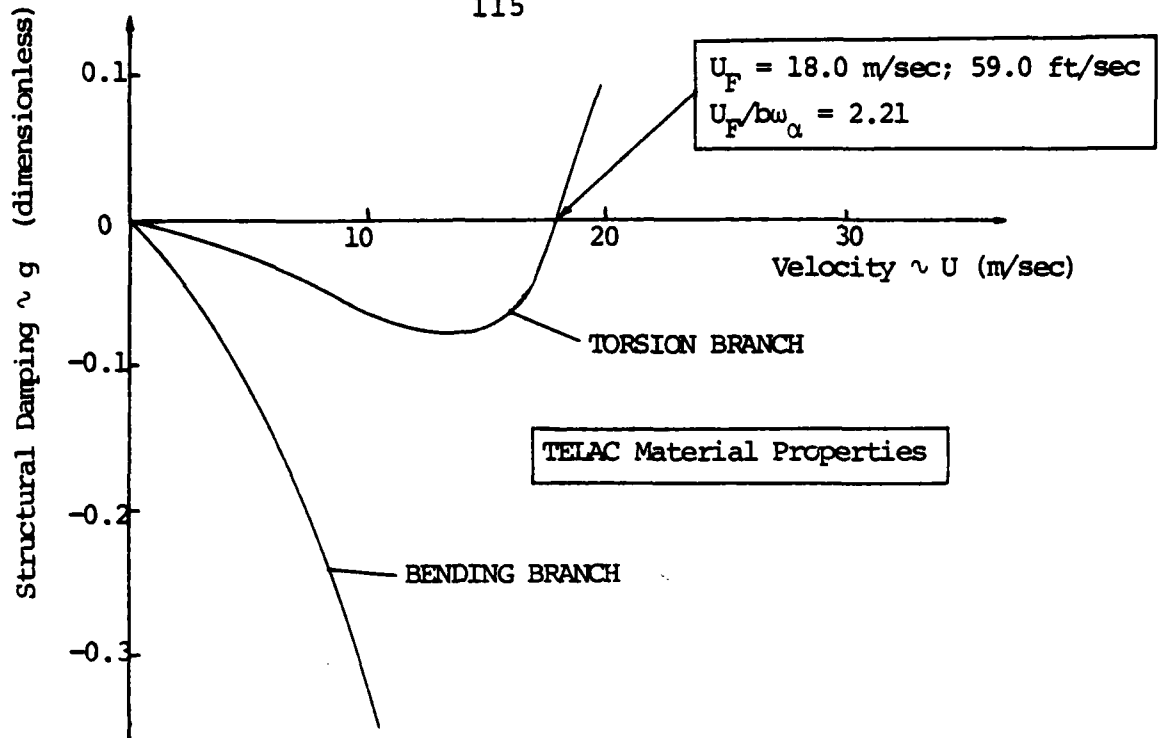
Figure B-1. U-g Diagram, $[0_2/90]_s$ Test Specimen
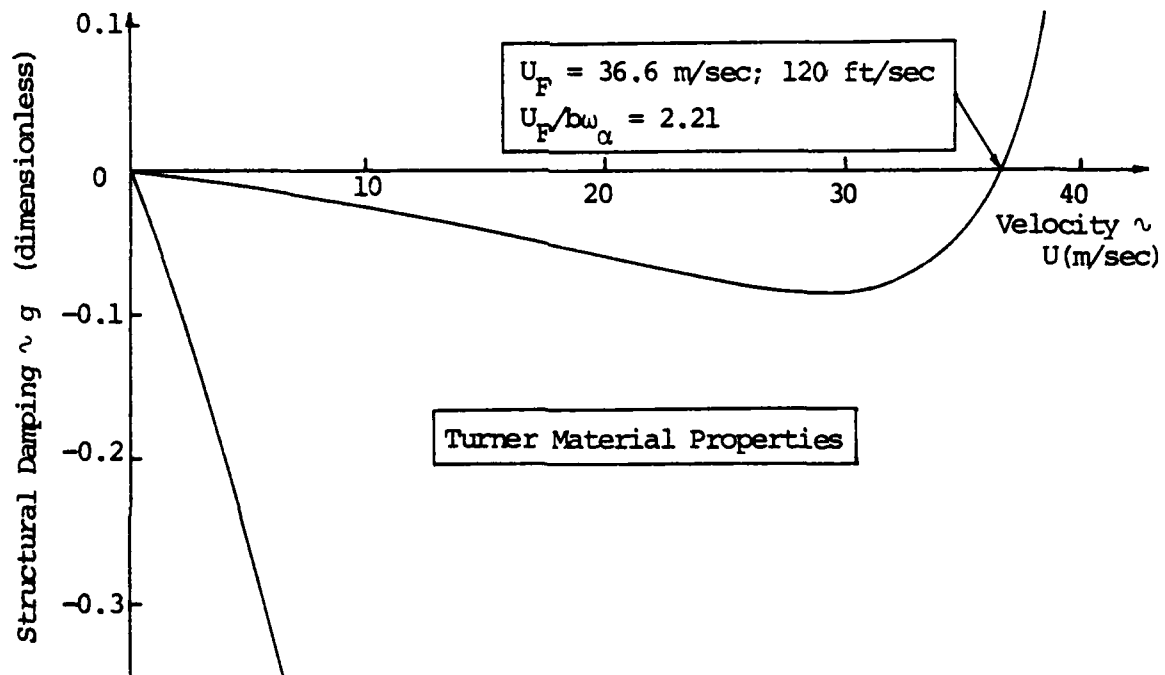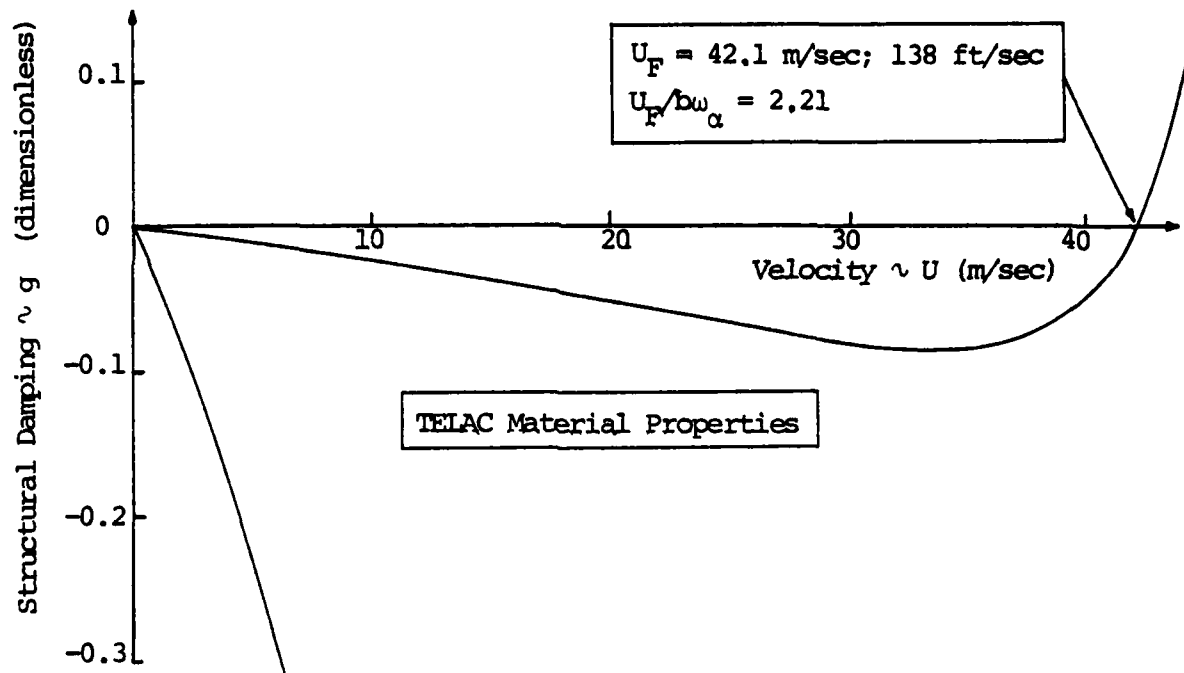
Figure B-2.   U-g Diagram, $[\pm45/0]_s$ Test Specimen
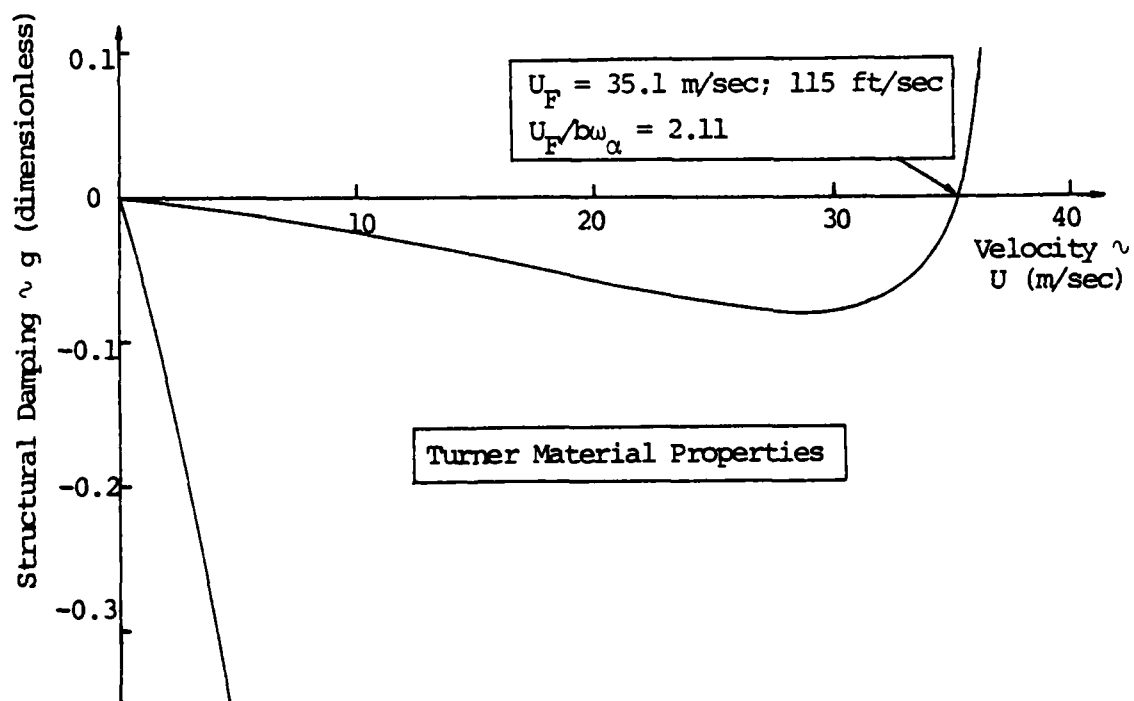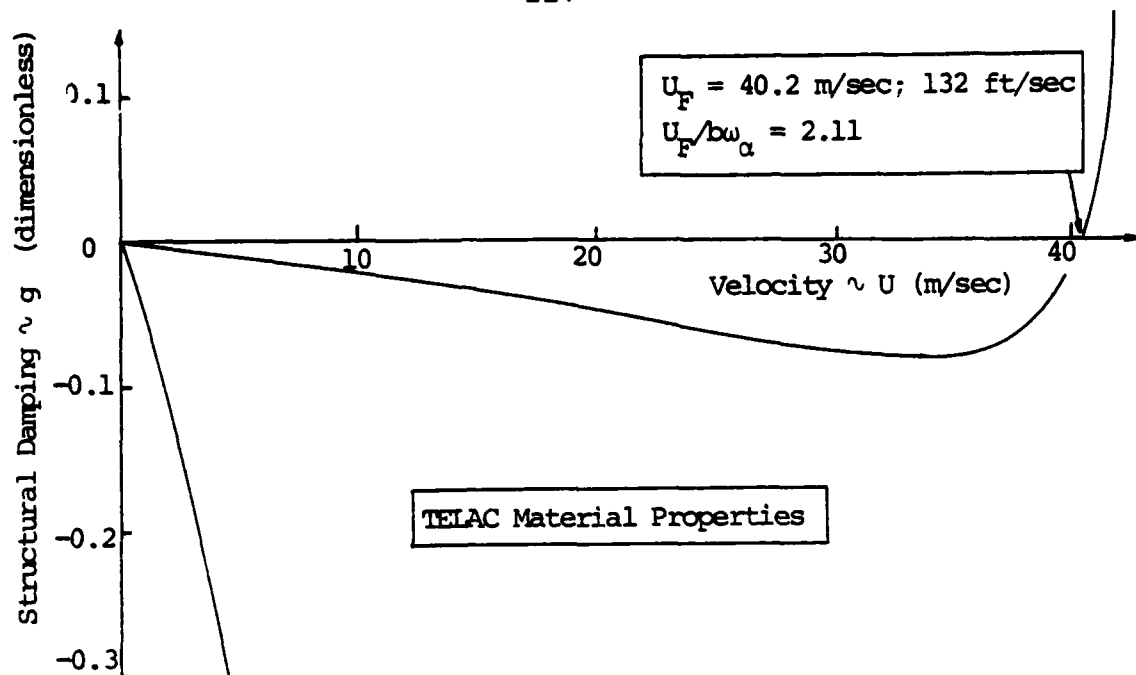
Figure B-3. U-g Diagram, $[+45_2/0]_s$ Test Specimen
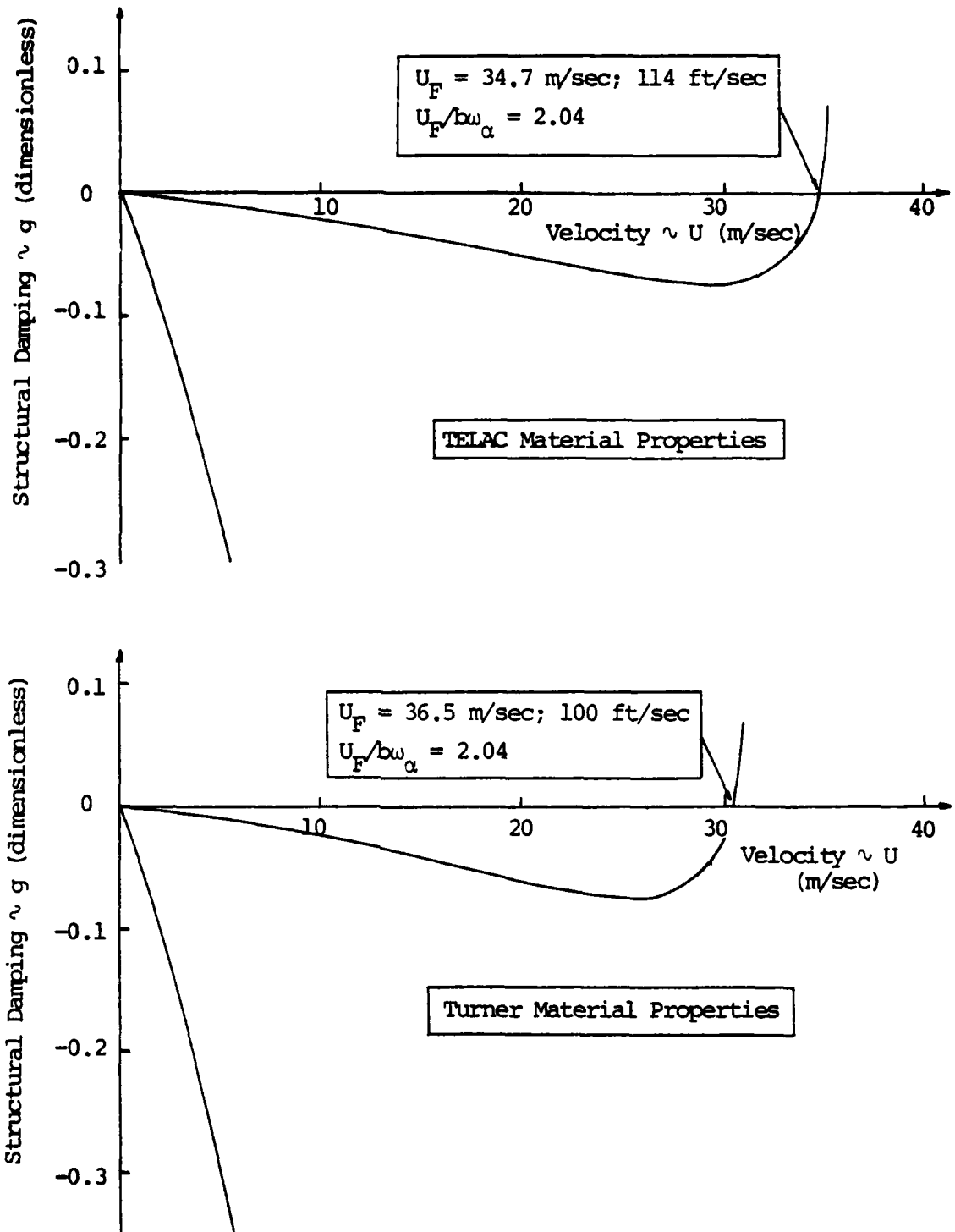
Figure B-4. U-g Diagram, $[+30_2/0]_s$ Test Specimen
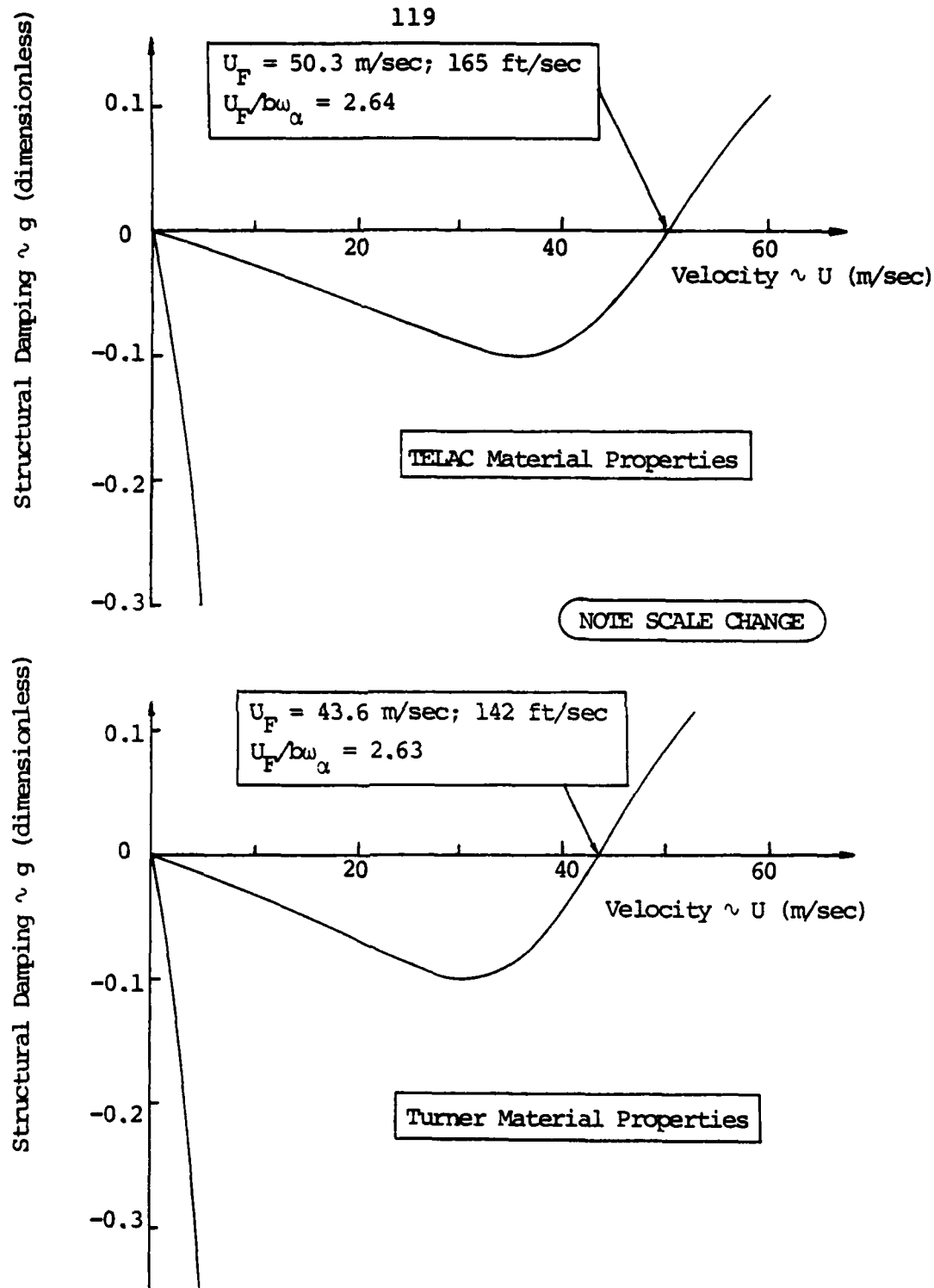
Figure B-5. U-g Diagram, $[-45_2/0]_s$ Test Specimen
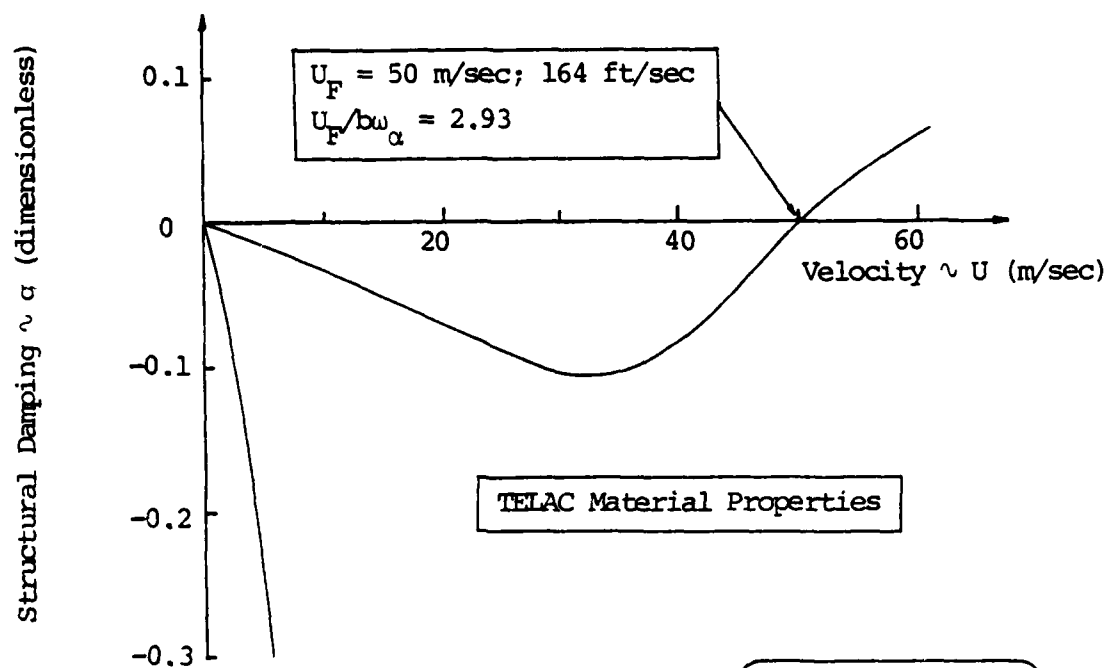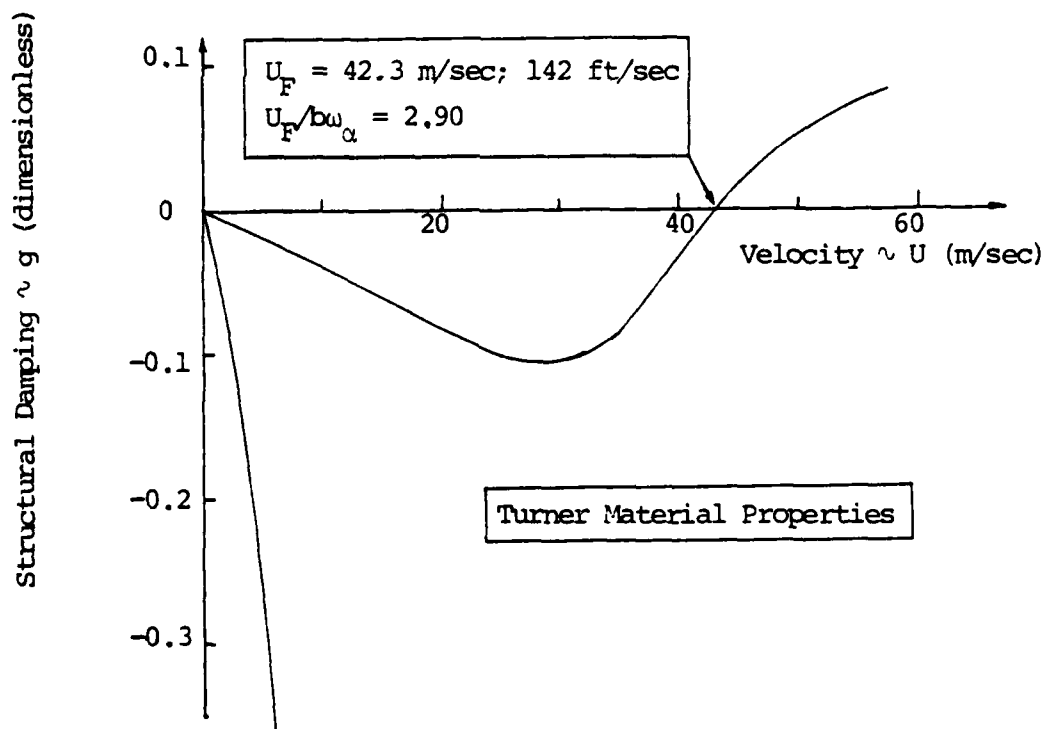
Figure B-6. U-g Diagram, $[-30_2/0]_s$ Test Specimen
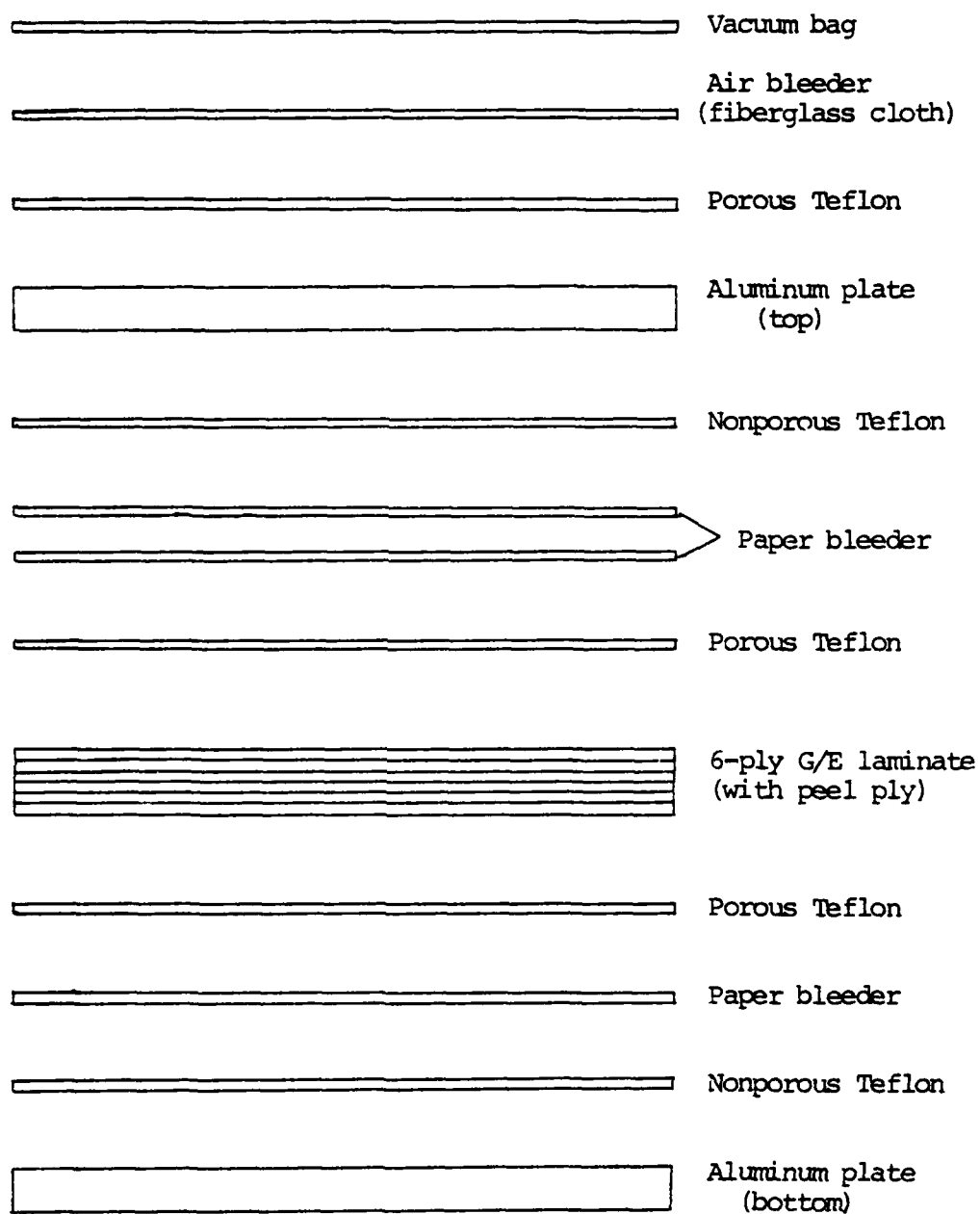
121

APPENDIX C

GRAPHITE/EPOXY CURING TECHNIQUES

▬▬▬▬▬▬▬▬▬▬▬▬	Vacuum bag
▬▬▬▬▬▬▬▬▬▬▬▬	Air bleeder (fiberglass cloth)
▬▬▬▬▬▬▬▬▬▬▬▬	Porous Teflon
▭▭▭▭▭▭▭▭▭▭▭▭	Aluminum plate (top)
▬▬▬▬▬▬▬▬▬▬▬▬	Nonporous Teflon
▬▬▬▬▬▬▬▬▬▬▬▬	Paper bleeder
▬▬▬▬▬▬▬▬▬▬▬▬	Porous Teflon
▬▬▬▬▬▬▬▬▬▬▬▬	6-ply G/E laminate (with peel ply)
▬▬▬▬▬▬▬▬▬▬▬▬	Porous Teflon
▬▬▬▬▬▬▬▬▬▬▬▬	Paper bleeder
▬▬▬▬▬▬▬▬▬▬▬▬	Nonporous Teflon
▭▭▭▭▭▭▭▭▭▭▭▭	Aluminum plate (bottom)

Figure C-1. Curing Materials

TABLE C-1

AUTOCLAVE CURE CYCLE

1. Place aluminum curing plate with curing materials (Fig. C-1) in autoclave and attach vacuum hose.

2. Perform vacuum test: Apply full vacuum (30 in) to curing plate, turn off vacuum pump, and watch bleed-down for five minutes.

3. Seal autoclave, apply full vacuum, and raise autoclave pressure to 85 psi.

4. Raise autoclave temperature to 240° F.

5. Maintain 85 psi and 240° F for one hour.

6. Raise pressure to 90 psi.

7. Raise temperature to 350° F.

8. Maintain 90 psi and 350° F for two hours.

9. Decrease temperature at a rate not exceeding 5° per minute until temperature reaches 130° F.

10. Release pressure and vacuum.

11. Open autoclave and remove curing plate.

APPENDIX D

TEST SPECIMEN DIMENSIONS

TABLE D-1

NOMINAL   TEST SPECIMEN DIMENSIONS

Parameter	Value	
Length	12.0 in	304.8 mm
Width	3.00	76.2
Ply thickness (nominal TELAC value)	0.00528	0.134
Total thickness (6 x ply thickness)	0.0317	0.804
Density (nominal TELAC value)	0.055 lb/in^3	1.52 x 10^3 kg/m^3

TABLE D-2

EXPERIMENTAL TEST SPECIMEN AVERAGE MEASUREMENTS

Test Specimen	Length		Width		Thickness		Density	
$[0_2/90]_s$	12.00 in	304.8 mm	3.004 in	76.27 mm	0.0313 in	0.795 mm	0.0556 lb/in.^{3}	1.54 x 10^3 kg/m^3
$[\pm 45/0]_s$	12.02	305.3	2.999	76.15	0.0326	0.828	0.0542	1.50 x 10^3
$[+45_2/0]_s$	11.98	304.3	3.003	76.25	0.0318	0.808	0.0553	1.53 x 10^3
$[+30_2/0]_s$	12.02	305.3	3.002	76.24	0.0314	0.798	0.0564	1.56 x 10^3

APPENDIX E

TEST DATA AND DATA REDUCTION METHODS

E.1 Flexibility Influence Coefficient Data Reduction

Test apparatus characteristics:

moment arm (1/2 couple) = 3.5 in

distance between front and rear rulers = 8.0 in

Test 1 raw data:

applied forces (F_T): ± 0.022 lb, ± 0.044, ± 0.066,

± 0.088

obtain front and rear deflections for each applied force

Test 2 raw data:

applied moments (M_T): ± 0.013 ft·lb, ± 0.026, ± 0.044,

± 0.056

obtain front and rear deflections for each applied moment

Data reduction for each test point:

lateral deflection (w_E) in units of feet = $[\dfrac{\text{front} + \text{rear}}{768}]$

angular deflection (α) in units of radians =

$$\tan^{-1}[\dfrac{\text{front} - \text{rear}}{256}]$$

$$c_{11} = \frac{W_E}{F_T} \ ; \quad c_{21} = \frac{\alpha}{F_T} \ ; \quad c_{12} = \frac{W_E}{M_T} \ ; \quad c_{22} = \frac{\alpha}{M_T}$$

Plots of all test points for each test specimen appear in Figs. E-1 to E-4.

E.2 Indicated and True Velocity Calculations

Raw data:

manometer reading (h_{alc}) in inches of alcohol

temperature (°F) at start and finish

barometric pressure (h_{Hg}) in inches of mercury

Indicated velocity calculation:

specific gravity (Sg) of alcohol = 0.805 at 80° F

specific weight (ω_{alc}) of alcohol = Sg(ω_{H_2O}) =

$$(0.805)(62.4 \ lb/ft^3) = 50.2 \ lb/ft^3$$

$$U_{indicated} = \frac{2\omega_{alc}h_{alc}}{\rho_{SL}} = 59.3 \sqrt{h_{alc}(inches)}$$

True velocity calculation:

$$U_{true} = U_{indicated}\left(\frac{1}{\sqrt{\sigma}}\right) \quad \text{where } \sigma = \rho/\rho_{SL} \text{ and}$$
$$\rho_{SL} = 0.002376 \ sl/ft^3$$

$$\rho = P_a(psf)/RT_a(°K)$$
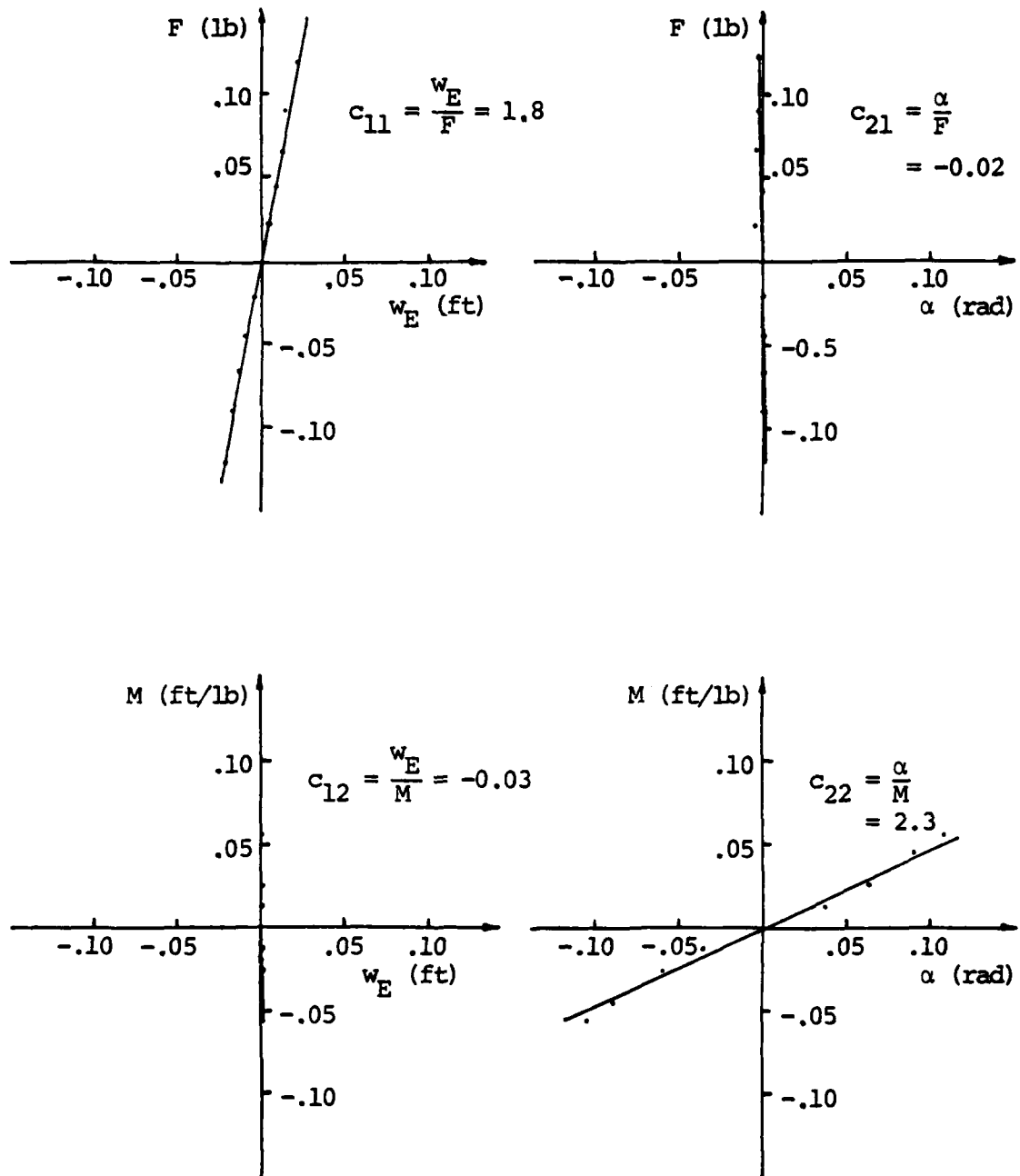
Figure E-1. Flexibility Influence Coefficients, $[0_2/90]_s$ Test Specimen
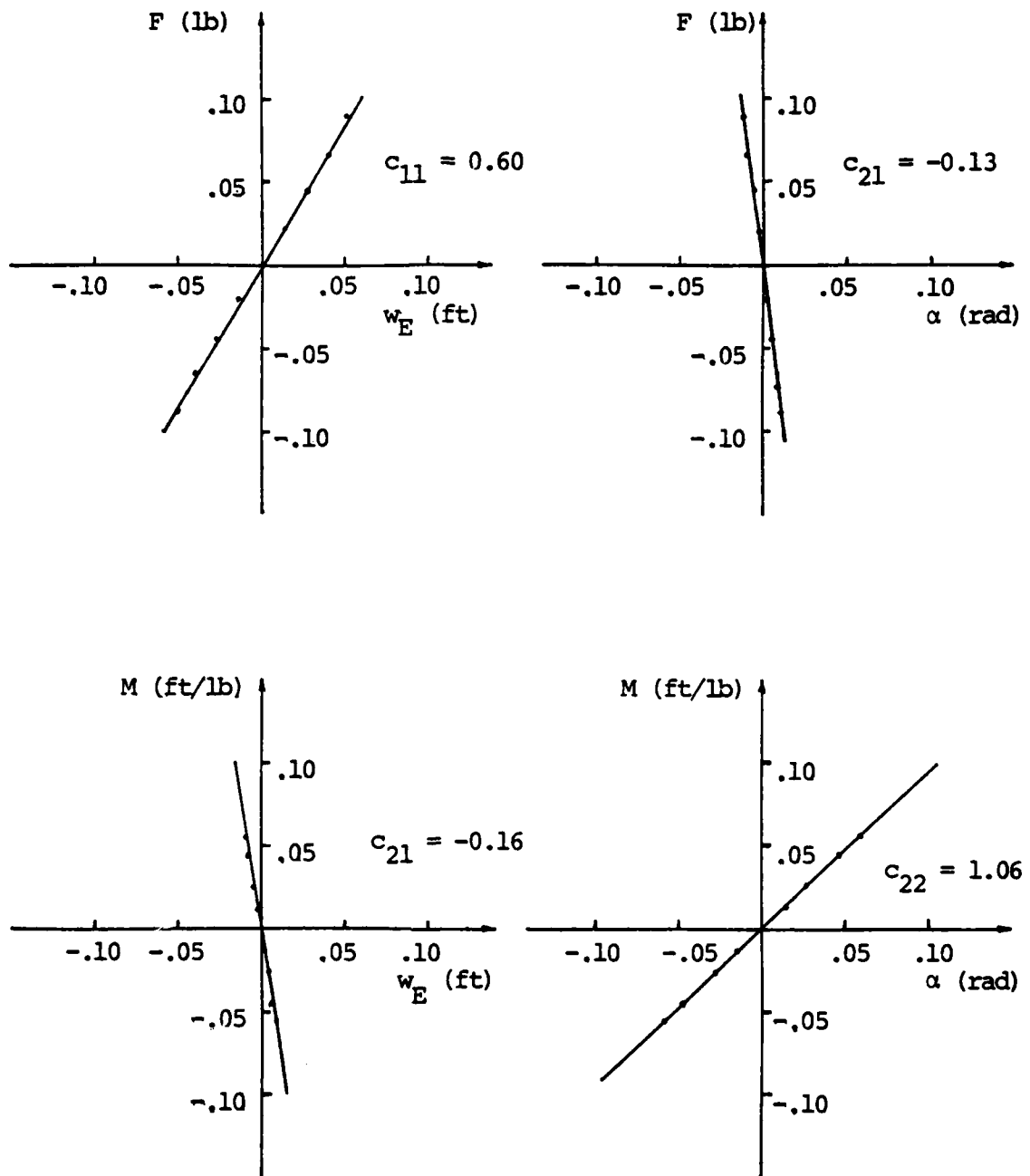
Figure E-2. Flexibility Influence Coefficients, [±45/0]$_s$ Test Specimen
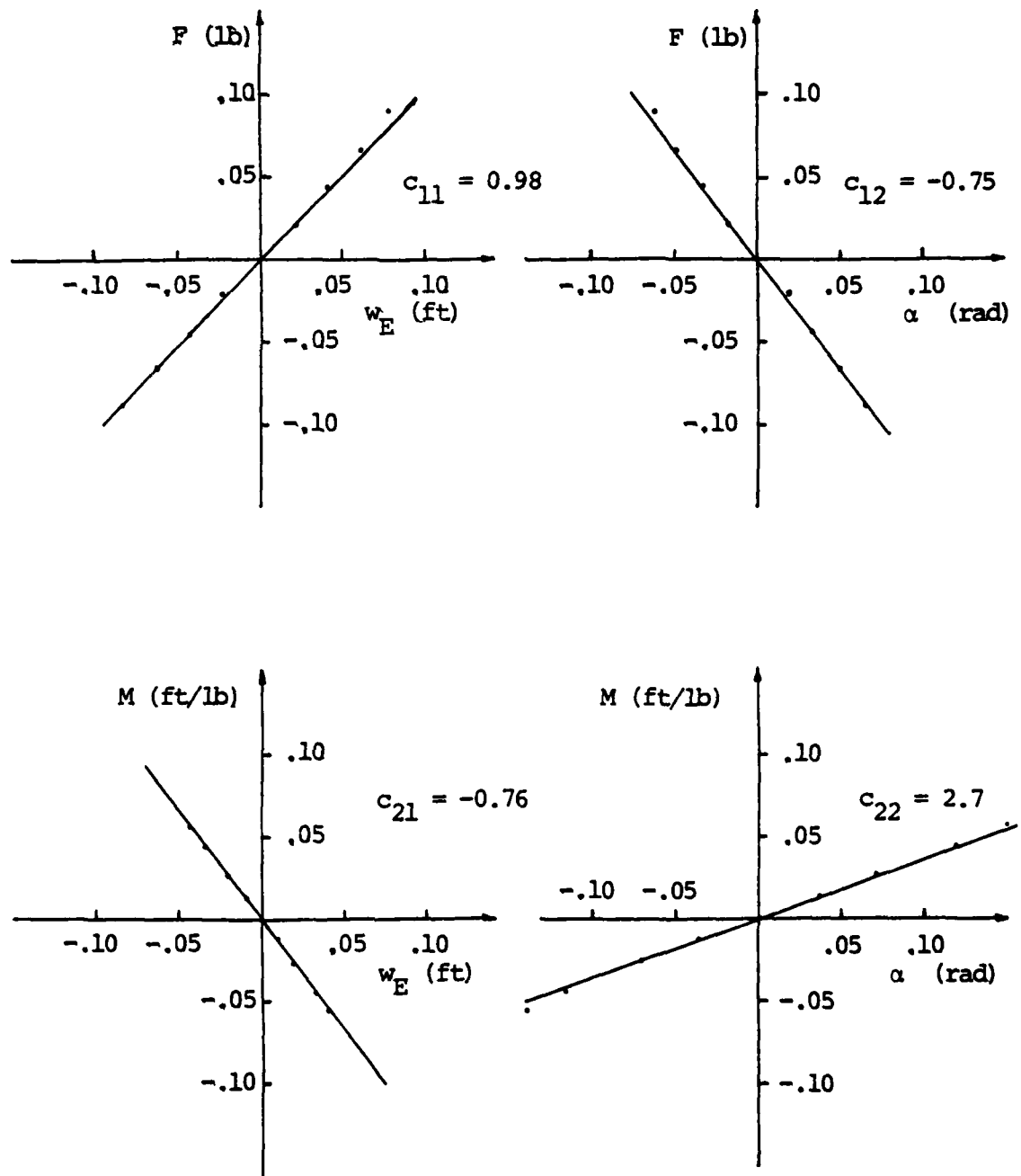
Figure E-3. Flexibility Influence Coefficients, $[+45_2/0]_s$ Test Specimen
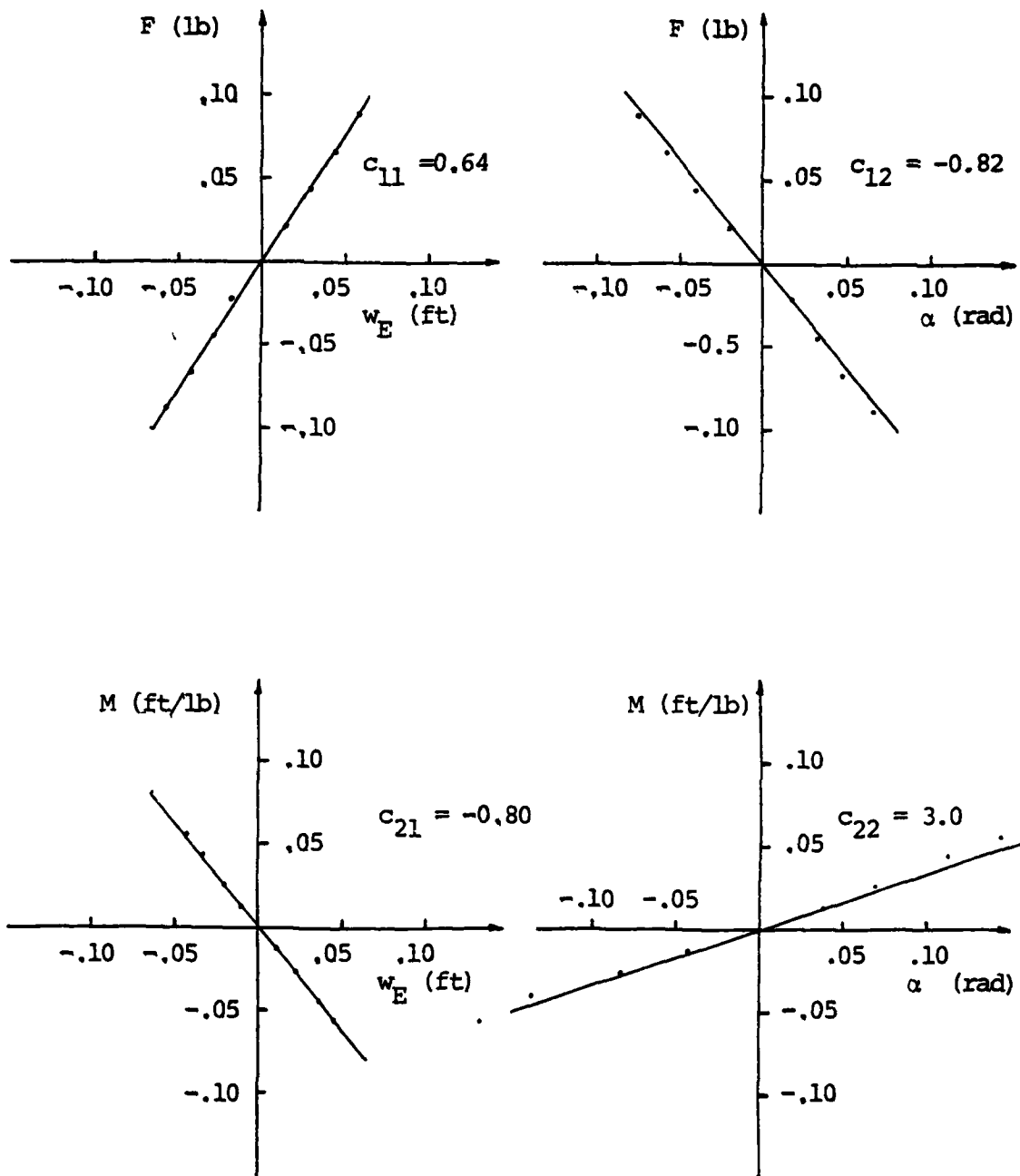
Figure E-4. Flexibility Influence Coefficients, $[+30_2/0]_s$ Test Specimen

$R = 3089.8 \text{ ft/sec}^2 \text{°K}$

$$T_a(\text{°K}) = 0.5556 \left[\left(\frac{T_{start} - T_{stop}}{2} \right) + 460 \right]$$

$$P_a(\text{psf}) = Sg_{Hg}\omega_{H_2O}h_{Hg}/12 = 70.72 \, h_{Hg} \text{ (inches)}$$

where $Sg_{Hg} = 13.6$

$$U_{true} = 59.3 \sqrt{h_{alc}(\text{inches})/\sigma}$$

E.3 Experimental Tip Deflection Calibrations

Calibration 1 raw data:

tip lateral deflections (δ_A): ± 0.25 in; ± 0.5; ± 0.75;

± 1.0

obtain strain gauge readings from strip chart in units

of mm

bending strain gauge (channel 2) (δ_C)

torsion strain gauge (channel 1) (θ_C)

Calibration 2 raw data:

tip angular deflections (θ_A): ± 4.78 deg; ± 9.55

obtain strain gauge readings from strip chart in units

of mm

By plotting each calibration point, obtain the following

slopes:

$$a_{11} = \frac{\delta_c(\text{cal 1})}{\delta_A(\text{cal 1})}$$

$$a_{21} = \frac{\theta_c(\text{cal 1})}{\delta_A(\text{cal 1})}$$

$$a_{12} = \frac{\delta_c(\text{cal 2})}{\theta_A(\text{cal 2})}$$

$$a_{22} = \frac{\theta_c(\text{cal 2})}{\theta_A(\text{cal 2})}$$

From these, we can obtain the following transformation equation:

$$\begin{Bmatrix} \delta_c(\text{mm}) \\ \theta_c(\text{mm}) \end{Bmatrix} = \begin{bmatrix} a_{11} & a_{12} \\ a_{21} & a_{22} \end{bmatrix} \begin{Bmatrix} \delta_A(\text{in}) \\ \theta_A(\text{deg}) \end{Bmatrix}$$

Since we want the inverse relationship, the A-matrix is inverted to obtain the final expression.

$$\begin{Bmatrix} \delta_A \\ \theta_A \end{Bmatrix} = [A]^{-1} \begin{Bmatrix} \delta_c \\ \theta_c \end{Bmatrix}$$

From this expression, we can get approximate values for the test specimen tip deflections knowing the strip chart strain gauge readings.

TABLE E-1

EXPERIMENTAL NATURAL FREQUENCIES

Test Specimen	Vibration Mode	Shaker (visual) 30 Sep 80	Shaker (visual) 30 Oct 80	Shaker (Oscilloscope)	Wind Tunnel (U = 0) 6 Oct 80	Wind Tunnel (U = 0) 23 Oct 80	Average
$[O_2/90]_s$	1B	11.0 Hz	11.1 Hz	11.1 Hz	11.1 Hz	not tested	11.1 Hz
	2B	68.5	69.6	69.5	68.3		69.0
	1T	42.7	43.1	42.1	40.8		42.2
$[\mp45/0]_s$	1B	5.9	6.1	6.2	6.0	6.15	6.1
	2B	38.0	38.8	38.8	38.0	38.8	38.5
	1T	78.0	79.1	78.2	75.5	76.3	77.4
$[+45_2/0]_s$	1B	4.8	4.8	4.9	4.8	4.85	4.8
	2B	29.6	30.3	30.4	30.0	30.4	30.1
	1T	50.9	51.4	51.1	49.5	52.4	51.1
$[+30_2/0]_s$	1B	5.9	6.1	6.0	5.9	5.95	6.0
	2B	35.9	36.5	36.7	~35	36.3	36.1
	1T	57.3	59.1	59.1	~60	58.1	58.4

133

134

REFERENCES

1. Krone, N.J., Jr., "Divergence Elimination with Advanced Composites", AIAA Paper No. 75-1009, 1975.

2. Weisshaar, T.A., "Aeroelastic Stability and Performance Characteristics of Aircraft with Advanced Composite Swept-forward Wing Structures", Air Force Flight Dynamic Laboratory Technical Report, AFFDL-TR-78-116, September, 1978.

3. Weisshaar, T.A., "Forward Swept Wing Static Aeroelasticity", Air Force Flight Dynamics Laboratory Technical Report, AFFDL-TR-79-3087, June, 1979.

4. Sherrer, V.C., Hertz, T.J., and Shirk, M.H., "A Wind Tunnel Demonstration of the Principle of Aeroelastic-Tailoring Applied to Forward Swept Wings", included in the proceedings, "AIAA/ASME/ASCE/AHS 21st Structures, Structural Dynamics, and Materials Conference", Seattle, Wash., May, 1980.

5. Naberhaus, J.D., and Waddoups, M.E., "Dynamic Characteristics of Advanced Filamentary Composite Structures", 3 volumes, Air Force Flight Dynamics Laboratory Technical Report AFFDL-TR-73-111, September, 1974.

6. Griffin, K.E., "An Aeroelastic Tailoring Study of a High Aspect Ratio Wing", included in the proceedings, "Third Conference on Fibrous Composites in Flight Vehicle Design", NASA TM X-3377, 1976.

7. Lynch, R.W., Rogers, W.A., and Braymen, W.W., "Aeroelastic Tailoring of Advanced Composite Structures for Military Aircraft", 3 volumes, Air Force Flight Dynamics Laboratory Technical Report AFFDL-TR-76-100, April, 1977.

8. Rainey, G.A., "Preliminary Study of Some Factors which Affect the Stall-Flutter Characteristics of Thin Wings", NACA TN-3622, March, 1956.

9. Dugundji, J., and Aravamundan, K., "Stall Flutter and Nonlinear Divergence of a Two-Dimensional Flat Plate Wing", Aeroelastic and Structures Research Laboratory Technical Report ASRL-TR-159-6, Department of Aeronautics and Astronautics, M.I.T., July, 1974.

10. Turner, M.D., "Comparison of Static and Dynamic Test Methods for Determining the Stiffness Properties of Graphite/Epoxy Laminates", M.S. Thesis, Department of Aeronautics and Astronautics, M.I.T., June, 1979.

11. Tsai, S.W., and Hahn, H.T., "Introduction to Composite Materials, Vol. I: Deformation of Unidirectional and Laminated Composites", Air Force Materials Laboratory Technical Report TR-78-201, January, 1979.

12. Ashton, J.E., and Waddoups, M.E., "Analysis of Anisotropic Plates", Journal of Composite Materials, Vol. 3, pp. 148 - 165, January, 1969.

13. Bisplinghoff, R.L., Ashley, H., and Halfman, R.L., Aeroelasticity, Addison-Wesley Publishing Co., Reading, Mass., 1955.

14. Bisplinghoff, R.L. and Ashley, H., Principles of Aero-elasticity, Dover Publications, Inc., New York, 1962.

15. Young, D., "Vibration of Rectangular Plates by the Ritz Method", ASME Paper No. 50-APM-18, 1950.

16. Edwards, J.W., Ashley, H., and Breakwell, J.V., "Unsteady Aerodynamic Modeling for Arbitrary Motions", included in the proceedings, "AIAA/ASME 18th Structures, Structural Dynamics and Materials Conference", San Diego, Calif., 1977.

17. Crawley, E.F., "The Natural Mode Shapes and Frequencies of Graphite/Epoxy Cantilevered Plates and Shells", M.S. Thesis, Department of Aeronautics and Astronautics, M.I.T., June, 1978.

18. Boyce, D.A., "Material Damping of Graphite/Epoxy Double Cantilever Beams", M.S. Thesis, Department of Aeronautics and Astronautics, M.I.T., September, 1979.

19. Crawley, E.F., and Dugundji, J., "Frequency Determination and Non-Dimensionalization for Composite Cantilever Plates", Journal of Sound and Vibration, Vol. 72, No. 1, pp. 1-10, 8 September, 1980.

LIST OF SYMBOLS

A   Amplitude of oscillation

a_0 Two dimensional lift curve slope = 2π

b   Semichord = c/2

C(k)   Theodorsen function

C_ℓ Lift coefficient

c   Chord

c_{ij} Flexibility influence coefficients

D_{ij} Flexural modulus for an anisotropic plate

E_L Longitudinal modulus

E_T Transverse modulus

e   Distance between elastic axis and aerodynamic center

F_t Concentrated test load

G_{LT} Shear modulus

g   Structural damping coefficient

i $\sqrt{-1}$

k   Reduced frequency = $\omega b/U$

k_{ij} Stiffness influence coefficient

L_E Lift force at elastic axis

ℓ Length of plate

M_E Aerodynamic Moment

M_t Concentrated test moment

m   Mass per area

p_z Distributed lateral load

Q_i Generalized force

Q_{ij} In-plane, on-axis lamina modulus

q Dynamic pressure

q_i Generalized displacement

T Kinetic energy

t Time

t_p Plate thickness

U Velocity

U_D Divergence velocity

U_F Flutter velocity

V Strain energy

W_e External work

w Lateral deflection

w_E Lateral deflection of elastic axis

$w_{E_{TIP}}$ Tip lateral deflection

Z Complex eigenvalue = $(1 + ig)/\omega^2$

α Angle of attack

α_0 Initial angle of attack

$\alpha_{\bar{e}}$ Elastic twist

α_{TIP} Tip angle of attack

γ_i Mode shape (two dimensional)

θ Ply angle

κ Coupling factor

ν_{LT} Major Poisson's ratio

ν_{TL} Minor Poisson's ratio

ρ, ρ_{∞} Air density

ϕ_i Mode shape (one dimensional)

ω Frequency of oscillation

ω_{α} Torsional natural frequency

DAT
ILM